

Copyright
by
Chandriker Kavir Dass
2015

The Dissertation Committee for Chandriker Kavir Dass Certifies that this is the approved version of the following dissertation:

**Two-Dimensional Coherent Spectroscopy of Monolayer Transition
Metal Dichalcogenides**

Committee:

Xiaoqin Li, Supervisor

Michael Downer

Keji Lai

Chih-Kang Shih

Emanuel Tutuc

**Two-Dimensional Coherent Spectroscopy of Monolayer Transition
Metal Dichalcogenides**

by

Chandriker Kavir Dass, B.S.

Dissertation

Presented to the Faculty of the Graduate School of

The University of Texas at Austin

in Partial Fulfillment

of the Requirements

for the Degree of

Doctor of Philosophy

The University of Texas at Austin

August 2015

Acknowledgements

I'm immensely grateful for having had the opportunity of studying at The University of Texas Austin and for the people I've met in my five and half years here. My time here in Austin has been a significant period of growth for me, both personally and academically, as well as an integral experience to shape my future path in life.

I'd like to thank, first and foremost, my adviser, Elaine Li, who showed patience and understanding despite the many obstacles thrown our way. You've taught me the meaning of duty, dedication, and hard work and without your tenacious drive, I would not be writing this today.

I'd also like to thank my lab mates for their humor and help. It made all those hours aligning optics feel a lot less tedious and a lot more productive. A special mention must be made for Galan Moody and Kai Hao who were indispensable to the success of this project. My thanks go to you two most of all.

Lastly, I'd like to thank my family, friends and loved ones who have helped me along the way. You've supported me in ways that can't be measured in words and for that I am immeasurably grateful.

Two-Dimensional Coherent Spectroscopy of Monolayer Transition Metal Dichalcogenides

Chandriker Kavir Dass, Ph.D

The University of Texas at Austin, 2015

Supervisor: Xiaoqin Li

Two-dimensional semiconductors have long been studied for their unique optical and electronic properties, but with the work of Novoselov and Geim on van der Waals materials, two-dimensional semiconductors have seen a surge of renewed interest. This dissertation focuses on monolayer transition metal dichalcogenides (TMDCs), a class of two-dimensional materials that can easily be fabricated by mechanical exfoliation, much like graphene. In their bulk form, these materials have indirect band gaps, but transition to direct gap semiconductors in the monolayer limit. The band-edge optical response of TMDCs, like WSe₂ and MoS₂, is dominated by exciton absorption occurring at the $\pm K$ -points of the Brillouin zone. Because of the unique electronic structure of these materials, these two points form distinct valleys in the band structure which can be exploited to produce valley polarization.

Exciton quantum dynamics are characterized by two fundamental parameters, one of which is the dephasing rate, γ , which describes quantum dissipation arising from the interaction of the excitons with their environment (*i.e.* other excitons, impurities, etc...). This dissertation focuses on measuring the fundamental property of dephasing time (which is inversely proportional to the dephasing rate and homogeneous linewidth) in monolayer WSe₂ through the use of two-dimensional coherent spectroscopy. Our

measurements have revealed a homogeneous linewidth consistent with dephasing times in the sub-picosecond regime. We also characterize the role of exciton-exciton and exciton-phonon interactions, on the homogeneous linewidth, through excitation density and temperature dependent studies. These studies have revealed strong many-body effects and nonradiative population relaxation as the primary dephasing mechanisms. Microscopic calculations show that in perfect crystalline samples of monolayer TMDCs, the radiative lifetimes are also in the sub-picosecond regime due to the large oscillator strengths inherent in these materials. This result is consistent with the short dephasing times found experimentally.

Table of Contents

Chapter 1 Introduction	1
1.1 Fabrication	3
1.2 Electronic and Optical Properties	4
1.3 Spin Orbit and Valley Interactions	6
1.4 Linear and Nonlinear Studies.....	8
1.5 2DCS On TMDCs.....	9
1.6 Dissertation Outline	13
Chapter 2 Semiconductor Theory of 2D Confined Systems.....	15
2.1 Bloch's Theorem	16
2.2 Excitons in Bulk.....	18
2.3 Infinite and Finite Wells	23
2.4 Excitons in Two Dimensions	30
2.5 Optically Created Excitons	32
2.6 Non-Ideal Behavior In 2D Materials	37
Chapter 3 Two-Dimensional Coherent Spectroscopy.....	39
3.1 Historical Overview of 2DCS.....	40
3.2 Four-wave Mixing	41
3.3 Types of FWM Experiments.....	45
3.4 The Nonlinear Response Function.....	46
3.5 The Optical Bloch Equations.....	49
3.6 Feynman Diagrams	54
3.7 2D Spectroscopy	59
3.8 Types of 2D Spectra.....	62
3.9 Interpreting 2D Spectra.....	66
3.10 Lineshape Analysis	67
Chapter 4 Experimental Apparatus	70
4.1 The JILA-MONSTR	70

4.2 Sample Preparation, Photoluminescence and Sample Imaging	77
4.3 Fourier Transform Spectral Interferometry	80
4.4 Phase Cycling.....	82
4.5 Acquiring 2D Data.....	85
Chapter 5 2DCS on Monolayer TMDCs	88
5.1 Motivations	89
5.2 Photoluminescence Studies.....	92
5.3 2DCS Studies of EID.....	96
5.4 2DCS Studies of Phonon Interaction	101
5.5 Calculating Homogeneous Linewidth.....	102
Chapter 6 Conclusion and Outlook.....	105
6.1 Conclusion	105
6.2 Outlook	106
Appendix Pump Probe on Hybrid Structures.....	108
A.1 Applications and Motivations	108
A.2 Sample Design	110
A.3 Experimental Apparatus.....	112
A.4 Results.....	114
Citations	121

Chapter 1: Introduction

Since the seminal work of Novoselov and Geim in 2005 [1, 2], graphene has ushered in a robust and fascinating field of research into atomically thin materials with unique electrical and optical properties. Transition metal dichalcogenides (TMDCs) are layered materials with strong in-plane bonding and weak out-of-plane interactions allowing for the exfoliation of the material into two-dimensional layers of unit cell thickness. Although these materials have been studied for decades, recent advances in nanoscale materials characterization and device fabrication--largely spurred on by graphene research--have opened up avenues of exploration for two-dimensional layers of ultra-thin TMDCs in nanoelectronics and optoelectronics. TMDCs such as WSe₂, MoS₂, MoSe₂, and WS₂ have sizable bandgaps that change from indirect to direct when exfoliated from their bulk to monolayer forms, allowing for applications in transistors, photodetectors, and electroluminescent devices. TMDCs have also emerged as excellent candidates in exploring control of valley dependent degrees of freedom with potential applications in valleytronics. Two-dimensional group-VI dichalcogenides MX₂ (M=Mo or W; X=S or Se) provide an ideal platform for exploring valley pseudospin degrees of freedom. In monolayers, the M and X atoms form a 2D hexagonal lattice that lacks spatial inversion symmetry. The breaking of inversion symmetry produces valley contrast in the orbital magnetic moment (\mathbf{m}) at the conduction and valence band edges located at $\pm K$ points in momentum space. This valley contrast can be exploited to produce a valley Hall effect as well as allowing for the optical preparation, control, and detection of valley pseudospin polarization. TMDCs also have very large excitonic effects with exciton binding energies in the range of a few hundred meV [3-7]. Such strong Coulomb interactions are inherent to systems of reduced dimensionality, but are also the result of

reduced dielectric screening of atomically thin materials and the relatively large electron and hole effective masses. These robust excitons, in conjunction with valley selectivity, offer the opportunity to demonstrate the optical manipulation of valley pseudospin. The important role of many-body effects have also been well-documented in recent ultrafast studies of TMDC materials and show the promise of an ideal platform in which to study many-body interactions [8-13].

In this chapter we will review the synthesis as well as the linear and nonlinear optical studies performed on monolayer TMDCs in the last few years and the insights into the excitonic properties that have been gained. The studies of the last few years have also opened up avenues of device applications in transistors, photodetectors and many more electronic and optoelectronic applications which will also be discussed. Because of the recent emergence of this field, many questions regarding the exciton dynamics in monolayer TMDCs remain unanswered. The chapter will continue with a discussion that will briefly explain our efforts, using two-dimensional coherent spectroscopy (2DCS), to answer some of the basic questions of intrinsic homogeneous linewidth, exciton-exciton interaction and exciton-phonon interaction. 2DCS offers a unique and powerful advantage in probing the exciton dynamics in these ultra-thin materials. As it is a very advanced version of four-wave mixing spectroscopy, we will discuss and compare it to some more simple spectroscopic techniques in order to develop some understanding of the advantages of 2DCS. The introduction chapter will then conclude with an overview of our main results followed by an outline of this dissertation.

1.1 FABRICATION

Reliable and scalable synthesis of 2D TMDCs is essential for translating their unique optical and electronic properties into applications. Fabrication techniques for 2D TMDCs can be broadly divided into one of two categories, top-down exfoliation or bottom-up synthesis.

By and far, the most common techniques are those that utilize top-down exfoliation, the simplest of these being the “scotch tape” method [2, 14-19]. Because TMDCs are layered materials bound together by weak van der Waal’s forces between layers, atomically thin flakes can be peeled from their parent bulk crystals much like was done in the early days of graphene. This method can produce single-crystal flakes of very high purity suitable for fundamental characterization [15-17, 20] and fabrication of single devices [16, 18-24]. The drawback of this method is that it is not scalable and is not repeatable. Recent work has successfully used a focused laser to exfoliate MoS₂ down to monolayer thickness through laser ablation. This method, although much more repeatable, would be difficult to scale up because of the laser raster scanning rates needed.

Less common methods of top-down exfoliation, but with the potential for more scalability, are ultrasonic exfoliation in liquid media [25-28] or ion-based liquid exfoliation [29-34]. In ion-based liquid exfoliation, lithium-based ionic compounds are mixed with TMDC powder and allowed to sit for a period of time. The lithium ions intercalate between the layers and then water is introduced forcing a reaction between the lithium and water to produce H₂ gas. The production of H₂ forces the separation of the layers resulting in gram quantities of submicron-sized monolayers. Ultrasonic exfoliation works by using organic solvents, aqueous surfactant solutions, or solutions of polymers in solvents which work to mechanically layered crystals yielding monolayer flakes a few

hundred nanometers in size. Both methods give a high yield of monolayer flakes compared to the “scotch tape” method, but with notable disadvantages. Ion-based liquid exfoliation is particularly notorious for changing the electronic and optical properties of some TMDCs, while ultrasonic exfoliation methods are susceptible to adsorb onto the surface of the monolayers.

In addition to the top-down methods already described, some growers of monolayer TMDCs employ bottom-up techniques such as chemical vapor deposition (CVD) [35-39], PVD [40] and epitaxial growth [41, 42]. Bottom up methods have shown the most promise in synthesizing large-area and uniform layers for such applications as wafer-scale fabrication of electronic devices and flexible, transparent optoelectronics. Of the bottom-up methods, CVD synthesis has proven to be particularly successful in creating large-area, high quality monolayer TMDCs on sapphire. CVD synthesis often involves heating of powder precursors--such as WO_3 powder and Se powder for the case of WSe_2 --in a furnace. This heated precursor is then transported via flowing Ar/ H_2 gas to a sapphire substrate where it is deposited and forms as WSe_2 . Precise control over the thickness can be achieved by monitoring the temperature of the precursors as well as the ratio of both precursors.

1.2 ELECTRONIC AND OPTICAL PROPERTIES

The band structures of many TMDCs are very similar in their general features, as verified by first principles and tight-binding calculations [43-49] as well as spectroscopic measurements [16, 20, 50-53]. In general, MoX_2 and WX_2 compounds are semiconducting, whereas most other TMDCs are metallic [43-48]. For TMDCs like MoS_2 and WSe_2 , the transition at the Γ -point is indirect in the bulk form of these materials, but shift to a direct-gap transition at the K -point at the monolayer limit [54-59].

The direct-gap transition at the K -point remains unchanged as a function of layer number, while the indirect transition at the Γ -point shifts from a small, indirect transition to a larger, one as the layer number is reduced. In MoS_2 and WSe_2 , this change can be attributed to hybridization between metal d and chalcogen p states below the Fermi energy [16, 20, 45, 60]. Density-functional theory calculations show that the conduction band states at the K -point are mainly due to localized d orbitals and are relatively unaffected by interlayer coupling as they are located in between the individual metal-chalcogen layers. For the Γ -point, the situation is quite different and the states in this region are the result of p_z -orbitals on the chalcogen and d -orbitals on the metal and have strong interlayer coupling [20]. All MX_2 and WSe_2 compounds are expected to be very similar in the nature of their indirect to direct-gap transitions as a function of decreasing layer number, with the direct-gaps of these materials ranging from 1.1-1.9 eV [43, 45-48, 61].

Because semiconducting TMDCs have direct semiconducting bandgaps in the visible portion of light, they are of great interest for applications in optoelectronics and because they can be made into a monolayer thick form, they have the potential to be used in flexible and transparent optoelectronics. The changes in the electronic bandstructure, as a result of changes in layer number, also directly influence the photoconductivity, absorption spectra and photoluminescence (PL) [16, 20, 43]. The most dramatic change can be seen in the PL where the shift from an indirect gap to direct gap semiconductor can increase the quantum yield by a factor of 10^4 [16]. Despite this large enhancement from bulk to monolayer, the overall quantum yield of semiconducting TMDCs is dismally low compared to conventional semiconductors. Compared to the near-unity values one would expect for a direct gap semiconductor, TMDCs have only been shown

to achieve values on the order of 10^{-3} [16] and much improvement must be made in order for these materials to compete with commercially used semiconductor materials.

The room temperature photoluminescence for WSe₂ shows two main resonances, the *A* and *B* excitons at around 750 nm and 600 nm, respectively [62, 63], but these values can vary slightly for samples produced via CVD or mechanical exfoliation. Mechanical exfoliation of WSe₂ usually yields samples with *A* exciton PL showing up at wavelengths slightly smaller than 750 nm. WSe₂ also has additional peaks at wavelengths below 600 nm corresponding to the indirect-gap luminescence and direct-gap hot luminescence [16]. The photoconductivity of TMDCs also reflects these band-structure features, with the photocurrent increasing in steps with respect to the photon energy corresponding to the direct and indirect gap energies [16]. The optical absorption spectrum for some semiconductor TMDCs shows two main peaks corresponding to the *A* and *B* excitons [16, 20, 64]. Calculations have confirmed that the *A* and *B* excitons correspond to the expected gap energies at the *K*-point of the Brillouin zone, confirming that these excitons are indeed due to the direct-gap transitions at the Brillouin zone edge [7]. The calculations also show that the exciton binding energies are quite high due to the reduced dielectric constants compared with bulk, as well as the 2D confinement. Exciton binding energies for WSe₂ and MoS₂ are predicted to be in the range of 0.5 eV to 1 eV [65] with recent experimental work showing the binding energies in the range of 0.3-0.5 eV [63, 66].

1.3 SPIN, ORBIT AND VALLEY INTERACTIONS

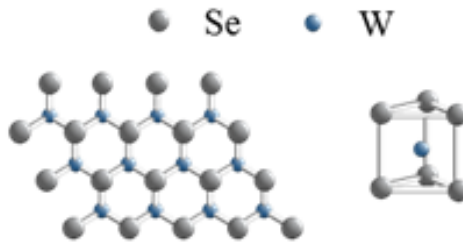


Figure 1: 2D hexagonal crystal lattice of monolayer WSe_2 consisting of two planes of Se atoms separated by a single plane of W atoms.

For group-IV semiconducting dichalcogenides, including MoS_2 and WSe_2 , strong spin-orbit coupling at the K -point in the Brillouin zone leads to splitting of the electronic bands [67]. Unlike bilayer TMDCs and graphene, both being centrosymmetric, monolayer TMDCs lack inversion symmetry (see Figure 1). The lack of inversion symmetry, high degree of electron confinement, and the high mass of the elements that make up the MX_2 materials leads to strong spin-orbit coupling the signature of which have been observed in optical absorption spectra, where the two main excitonic features—the A and the B excitons that come from the two spin-split valence bands in the $\pm K$ valley [64]—have an energy splitting of 150 meV to 400 meV in molybdenum [16, 66] and tungsten dichalcogenides [62, 68], respectively. This splitting agrees with first-principles calculations and ARPES measurements of SOC-induced splitting in the valence bands [69, 70]. For the conduction band, first-principles calculations show a small but finite spin-valley with a magnitude of several to tens of meV for different monolayers TMDCs [6, 68, 71-74]. An important consequence of this spin-valley coupling is that the spin-index becomes locked to the valley index at the band edges. Consequently spin can be selectively excited through valley optical selection rule and intervalley scattering requires a simultaneous spin flip. This affords protection for both the spin and valley polarization, as a result, intervalley spin relaxation is expected to be slow [73]. In addition, the generation of a spin Hall effect is accompanied by a valley

Hall effect [75, 76]. The confinement of carrier populations to specific valleys in K -space through optical excitation alone may be the first step towards a new field of valleytronic devices [77-81].

1.4 LINEAR AND NONLINEAR STUDIES

Crucial in developing valleytronic devices is the ability to selectively excite and manipulate carriers in a specific valley, the viability of which depends on how robust and pure the valley selectivity is. Early work by Zeng *et al.* [82] used helicity-resolved PL to demonstrate a valley polarization of 30% in pristine monolayer MoS₂. The researchers were able to optically excite the monolayer MoS₂ with light of one helicity and detected the helicity of the PL response showing that 30% of the emitted light followed the helicity of the optical excitation. Cao *et al.* [83] were able to show a valley polarization of up to 50% in monolayer MoS₂. Although impressive, much better results have also been achieved. Mak *et al.* [84] found almost complete valley polarization in monolayer MoS₂ using helicity resolved PL and were also able to give a lower bound of 1 ns on the valley polarization, strongly reaffirming the viability of these materials in valleytronic devices. Similar results have been shown by Jones *et al.* on monolayer WSe₂ in which a valley polarization of 40% was measured.

In addition to an excellent degree of valley polarization achievable in these materials, recent studies have also shown that the valley polarization lifetimes can be on the order of picoseconds. Using time-resolved PL, Lagarde *et al.* [9] found exciton emission decay times of approximately 4 ps in monolayer MoS₂. Helicity-resolved, ultrafast pump-probe has shown that valley polarization is preserved for several picoseconds before scattering destroys the valley selectivity [85] while other ultrafast pump-probe experiments have shown polarization anisotropy to be completely lost within

400 fs [13]. As the current research suggests, there is still much to learn about the valley dynamics in these monolayer TMDCs.

Nonlinear studies on exciton dynamics have also employed incoherent spectroscopic techniques like pump-probe. Wang *et al.* [86] have found carrier lifetimes of 100 ps while other groups find population decays with fast and slow components of ~ 500 fs and 400 ps, respectively [11]. Shi *et al.* [10] have found decay dynamics even more complicated, measuring exciton population decay in monolayer MoS₂ with three different timescales: a fast decay of 2-4 ps, an intermediate decay of 30-80 ps, and a slow decay of 300-1000 ps. Despite the speed at which research into 2D TMDCs is progressing much more research is needed and many fundamental questions of the exciton dynamics remain unresolved, such as the degree to which radiative vs nonradiative pathways influences the carrier dynamics, the role of many-body effects in these materials, the role of excitation-induced dephasing (EID) and exciton-phonon interaction as well as the intrinsic homogeneous linewidth of the excitons. The future growth of these materials and their applications in new devices will rely heavily on our knowledge of these fundamental properties. Much of the research performed so far has been done using linear techniques such as time-resolved PL or nonlinear, incoherent spectroscopies such as pump-probe, leaving a wealth of information that can only be explored with coherent spectroscopies such as 2DCS.

1.5 2DCS ON TMDCs

Optical two-dimensional coherent spectroscopy (2DCS), an extension of three-pulse four-wave mixing (FWM), is a powerful tool that can overcome many of the limitations of simpler spectroscopies [87]. In pump-probe experiments and three-pulse FWM, often researchers use a broadband femtosecond or picosecond laser which can

excite multiple electronic transitions, resulting in complicated dynamics and oscillatory beats. With one-dimensional spectroscopies like pump-probe and FWM, it is often impossible to separate these electronic transitions or distinguish between quantum mechanical coupling or polarization interference as the cause of the oscillatory beats [88]. One-dimensional spectra can also exhibit very similar characteristics for very different phenomenon, such as inhomogeneity and dephasing, making it impossible to distinguish one from the other. The manifestation of many-body interactions such as local-field effects [89], excitation-induced dephasing [90], excitation-induced shift [91] and biexcitonic effects [92] can also be impossible to distinguish using incoherent spectroscopies.

2DCS grew out of the field of multidimensional nuclear magnetic resonance (NMR) [93] spectroscopy and is an optical analog of those spectroscopic techniques. It has been implemented in both the infrared and optical regimes to study the coherent, nonlinear response of a variety of systems and can provide a snapshot of coherent dynamics on femtosecond timescales. 2DCS has been routinely employed in non-collinear geometries allowing for spatial isolation of a background-free signal. By recording the FWM signal along a specific phase-matched direction, a variety of 2D spectra can be generated--each sensitive to specific dynamics and interactions--simply by changing the time ordering of pulses and taking the Fourier transform with respect to different delays. By coherently tracking the signal phase evolution while one pulse delay is scanned, 2DCS provides a large variety of advantages over one-dimensional spectroscopies. Congested one-dimensional spectra can be unfolded onto two dimensions, allowing for the identification of multiple resonances in the nonlinear response, revealing the nature of coupling between resonances and separating quantum mechanical coherent pathways. In one specific time-ordering in which a photon echo is

produced, the 2D spectrum can be analyzed in terms of its elongation along the diagonal and cross-diagonal in the spectral plot. By looking at the width of the signal along these two directions we are able to unambiguously separate the inhomogeneous and homogeneous broadening inherent in a system. The experiments outlined in this dissertation represent the first implementation of 2DCS on TMDCs and provides invaluable insight into the optoelectronic properties of these materials.

2DCS of monolayer TMDCs was implemented using the JILA **Multidimensional Optical Nonlinear SpectRometer** (MONSTR), designed by Bristow *et al.* [94] in 2009. The MONSTR is an ultrastable platform of nested and folded Michelson interferometers designed to take a single, pulsed laser input and produce four identical, phase stabilized pulses in a box geometry. Phase stability between the pulses are on the order of $\lambda/100$ and are maintained via active stabilization via feedback-assisted, interferometric monitoring. The delay between each pulse is varied with the use of translation stages with three of the pulses being used for excitation and the fourth pulse being used for spectral interferometry. This fourth pulse must necessarily be phase stable and co-propagate with the signal itself in order for a Fourier transform of the interferogram to be possible. The samples which were used to gather data were prepared using chemical vapor deposition (CVD) onto transparent sapphire substrates which resulted in monolayer WSe₂ domains of triangular shape and $\sim 10 \mu\text{m}$ in lateral size. Because of the density of the flakes and an excitation spot size of $30 \mu\text{m}$ diameter, more than one flake was excited at one time.

Despite multiple flakes in the excitation spot, the nonlinear signal was too weak to detect using lock-in amplifiers and an amplitude-modulated FWM signal. In addition to the weak signal, scattering of the excitation beams into the signal direction proved a significant problem. To address these issues we employed phase-cycling and spatial filtering which drastically reduced scattering to the point we could detect a nonlinear

signal. Once a signal was found, we performed one-quantum rephasing scans which represents a specific time-ordering of pulses where a photon echo signal is emitted after the arrival of the third pulse. Cross-diagonal slices of the spectra at a particular emission energy provides a measure of the homogeneous linewidth [95], inversely proportional to the dephasing time, whereas diagonal slices gives the amount of inhomogeneity in the system. The inhomogeneity of the system was found to be larger than the laser bandwidth, as determined by PL measurements, so the inhomogeneity in our 2D spectra was laser bandwidth limited. As a result, we focused solely on the cross-diagonal slices to find the homogeneous linewidth.

Cross-diagonal slices in the 2D spectrum were taken for a wide range of excitation densities, from $\sim 2.5 \times 10^{11}$ excitons/cm² to $\sim 17.5 \times 10^{11}$ excitons/cm², showing a linear trend of increasing homogeneous linewidth with increasing excitation density--a clear signature of excitation-induced dephasing (EID). The excitation density dependence of the homogeneous linewidth was then fit to a model, which we were then able to extract a zero-density homogeneous linewidth as well as an exciton-exciton interaction parameter. Not surprisingly, the interaction parameter was found to be quite large consistent with the reduced dielectric screening expected in monolayer TMDCs. All of the excitation dependent data were taken at a temperature of 10 K.

In order to probe exciton-phonon interactions, cross-diagonal slices were also taken as a function of temperature. The homogeneous linewidths were plotted as a function of temperatures ranging from ~ 5 K to ~ 50 K showing a linear increase in with increasing temperature. This data was then fit to a model and from this fit we were able to extract a value for the exciton-phonon coupling strength, yielding a value 5-10 larger compared to traditional semiconductor quantum wells and twice as large as bulk TMD InSe and a value for residual homogeneous linewidth at zero temperature. In addition,

using the data from the excitation density dependence as well as the exciton-phonon fit, we were then able to extract an intrinsic homogeneous linewidth free of exciton-exciton and exciton-phonon interactions. The intrinsic homogeneous linewidth found, coupled with population decay measurements, reveals TMDCs have very short lifetimes where the dominating factors are non-radiative population recombination occurring on sub-picosecond time-scales, exciton-excitons interactions and exciton-phonon interactions. Calculations further reveal inherently rapid radiative lifetimes in perfect 2D crystals makes monolayer TMDCs good candidates for optoelectronics requiring fast recombination dynamics, including high-speed detectors and optical switches.

1.6 DISSERTATION OUTLINE

The focus of this dissertation will be the optoelectronic properties monolayer TMDCs using optical 2DCS. Chapter 2 will discuss the physics of semiconductors and the optical properties of excitons in 2D systems. We begin the chapter with a discussion of excitons in bulk, then move onto excitons in monolayers and quantum wells as well as discussing their optical properties. In Chapter 3 we will discuss 2DCS and begin by giving a brief historical overview. We will then move on to discussing some simpler, yet related, spectroscopic techniques in order to better understand the more complicated 2DCS. We'll then discuss the nonlinear response function which describes the material response to an applied electric field as well as the optical Bloch equations and how we can use the simple diagrammatic approach of Feynman diagrams to quickly write down all the terms in the nonlinear response function. We'll conclude the chapter with an explanation of 2DCS as well as the different types of 2D spectra and how to interpret them. In Chapter 4 we will discuss the experimental apparatus beginning with an overview of the 2DCS platform called the JILA MONSTR. We will then discuss how the

sample was prepared and then conclude with how the data was taken, processed and noise filtered. Chapter 5 will deal with our experimental results on monolayer WSe₂. We'll begin by talking about the motivations behind the experiment then move on to the data that was taken. The chapter concludes with an overview of a calculation supporting our data. Chapter 6 will conclude the dissertation with an outline of future directions and possible avenues of exploration that we can easily pursue using the existing 2DCS setup.

Chapter 2: Semiconductor Theory of 2D Confined Systems

Two-dimensionally confined systems come in a large variety of materials and methods of growth, the most well known being the conventional quantum well semiconductors like GaAs/AlGaAs and GaSb/InAs. Of foremost interest to this thesis are the atomically thin Van-der-Waals materials, in particular the transition metal dichalcogenides (TMDCs) such as WSe₂ and MoS₂. Much like conventional quantum well heterostructures—which can be fabricated out of GaAs/AlGaAs, GaSb/InAs, or Si/GeSi—TMDCs can be grown using techniques such as chemical vapor deposition (CVD) or molecular beam epitaxy (MBE). In addition, because these materials are composed of monolayers stacked and bound together by weak Van-der-Waals interactions, they may also be mechanically exfoliated to produce very high quality monolayer samples, which is not possible using conventional semiconductor materials. TMDCs are composed of transition metal atoms, typically Mo or W, and chalcogen atoms, like S or Se, and have bandgaps in the range of 1-2 eV [96] compared to conventional quantum well heterostructures which have bandgaps that can be tuned through ranges as low as 0.2 eV all the way up to 6 eV [97].

This dissertation will focus on the 2D confined TMDCs like WSe₂ with many comparisons to more well-studied conventional quantum well heterostructures for context. We will first review condensed matter theory of bandstructures in bulk semiconductors. We will then look at exciton formation in these bulk materials and their optical properties. Lastly, we conclude with the optical properties of excitons in 2D confined materials.

2.1 BLOCH'S THEOREM

Semiconductors are crystalline structures whose atoms have tightly bound electrons that stay close to the nucleus as well as loosely bound outer electrons that are free to move about the crystal. These electrons move about in a periodic potential created by the crystal lattice of ion cores. This periodic potential has the property [97]

$$U(\mathbf{r} + \mathbf{R}) = U(\mathbf{r}), \quad (1)$$

where \mathbf{R} is any Bravais lattice vector. Inserting this into the Schrodinger equation gives

$$H\psi = \left(-\frac{\hbar}{2m} \nabla^2 + U(\mathbf{r}) \right) \psi = \varepsilon\psi. \quad (2)$$

Bloch's theorem states that eigenstates of this Hamiltonian have the form of a plane wave times a function with the periodicity of the Bravais lattice:

$$\psi_{n\mathbf{k}}(\mathbf{r}) = e^{i\mathbf{k}\cdot\mathbf{r}} u_{n\mathbf{k}}(\mathbf{r}), \quad (3)$$

where n is the band index and $u_{n\mathbf{k}}(\mathbf{r})$ has the same translational symmetry of the lattice, i.e.

$$u_{n\mathbf{k}}(\mathbf{r}) = u_{n\mathbf{k}}(\mathbf{r} + \mathbf{R}). \quad (4)$$

Because of the periodicity of the lattice, \mathbf{k} is confined to the first Brillouin zone to avoid redundancy. Bloch's theorem leads to a description of the electronic energy levels in a periodic potential in terms of a family of continuous functions $\varepsilon_n(\mathbf{k})$ with each continuous band indexed by n and having the periodicity of the reciprocal lattice.

The business of calculating the band structures of materials turns out to be a daunting task unless some approximations are made. A simplified treatment of the band

structure is referred to as the *tight-binding model* and relies on the assumption that there is little overlap between the electron orbitals of atoms separated by two or more lattice sites. Even for neighboring atoms, the tight-binding model assumes that the inner orbitals of each atom essentially have no overlap and it is only the outer orbitals that overlap to any significant degree. The first step in the tight-binding approximation is to replace the full crystal Hamiltonian with the Hamiltonian of a single atom plus a small perturbation that contains some information about the periodicity of the lattice. With this in mind we can write

$$H = H_{at} + \Delta U(\mathbf{r}), \quad (5)$$

and write the eigenfunctions as a linear combination of atomic orbitals (LCAO):

$$\psi(\mathbf{r}) = \sum_{\mathbf{R}} e^{i\mathbf{k}\cdot\mathbf{R}} \sum_n b_n \psi_n(\mathbf{r}), \quad (6)$$

where $\psi_n(\mathbf{r})$ are localized atomic wave functions and we sum over all \mathbf{R} vectors in the Bravais lattice and all n atomic orbitals. By inserting equation (5) into Schrodinger's equation for the entire crystal and multiplying the result by ψ^* we can obtain an eigenvalue equation that determines the coefficients $b_n(\mathbf{k})$ and the energies $\varepsilon(\mathbf{k})$ given by

$$\begin{aligned} (\varepsilon(\mathbf{k}) - E_m) b_m &= -(\varepsilon(\mathbf{k}) - E_m) \sum_n \left(\sum_{\mathbf{R} \neq 0} \int \psi_m^*(\mathbf{r}) \psi_n(\mathbf{r} - \mathbf{R}) e^{i\mathbf{k}\cdot\mathbf{R}} d\mathbf{r} \right) b_n \\ &+ \sum_n \left(\int \psi_m^*(\mathbf{r}) \Delta U(\mathbf{r}) \psi_n(\mathbf{r}) d\mathbf{r} \right) b_n + \\ &\sum_n \left(\sum_{\mathbf{R} \neq 0} \int \psi_m^*(\mathbf{r}) \Delta U(\mathbf{r}) \psi_n(\mathbf{r} - \mathbf{R}) e^{i\mathbf{k}\cdot\mathbf{R}} d\mathbf{r} \right) b_n. \end{aligned} \quad (7)$$

Using the assumption that our atomic levels are all well-localized, we can recognize that the first and third terms on the right are small because they involve orbitals at different sites, i.e. one at \mathbf{r} and another at $\mathbf{r}-\mathbf{R}$, and we can see that the second term is small because the atomic wave functions will be negligible at any distance at which $\Delta U(\mathbf{r})$ would deviate appreciably from the atomic potential. As a consequence we can conclude that

$$\varepsilon(\mathbf{k}) \approx E_m , \quad (8)$$

i.e. that the Bloch energies are very close to the orbital energies themselves. In practice one could calculate an s-band energy dispersion by setting $E_m = E_0$ and summing equation (7) over all the energies degenerate or close to E_0 , similarly if one wanted to calculate the energy dispersion for any other band.

2.2 EXCITONS IN BULK

Figure 2 shows the energy bands for bulk MoS₂ and bulk GaAs [96, 98]. Bulk GaAs is a direct-gap semiconductor and remains so even when confined to two dimensions, but many TMDCs (MoS₂, MoSe₂, WS₂, and WSe₂) have the unique property in that they transition from an indirect bandgap at the Γ -point to a direct bandgap at the K -point when going from bulk to monolayer. This transition can be attributed to confinement effects and hybridization between p_z and d orbitals at the Γ -points [16, 20, 45]. As a result of this transition the optical properties of the material change drastically. Because the minimum of the conduction band (CB) and the maximum of the valence band (VB) line up in k -space, an incoming photon with energy equal to the bandgap, E_B , can promote an electron from the valence band to the conduction band if the transition is dipole allowed without the need for phonons to mediate the transition. In indirect bandgap materials a

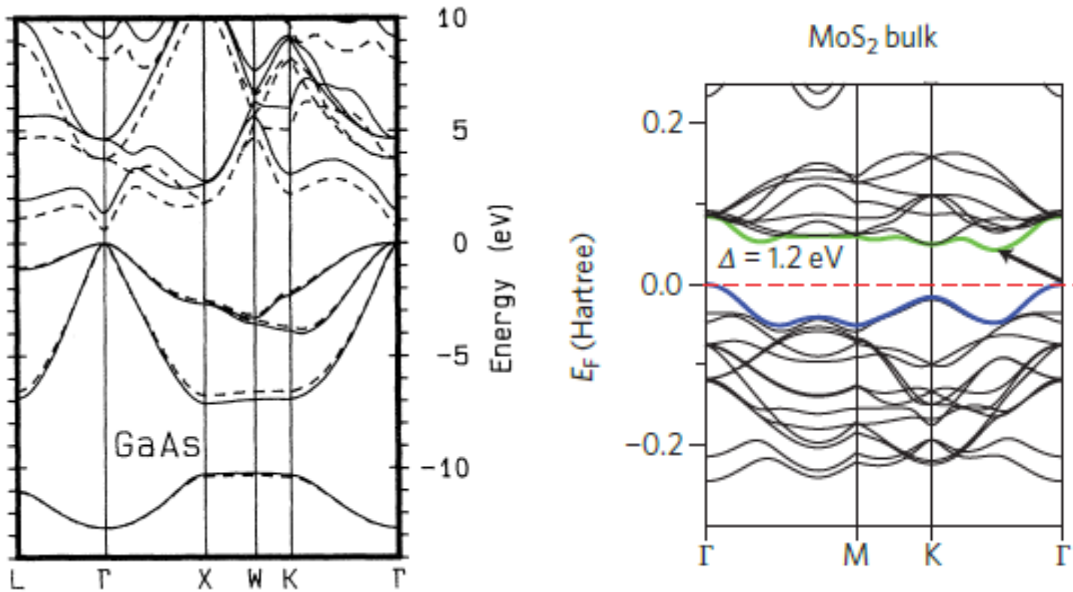


Figure 2:(Left) Two band structure calculations for bulk GaAs. The dashed lines represent the LDA calculations and the solid lines represent the GWA calculations [99]. (Right) Band structure of bulk MoS₂. The arrow shows the indirect gap at the Γ point [97].

phonon is required to conserve momentum since the incoming photon carries negligible momentum and the transition requires a large change in the electron wave vector.

Since the materials we study have direct bandgaps we will focus our attention there. Both GaAs and monolayer WSe₂ have dipole allowed transitions at their Γ -points and K -points, respectively, and during optical excitation with a photon of energy $h\omega > E_B$ an electron is promoted from the valence band to the conduction band leaving behind a hole in the valence band that behaves like a positively charged particle. For excitations such that $h\omega \approx E_B$, Coulomb forces between the positively charged hole in the valence band and the negatively charged electron in the conduction band must be included in order to accurately characterize the optical properties of these materials. The Coulomb interaction between electron and hole leads to the formation of quasiparticles called *excitons* which show up as strong absorption lines below E_B . Excitons may be

categorized into two types, Wannier-Mott excitons and Frenkel excitons. Wannier excitons have Bohr radii (defined as the mean distance between electron and hole) much larger than the length of the lattice unit cell, whereas Frenkel excitons have Bohr radii on the order of, or smaller than, the lattice unit cell (the latter being found in wide-gap semiconductors or some organic materials). The excitons in both GaAs and monolayer WSe₂ are Wannier excitons and are free to move about the entirety of the crystal as a bound pair [7, 97]. Wannier excitons are therefore sometimes called free excitons.

Because excitons consist of a positively charged hole and a negatively charged electron, their dynamics are very similar to a hydrogen atom and typically modeled in that fashion. The two systems have notable differences and therefore some modifications must be made. Firstly, the electron and hole exist in a medium with a high dielectric constant and so the binding energy will be much smaller. Secondly, since the electrons and holes move about in a lattice, and not free space, we must find their effective masses and use those to find the reduced mass that appears in the well-known results for the hydrogen atom. The effective mass near the bandgap minimum can be approximated by

$$m^* = \hbar^2 \left(\frac{d^2 E}{dk^2} \right)^{-1}. \quad (9)$$

The bands are parabolic for small k and therefore the dispersion relations can be approximated as

$$\begin{aligned} E_c(k) &= E_B + \frac{\hbar^2 k^2}{2m_e^*} \\ E_v(k) &= -\frac{\hbar^2 k^2}{2m_h^*}, \end{aligned} \quad (10)$$

where m_h^* and m_e^* are the effective masses for the hole and electron, respectively. The effective masses of both the electrons and holes will, in general, be much smaller than the

free space mass of an electron (e.g. $m_e^* = 0.067m_0$ for GaAs and $m_e^* = 0.45m_0$ for MoS₂) [99, 100].

In order to calculate how Coulomb attraction affects the linear optical properties of direct bandgap materials, we begin with the exciton wave function which is constructed from a linear combination of electron and hole Bloch functions

$$\Psi(\mathbf{r}_e, \mathbf{r}_h) = \sum_{\mathbf{k}_e, \mathbf{k}_h} \Phi(\mathbf{k}_e, \mathbf{k}_h) u_{c\mathbf{k}_e}(\mathbf{r}_e) e^{i\mathbf{k}_e \cdot \mathbf{r}_e} u_{v\mathbf{k}_h}(\mathbf{r}_h) e^{i\mathbf{k}_h \cdot \mathbf{r}_h}, \quad (11)$$

where $\Phi(\mathbf{k}_e, \mathbf{k}_h)$ is an expansion coefficient, \mathbf{k}_e and \mathbf{k}_h are the electron and hole wave vectors, and \mathbf{r}_e and \mathbf{r}_h are the electron and hole positions. Typically the atomic part of the Bloch wave functions, $u_{c\mathbf{k}_e}(\mathbf{r}_e)$ and $u_{v\mathbf{k}_h}(\mathbf{r}_h)$, vary slowly with \mathbf{k}_e and \mathbf{k}_h and therefore some simplifications can be made. When dealing with direct-gap materials, in which the bandgap minimum lies at the center of the Brillouin zone, we may set $\mathbf{k}_e = \mathbf{k}_h = 0$ in the atomic part of the exciton wave function leaving

$$\Psi(\mathbf{r}_e, \mathbf{r}_h) = u_{c0} u_{v0} \sum_{\mathbf{k}_e, \mathbf{k}_h} \Phi(\mathbf{k}_e, \mathbf{k}_h) e^{i\mathbf{k}_e \cdot \mathbf{r}_e} e^{i\mathbf{k}_h \cdot \mathbf{r}_h}. \quad (12)$$

It should be noted that for the TMDC materials we study this simplification is not strictly true since the direct bandgaps we probe lie at the edge of the Brillouin zone, but an *ab initio* analysis for these materials follows very closely to the one presented here [65, 101]. From equation (12) we can see that the exciton wave function consists of an envelope function

$$\Phi(\mathbf{r}_e, \mathbf{r}_h) = \sum_{\mathbf{k}_e, \mathbf{k}_h} \Phi(\mathbf{k}_e, \mathbf{k}_h) e^{i\mathbf{k}_e \cdot \mathbf{r}_e} e^{i\mathbf{k}_h \cdot \mathbf{r}_h}, \quad (13)$$

that describes the relative motion between the electron and hole on length scales larger than the lattice spacing as well as an Bloch functions, u_{c0} and u_{v0} , that modulate the envelope on the atomic scale. In order to describe the relative motion between electron and hole we can plug equation (13) into the two-particle Schrodinger equation and the problem follows the same procedure as the solution to the hydrogen atom energy levels, i.e. we can break the motion up into relative and center-of-mass coordinates. The center-of-mass motion is that of a free particle of mass $M = m_e + m_h$ and the relative motion of the excitonic wave function is described by the Wannier Equation

$$\left(-\frac{\hbar^2}{2m_r}\nabla_r^2 - \frac{e^2}{\epsilon_0 r}\right)\varphi(\mathbf{r}) = \mathcal{E}_r\varphi(\mathbf{r}) \quad (14)$$

$$m_r = \frac{m_e m_h}{m_e + m_h}$$

$$\mathbf{r} = \mathbf{r}_e - \mathbf{r}_h,$$

where m_r is the reduced mass, \mathbf{r} is the relative coordinate, and $\varphi(\mathbf{r})$ is the part of the exciton envelope function that strictly depends on \mathbf{r} . The Wannier Equation is mathematically equivalent to the Schrodinger equation and the results will be quoted here. The energy eigenvalues for the relative motion between the electron and hole are

$$\mathcal{E}_r \equiv \mathcal{E}_{n,l,m} = -\frac{m_r e^4}{2\hbar^2 \epsilon_0^2} \left(\frac{1}{n^2}\right) \equiv -E_{Rydberg} \left(\frac{1}{n^2}\right), \quad (15)$$

where $n = 1, 2, \dots$; $l = 0, 1, \dots, n - 1$; and $m = -l, \dots, l$ are the main, orbital and magnetic quantum numbers, respectively. Orbitals with $l = 0$ are referred to as s-orbitals and $l = 1$ as p-orbitals, etc. The exciton Rydberg energy, $E_{Rydberg}$, is often written in terms of the exciton Bohr radius

$$E_{Rydberg} = \frac{e^2}{2a_B \epsilon_0} = \frac{\hbar^2}{2m_r a_B^2} \quad (16)$$

$$a_B = \frac{\epsilon_0 \hbar^2}{m_r e^2} .$$

The total exciton energy is a sum of the bandgap energy, the exciton binding energy, and the center-of-mass kinetic energy.

In general, what one finds is that the larger the binding energy the smaller the Bohr radius. Some typical binding energies are 4.2 meV for bulk GaAs , 424 meV in bilayer MoS₂, and 50 meV for bulk MoS₂ [102]. In the monolayer limit, the binding energy for MoS₂ jumps dramatically to 897 meV compared to $k_B T = 25$ meV for room temperature [6]. Since phonon broadening can play a significant role in the width of exciton absorption lines, the binding energy alone is not a good indicator of whether or not exciton absorption will be resolvable up to room temperature.

Typical absorption spectra for bulk GaAs and a bulk TMDC is shown in Figure 3 as well as a schematic diagram (Figure 4) showing the absorption with and without Coulomb interactions. From Figure 4 we can see that the expected absorption spectrum is greatly modified when Coulomb interactions are included. Without Coulomb interactions the absorption follows a square-root law behavior

$$\alpha \sim (\hbar\omega - E_B)^{1/2}, \quad (17)$$

but instead exhibits sharp features below the bandgap that can only be explained with the inclusion of Coulomb interactions between electron and holes.

2.3 INFINITE AND FINITE WELLS

Our discussions so far have looked at excitons in bulk materials, but the optical absorption properties in 2D structures differs greatly in comparison to their bulk counterparts. For 2D materials, the differences between the bulk optical properties and the quantum confined optical properties will only become manifest when the confinement

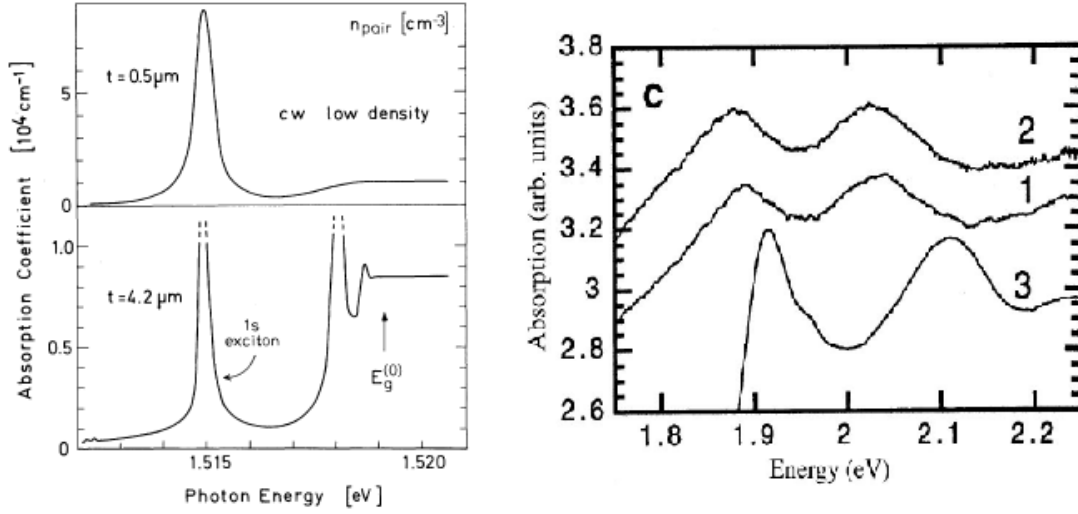


Figure 3: (Left) The top panel shows the low temperature linear absorption of 0.5 μm thick GaAs platelets and the bottom panel shows the linear absorption of a 4.2 μm thick GaAs sample [103]. (Right) Curves 1 and 2 shows the low temperature linear absorption of MoS₂ nanoparticles. Curve 3 is the linear absorption of bulk MoS₂ [104].

in one dimension satisfies the following criteria

$$\Delta x \leq \sqrt{\frac{\hbar^2}{mk_B T}}. \quad (18)$$

That is to say, the thickness of our 2D material must be equal to or smaller than the de Broglie wavelength for the thermal motion [100]. At room temperature and for a semiconductor with an electron mass of $0.1m_0$, Δx must be less than or equal to about 5 nm. In quantum heterostructures, this confinement is achieved by the potential barrier

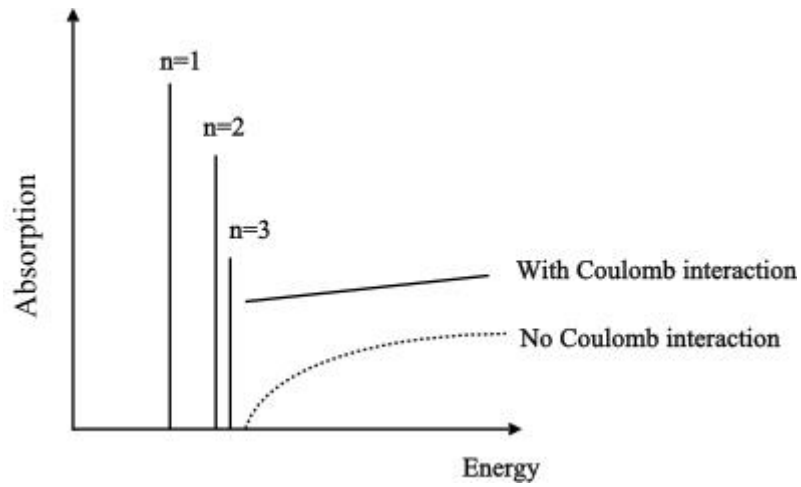


Figure 4: Schematic drawing of absorption with and without Coulomb interaction. The absorption follows a square root dependence with no Coulomb interaction.

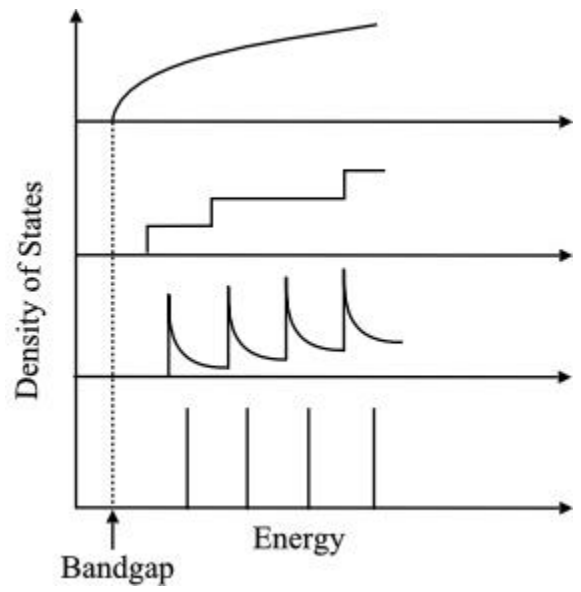


Figure 5: Schematic drawing of the density of states of (from top to bottom): bulk, quantum well, quantum wire, and quantum dot structures.

caused by bandgap discontinuities between two different materials, e.g. GaAs and AlGaAs. In TMDC materials this confinement is created by making the material very thin using mechanical exfoliation or simply by growing them to be atomically thin. The result of this confinement can be seen in Figure 5, which depicts the density of states of bulk, quantum well, quantum wire and quantum dot structures. In the absence of confinement the density of states can take on any value and increases like $(E - E_B)^{1/2}$. When confinement is introduced along one direction the density of states jumps in discrete steps and is independent of energy. Another consequence is that the bandgap increases as a result of the confinement and, as we'll see in the next few pages, the motion of the particles in the planar direction is unchanged from the bulk case, but the motion perpendicular to the plane is quantized.

The analysis for the electronic levels of a single particle in a quantum well is made much simpler by separating the problem into in-plane components and the out-of-plane component. In this vein, we may write the wave function in the form

$$\Psi(x, y, z) = \psi(x, y)\varphi(z). \quad (19)$$

The states of the system are then described by a wave vector \mathbf{k} that only includes the in-plane k_x and k_y components and the quantum number n that indicates the energy levels in the z direction. With the effective mass approximation we can then write the energy as

$$E^{total}(n, \mathbf{k}) = E_n + \frac{\hbar^2 \mathbf{k}^2}{2m^*}, \quad (20)$$

where E_n is often estimated by modeling the confinement potential as an infinite potential well. While a more accurate description of the confining potential would be a finite potential well, the infinite potential offers simplicity and is often a good starting point.

We first consider a single particle (electron or hole) in an infinite potential well. Outside the region from $-\frac{d}{2} < z < +\frac{d}{2}$ the potential is infinite and inside this region the potential is assumed to be zero. In this well-known problem we start with the Schrodinger equation for a single particle and note that since the potential is infinite outside the well the wavefunctions must go to zero at the boundaries, i.e. at $z = \pm\frac{d}{2}$. This leads to sine function solutions to the Schrodinger equation and energy levels

$$E_n = \frac{\hbar^2 k_n^2}{2m^*} = \frac{\hbar^2}{2m^*} \left(\frac{n\pi}{d}\right)^2, \quad (21)$$

where $n = 1, 2, 3 \dots$

The resulting energy levels tend to be quite far off for many confined 2D systems and the reason for this can immediately be understood when we remember that the model overestimates the confining potential and thus the quantization energies. The resulting energies from the infinite barrier model are closer for states with small quantization energies and materials with high potential barriers at the interface. Probably the most important result to note from the infinite potential barrier analysis is the fact that the energy level depends on the effective masses of the particles, i.e. heavier particles in the well will have a lower energy than lighter ones. In particular, this becomes important in GaAs/AlGaAs systems in which the heavy-hole band and light-hole band are no longer degenerate in a quantum well. The states can also be separated into their parities, states of odd n will have even parity whereas states of even n will have odd parity. This distinction becomes important later when we start looking at selection rules for allowed transitions.

We can adopt an even better model if we consider the confining potential as a finite barrier. This model starts with the assumption that the barriers have a height of

energy V_0 and from there it follows that the wavefunctions are non-zero outside of the confining potential. Because the wavefunctions are non-zero outside of the well we must include both sine and cosine solutions, rather than just sine solutions like in the infinite well model. The Schrodinger equation inside the well remains the same as in the infinite potential well, but outside the well the wavefunction is given by

$$-\frac{\hbar^2}{2m_b^*} \frac{d^2\varphi(z)}{dz^2} + V_0\varphi(z) = E\varphi(z), \quad (22)$$

which has solutions of the form

$$\varphi(z) = Ae^{\pm\kappa z}, \quad (23)$$

where κ is defined by

$$\frac{\hbar^2\kappa^2}{2m_b^*} = V_0 - E, \quad (24)$$

which tells us that the higher energy levels in the quantum well tunnel more into the barriers because the decay constant is smaller for these states. It's important to note that in equation (22) the effective mass that must be used is m_b^* which is the effective mass of the particle in the barrier material. Similarly, the effective mass in the Schrodinger equation for the well must be that of the well material itself. In general, the well and barrier will have different effective masses because of the different bandstructures of each material.

As we can see from equation (23), the wave functions must decay exponentially outside of the well. By applying appropriate boundary conditions at the well/barrier interface, that is

$$\varphi_w\left(\pm\frac{d}{2}\right) = \varphi_b\left(\pm\frac{d}{2}\right) \quad (25)$$

and

$$\frac{1}{m_w^*} \left(\frac{d\phi_w}{dz} \right)_{z=\pm d/2} = \frac{1}{m_b^*} \left(\frac{d\phi_b}{dz} \right)_{z=\pm d/2}, \quad (26)$$

we arrive at two transcendental equations for the energy eigenvalues, one for the cosine solutions and one for the sine solutions

$$\tan\left(\frac{kd}{2}\right) = \frac{m_w^* \kappa}{m_b^* k} \quad (27)$$

and

$$\tan\left(\frac{kd}{2}\right) = \frac{m_b^* k}{m_w^* \kappa}, \quad (28)$$

respectively. By substituting equations (21) and (24) into the last two equations we can eliminate k and κ and get equations (27) and (28) in terms of E

$$\begin{aligned} \sqrt{E^+} \tan\left(\sqrt{\frac{mE^+}{2\hbar^2}} d\right) &= \sqrt{V_0 - E^+} \\ -\sqrt{E^-} \cot\left(\sqrt{\frac{mE^-}{2\hbar^2}} d\right) &= \sqrt{V_0 - E^-}, \end{aligned} \quad (29)$$

where E^+ and E^- are the energy eigenvalues for the even and odd states, respectively.

These equations cannot be solved analytically, but can easily be solved graphically or numerically. Figure 6 shows the graphical solutions of equations (29) where the intersections are the allowed even and odd bound-state energies. It is clear from Figure 6 that if V_0 is less than the second lowest bound state in the infinite potential well, $n = 2$ in Equation (21), then only one bound state remains and it is an even state. For values of V_0 greater than zero then there is always at least one bound state. It's also clear to see from the equations that as the thickness d of the well is reduced the

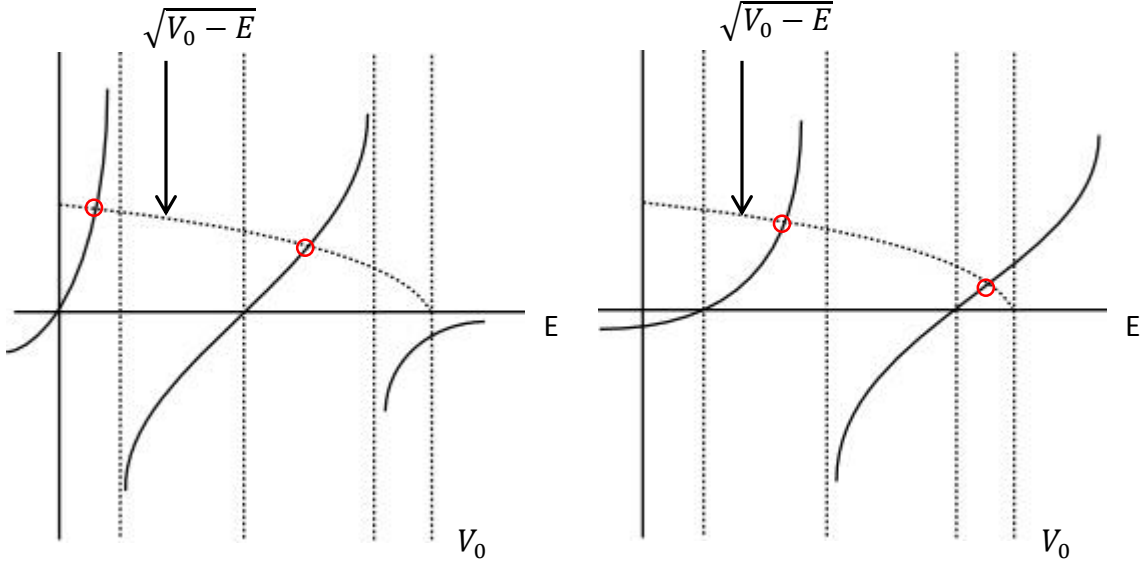


Figure 6: (Left) Graphical solution of allowed even bound-state energies. (Right) Graphical solution of allowed odd bound-state energies.

values for the bound state energies shift to higher energies. This blue-shift is the result of quantum confinement and can be used to tune the absorption properties of a quantum well itself.

2.4 EXCITONS IN TWO DIMENSIONS

Now that we have some understanding of how single particles behave in a quantum well we can look more closely at how excitons behave. The analysis for exciton dynamics in quantum wells follows closely to the analysis leading to equation (16), i.e. the dynamics in the plane are analogous to the hydrogen atom. The total Hamiltonian for the electron-hole pair in the quantum well is

$$H = -\frac{\hbar^2}{2m_e} \nabla_e^2 - \frac{\hbar^2}{2m_h} \nabla_h^2 + V_{confinement} + V_{Coulomb}. \quad (30)$$

Comparing this to equation (14) we can see that the only modification is the addition of the confinement potential. The problem is then broken up into the x and y directions that

are in the plane of the well and the z direction that is out of the plane. In the planar direction, as we did for the bulk case, we separate the motion into the relative and center of mass coordinates using the total and reduced masses of the electron-hole pair. For simplicity, we treat the confining potential in the z direction to be an infinite potential well and the energy eigenstates for the perpendicular direction are exactly that of equation (21) with the substitution of the reduced mass of the electron-hole pair. The solution of the two-dimensional Schrodinger equation for an electron-hole pair can be found in standard quantum optics textbooks and so will be quoted here [105]

$$\varepsilon_n^{2D} = E_g + \frac{\hbar^2 \pi^2 j^2}{2m_r d^2} - \frac{E_{Rydberg}}{\left(n_j - \frac{1}{2}\right)^2}, \quad (31)$$

where $n_j = 1, 2, 3 \dots$ and $E_{Rydberg}$ is the same as that found in equation (16). The second term is the confinement term where $j = 1, 2, 3 \dots$. We can see from the equation that at each j value we have an exciton series given by the third term which is almost identical to the exciton series in a bulk (see equation (15)) semiconductor except for the fact that now $n \rightarrow n - 1/2$. It is clear from equation (31) that for $n = 1$ the exciton energy in 2D systems is 4 times larger for the $n = 1$ state in bulk. More careful calculations that include imperfections in the quantum well actually predict enhancements smaller than 4 and closer to 2.5 times larger.

As one might expect, the Bohr radius is smaller in quantum wells compared to bulk. Similar to how we arrived at the first line in equations (16) we may write the 2D Rydberg energy in terms of the 2D Bohr radius

$$E_{Rydberg} = \frac{\hbar^2}{m_r (a_B^{2D})^2}. \quad (32)$$

Using the second line in equations (16) and the fact that the exciton energies are 4 times larger in two dimensions than three we can conclude that the Bohr radii in 2D systems are only half as big as their three-dimensional counterparts.

In the previous arguments we have assumed that the dielectric constants in both the well and barriers are the same which is a very good approximation when dealing with GaAs/AlGaAs, but not so when talking about transition metals. For cases in which the dielectric constant of the well is larger than that of the barriers, e.g. a thin semiconductor deposited on an insulating substrate, the exciton binding energy may be strongly enhanced by what is called the local field effect. For materials like transition metals, local field effects can play a big role in exciton binding energies [6, 106].

2.5 OPTICALLY CREATED EXCITONS

Largely missing from the discussion so far has been the interaction of these 2D materials with light, but in order to optically create excitons light must be absorbed and so the selection rules governing the light matter interaction will be discussed. Let us first evaluate the matrix elements for a transition from an initial state in the valence band to a final state in the conduction band

$$M = \langle f|x|i\rangle = \int \psi_f^*(\mathbf{r})x\psi_i(\mathbf{r})d^3\mathbf{r}. \quad (33)$$

In bulk materials the matrix elements for x, y and z are all equivalent, but in quantum wells only the in-plane directions are equivalent. For a quantum well we can consider the experimental setup in which the quantum well lies in the x - y plane and the light propagates in the z -direction (Figure 7) so that

$$\langle f|x|i\rangle = \langle f|y|i\rangle \neq \langle f|z|i\rangle. \quad (34)$$

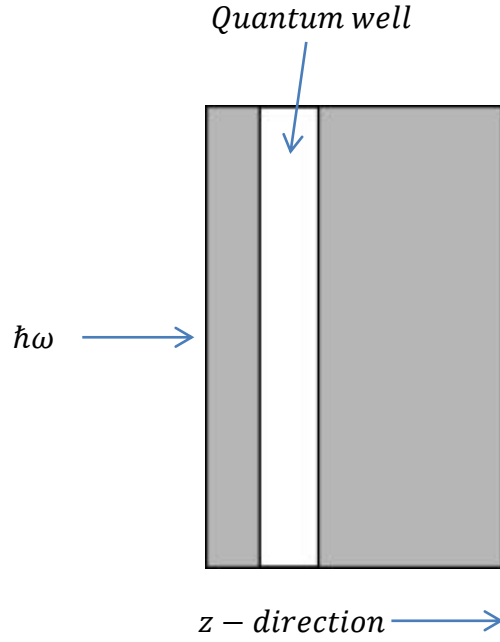


Figure 7: Coordinate system for light incident on a quantum well.

In order to evaluate the matrix elements of equation (33) we must write down the form of the initial and final states which we may do by using the Bloch formalism for the in-plane motion and the bound states for the out-of-plane motion

$$\begin{aligned}\Psi_i &\equiv |i\rangle = \frac{1}{\sqrt{A}} u_v(\mathbf{r}) \varphi_{hn}(z) e^{i\mathbf{k}_{xy} \cdot \mathbf{r}_{xy}} \\ \Psi_f &\equiv |f\rangle = \frac{1}{\sqrt{A}} u_c(\mathbf{r}) \varphi_{en}(z) e^{i\mathbf{k}'_{xy} \cdot \mathbf{r}_{xy}},\end{aligned}\tag{35}$$

where $u_v(\mathbf{r})$ and $u_c(\mathbf{r})$ are the envelope functions for the valence and conduction bands, $\varphi_{hn}(z)$ and $\varphi_{en}(z)$ are the bound states for the hole and electron, and finally $e^{i\mathbf{k}_{xy} \cdot \mathbf{r}_{xy}}$ and $e^{i\mathbf{k}'_{xy} \cdot \mathbf{r}_{xy}}$ are the plane waves for the in-plane motion of the hole and electron. We can make one small simplification here and set $\mathbf{k}_{xy} = \mathbf{k}'_{xy}$ since the photon will impart very little momentum. Plugging equations (35) into equation (33) we can separate the matrix

elements M into two parts, the valence-conduction band dipole moment and the electron-hole overlap

$$\begin{aligned} M_{cv} &= \langle u_c | x | u_v \rangle = \int u_c^*(\mathbf{r}) x u_v(\mathbf{r}) d^3\mathbf{r} \\ M_{nn'} &= \langle en' | hn \rangle = \int_{-\infty}^{+\infty} \varphi_{en'}^*(z) \varphi_{hn} dz . \end{aligned} \quad (36)$$

For the second equation in (36) we can plug in the sine function solutions for the infinite quantum well and recognize that the overlap factor

$$M_{nn'} = \frac{2}{d} \int_{-d/2}^{+d/2} \sin\left(k_n z + \frac{n\pi}{2}\right) \sin\left(k_{n'} z + \frac{n'\pi}{2}\right) dz \quad (37)$$

is zero for $n \neq n'$ and equal to one otherwise. This is not strictly true for real world systems where the well barriers are finite, but the transitions where $n \neq n'$ are still very weak and are strictly forbidden when Δn is odd since these involve states of opposite parity.

The selection rules just outlined gives a clear picture of what the absorption profile for 2D system should look like. The onset of absorption will only occur if the incoming photon has more energy than the bandgap of the well plus the additional energy that comes from confinement. Once the photon energy reaches this threshold then an electron from the valence band in the $n = 1$ state can be promoted to an $n' = 1$ level in the conduction band. By increasing the photon energy even more $\Delta n = 2, 3 \dots$ transitions can be excited and will show up as steps in the absorption profile (Figure 8).

In addition to the selection rules arising from the second equation in (36), we have selection rules from the conduction and valence band envelope functions. These selection rules are imbedded in the integral in the first equation of (36) and will not be calculated

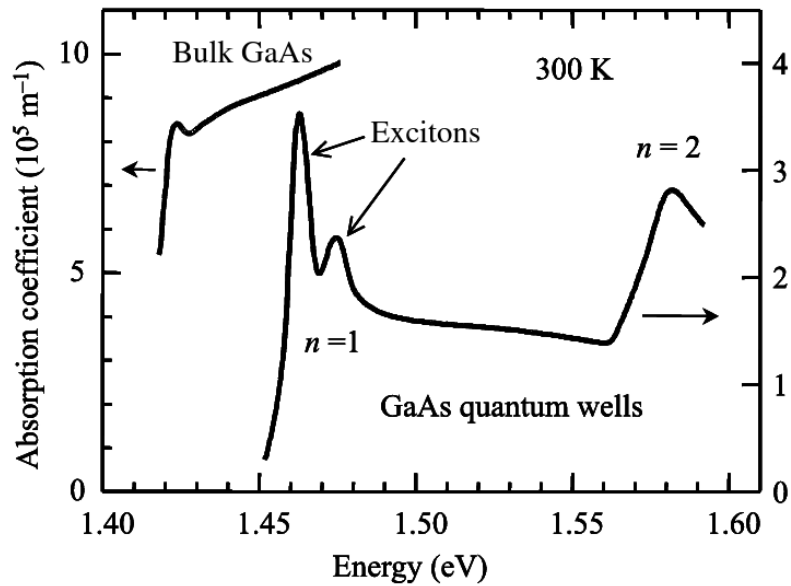


Figure 8: Linear absorption for bulk GaAs and a GaAs multiple quantum well [107].

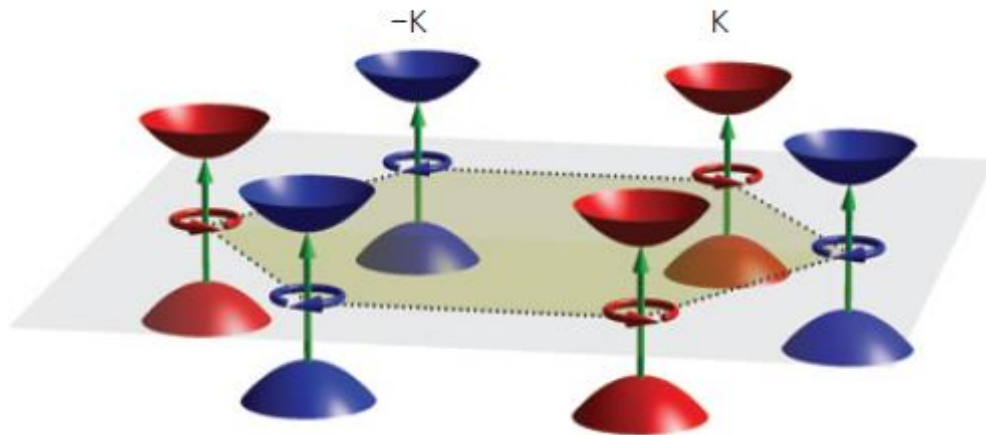


Figure 9: Blue (red) denotes electrons in the K (-K) valley. The valleys are the edges of the hexagonal Brillouin zone. The K (-K) valley only allows left (right) hand circular polarization for exciton formation [108].

here, but only the results discussed. The selection rules arising from this integral are determined by the type of orbitals that dominate the valence and conduction band

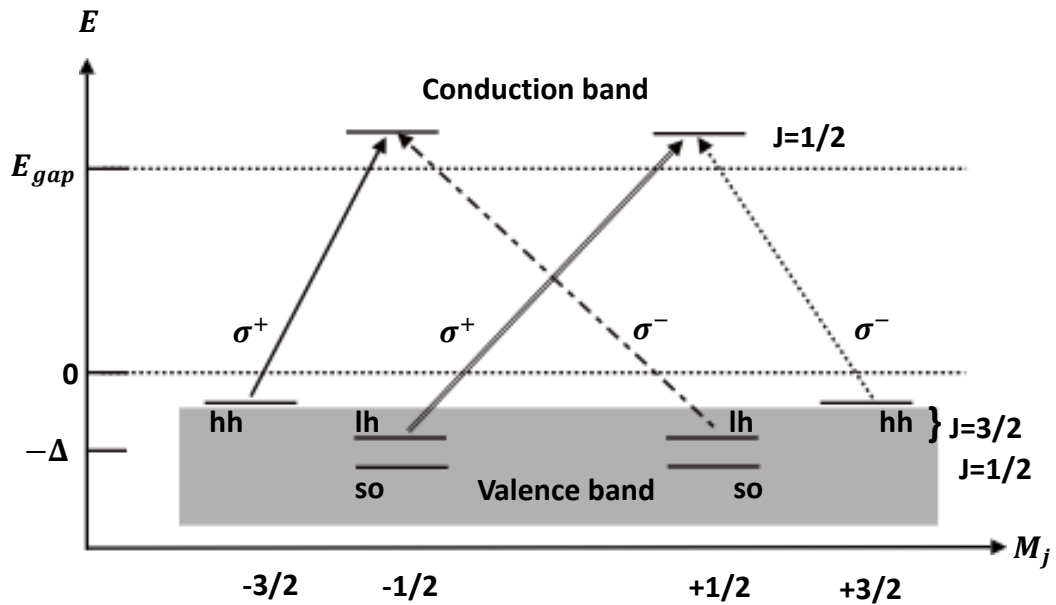


Figure 10: Selection rules for circularly polarized light in a quantum well with the zinc-blende band structure.

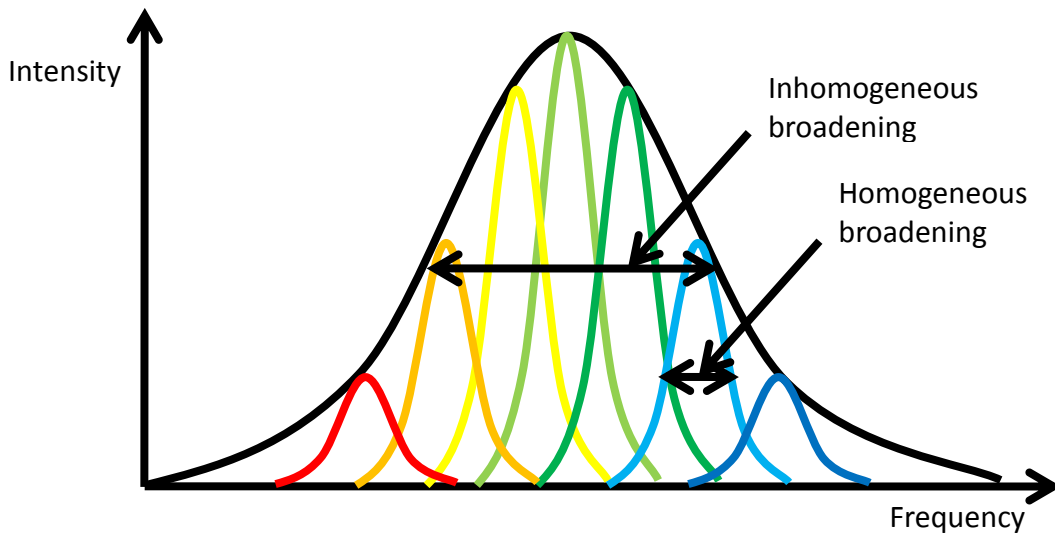


Figure 11: Homogeneous and inhomogeneous contributions to linewidths in linear absorption measurements.

envelope functions. For the TMDC materials we study the exciton absorption occurs, not near the Γ -point like in GaAs, but near the $\pm K$ -points in momentum space (Figure 9). In these materials the top of the valence band is dominated by d and p orbitals that

hybridize to form states with orbital angular momentum $m = 0$ for both the $+K$ and $-K$ valleys. The bottom of the conduction band is dominated by d orbitals with orbital angular momentum $m = 1$ and $m = -1$ for $+K$ and $-K$, respectively. The angular momentum selection rules therefore allow a transition, in the $+K$ and $-K$ valleys, upon absorption of only left-hand or right-hand circularly polarized light for each respective valley. The ability to selectively excite excitons in different valleys of k – *space* allows for the realization of “valleytronic” devices in which one can exploit the valley degree of freedom analogous to exploiting spin degrees of freedom [83].

The situation in III-V semiconductor quantum wells, like GaAs, is quite different due to the fact that the exciton absorption occurs, not at the edges of the Brillouin zone, but at the center. Whether using left or right-hand circularly polarized light, all the excitons will be created at the Γ -point. For GaAs, the valence band states are p -like in character and the conduction band states are s -like with the heavy-hole and light-hole excitons having $m = \pm 3/2$ and $m = \pm 1/2$ levels, respectively. The conduction band has states with orbital angular momentum $m = \pm 1/2$ states. Due to the lifting of the heavy-hole and light-hole bands that was seen in bulk GaAs, one can now theoretically create 100 percent spin polarized electrons (Figure 10) with σ^+ or σ^- corresponding to spin-up or spin-down electrons.

2.6 NON-IDEAL BEHAVIOR IN 2D MATERIALS

As is true with most systems, the theoretical behavior we’ve been discussing can be quite different than the real world behavior. Linear absorption results, like those shown in Figure 8, give very limited information regarding the exciton dynamics of the material. Often in optical measurements of excitons, what one is interested in is the homogeneous linewidth (Figure 11) of the exciton absorption which is often hidden in

linear absorption measurements. The homogeneous linewidth of the exciton transition is inversely proportional to the dephasing time (see Chapter 3) which determines how useful these materials can be for applications such as quantum information processing. In real-world 2D materials what often dominates the linear absorption spectrum is inhomogeneous broadening that occurs as a result of fluctuations in the local environments of the individual excitons. These fluctuations can be caused by inconsistent well-widths during the growth process or variations in stoichiometry or alloy composition across the sample. In Chapter 3 we will discuss many optical techniques that are routinely used on 2D materials and discuss their limitations. We will then move on to a discussion of nonlinear techniques aimed at understanding more about exciton dynamics and how one can use nonlinear spectroscopy to extract the inhomogeneous and homogeneous linewidths.

Chapter 3: Two-Dimensional Coherent Spectroscopy

Optical two-dimensional coherent spectroscopy (2DCS) is a powerful spectroscopic tool which borrows from techniques first developed in the 1970's in the field of nuclear magnetic resonance (NMR) [39] and has been used to study a wide variety of complex systems including liquids [109, 110], molecules [111-113], atomic vapors [114-117], semiconductor quantum wells [118, 119], and semiconductor quantum dots [120-126]. In contrast to linear spectroscopies, and even simpler nonlinear techniques, 2DCS enables tracking of the phase of the nonlinear response of the system with respect to two delays. By knowing the phase of the nonlinear response a Fourier transform may be taken with respect to the delays and a two-dimensional spectrum generated. Congested one-dimensional spectra are unfolded onto two dimensions allowing for the separation of inhomogeneous and homogeneous linewidths, isolation of coherent pathways, and coupling between resonances. Knowing the phase of the nonlinear signal also allows for the separation of the real and imaginary parts, yielding more information about microscopic details than spectroscopies that measure only magnitude. 2DCS has proven a powerful tool in studying a material's dephasing dynamics, population decay, and many-body dynamics.

In this chapter, we first start by giving a brief historical overview of the development of 2DCS from NMR and then we'll move on to discussing four-wave mixing. Next, we'll discuss the optical Bloch formalism and then the Feynman diagram approach to constructing the nonlinear response function. We will finish the chapter by making the transition from one-dimensional spectroscopy to two dimensions and the types of spectra that one can generate in 2DCS.

3.1 HISTORICAL OVERVIEW OF 2DCS

Multidimensional spectroscopy was first developed by the Ernst group in 1976 in the field of NMR [127]. At that time the Ernst group discussed the applications of two-dimensional spectroscopy in nuclear magnetic resonance and went into mathematical detail regarding the applications. As proof of principle, the researchers then applied two-dimensional spectroscopy to some simple spin systems. The work done by Ernst and his colleagues quickly drew the attention of researchers within and outside the field of NMR and shortly thereafter was extended to microwave frequency spectroscopy [128], 2D Raman spectroscopy of atomic vapors [129], and 2D IR spectroscopy [130]. 2D IR spectroscopy experiments were able to extend multi-dimensional techniques to very short wavelengths, elucidating properties of the structure of molecules by probing their vibrational modes and coupling [131, 132]. The technique was first used for probing electronic transitions by the Jonas group in 1998 [111]. Jonas and his colleagues studied a relatively simple system consisting of IR144 dye in methanol and were able to confirm their models with the data and were working at wavelengths around 800 nm. Some of the first studies on QW structures implemented multi-dimensional spectroscopies in both the time [88, 133] and frequency domains [134] and found temporal beating in the FWM signals which were thought to either arise from quantum interference or classical, macroscopic polarization interference. It was found that some systems, bound exciton resonances in CdSe for example, did indeed exhibit classical interference while other systems, such as light-hole and heavy-hole excitons in GaAs quantum wells, exhibited true quantum interference.

The early multi-dimensional spectroscopy done on semiconductor systems were, in fact, not 2DCS techniques, but multi-dimensional techniques in which the phase evolution of the nonlinear signal was not tracked. These early techniques were essentially

1D spectra incoherently stacked in order to generate a 2D spectrum. The first 2DCS studies done on semiconductor systems were done in 2005 by Borca *et al.* and investigated the role of many-body effects and unbound electron-hole pairs on the nonlinear response of excitons in GaAs quantum wells [135]. Borca and his colleagues were able to show the major role many-body interactions played in QWs by studying the off-diagonal features of the 2D spectrum. Follow up studies revealed that the dominant many-body interactions were excitation-induced dephasing and excitation-induced shift between excitons [118]. These studies also put constraints on microscopic many-body theories and served as guides to theories beyond the Hartree-Fock mean field limit [136].

In recent years 2DCS has pushed our knowledge of of electronic properties [120], exciton dephasing and relaxation dynamics [121, 122], exciton-exciton coherent coupling [126], $\chi^{(5)}$ optical nonlinearities [124], and exciton-biexciton correlated broadening [123].

3.2 FOUR-WAVE MIXING

The stepping stone to understanding 2DCS is to first understand simpler nonlinear spectroscopies such as pump-probe and transient FWM. These techniques are able to distinguish the difference between homogeneous and inhomogeneous broadening, which would be otherwise impossible in linear spectroscopy. In the systems we study, the dephasing dynamics of the excitons occur on timescales of hundreds of femtoseconds to tens of picoseconds and therefore what is required to study them are ultrafast nonlinear techniques to properly resolve the dynamics. In order to produce a nonlinear response, light of sufficient intensity is required, usually necessitating the use of a femtosecond pulsed laser. For light of such high intensity the response of the induced polarization in

the sample can no longer be modeled as linear to the incident electric field, but higher order terms must be included

$$P = \chi^{(1)} \cdot E + \chi^{(2)} \cdot E^2 + \chi^{(3)} \cdot E^3 + \dots , \quad (38)$$

where P is the induced polarization, E is the exciting electric field and $\chi^{(n)}$ is the n -th order susceptibility. In equation (38), we are ignoring the vector nature of E and P , which would necessitate $\chi^{(n)}$ to be an $n + 1$ order tensor. The $\chi^{(1)}$ term describes the linear response of the system and determines the absorption and refractive index. The $\chi^{(2)}$ term is the second order nonlinearity and is zero in materials that have inversion symmetry, the same is true for all even orders of $\chi^{(n)}$. For transition metal dichalcogenides, inversion symmetry is broken in the monolayer limit and so these materials do exhibit second harmonic generation (SHG) for monolayer as well odd layer thickness. Even layer thickness in these materials does not show appreciable SHG [137, 138]. For materials with inversion symmetry, the lowest order nonlinear response is the $\chi^{(3)}$ response which can be probed with pump-probe (transient absorption) and FWM. In these experiments two or, in the case of FWM, three fields act on the sample in order to produce the nonlinear signal. In the case of pump-probe, which only has two excitation fields, the pump acts twice. Quite often, these experiments are done in the time-domain or a mixture of the time and frequency domain. As is the case with our application of 2DCS, it is a mixture of time and frequency domain in which the nonlinear signal is spectrally resolved while a pulse delay is varied.

Pump-probe experiments can be spectrally resolved with the signal being sent to a spectrometer or they can be time integrated where the signal is sent to a single channel detector. These experiments are often done on-resonance with whatever transition is being probed, but can also be done off resonance. Pump-probe experiments measure

population dynamics and do so by measuring changes in the material absorption as a result of the pump. The pump, which is generally much more intense than the probe, is incident on the sample and creates an excited state population. The probe pulse then arrives at some time later and either experiences reduced absorption at the transition energy or can drive stimulated emission of the excited states. If the transition has not been saturated by the pump, the probe can also experience absorption by injecting more populated states. The lifetime and evolution of the populated states can be mapped out by scanning the probe from negative time delays to positive time delays. Timescales as long as hundreds of picoseconds are often needed in order for the population to decay to zero. Pump-probe experiments are not coherent measurements as it is the population that's being measured and not any coherent dynamics. Spectrally resolved pump-probe can still provide information about the many-body effects in a material since changes in the width of a transition or the energy at which the transition occurs will shed light on excitation induced broadening and excitation induced shifts.

In order to measure coherent dynamics in a system, FWM spectroscopy can be used. FWM experiments can be employed in a variety of ways, but the most basic form is degenerate FWM in which three pulse of equal frequency are incident on a sample and generate a fourth pulse which is the nonlinear signal. The first pulse is incident on the sample with wavevector \mathbf{k}_A and generates a coherent superposition between the ground and excited states. The second pulse with wavevector \mathbf{k}_B is incident on the sample and delayed by a time τ , this pulse converts the coherent superposition into a population of excited states. The population amplitude depends on the relative phase between pulse A and pulse B , being maximum when the two interfere constructively and minimum when the two interfere destructively. Pulses A , B and C can be collinear or, as is the case with many FWM experiments, they can be spatially separated. For spatially separated

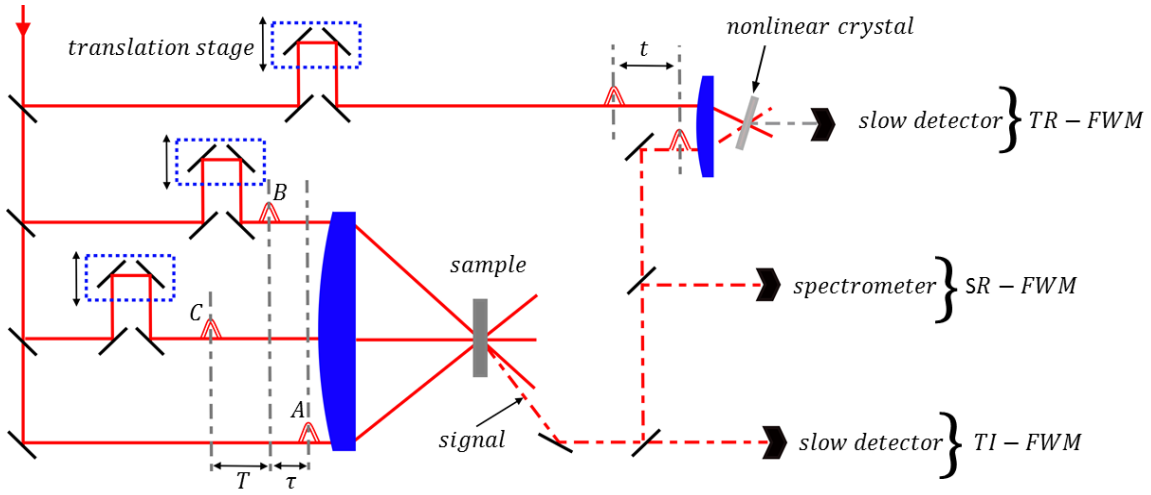


Figure 12: Schematic diagram of TI-FWM, SR-FWM and TR-FWM.

excitation beams, the constructive and destructive interference of beams A and B will vary across the sample and create a population grating. The third pulse, \mathbf{k}_C , arrives a time T later, with respect to the second pulse, and generates the nonlinear signal in the phase-matched direction, $\mathbf{k}_S = -\mathbf{k}_A + \mathbf{k}_B + \mathbf{k}_C$. Detecting the signal in this particular direction requires \mathbf{k}_A act as a conjugated pulse.

In the simplest FWM experiments, the pulse delays are as stated above, with pulse A arriving first and pulse C arriving last, but different dynamics can be probed by changing the pulse ordering. For example, by allowing pulse A to arrive last one can probe two-quantum coherences (discussed later in this chapter) which are sensitive to many-body effects not present in a simple independent two-level model. For the simple FWM experiment already described, information about dephasing and decoherence can be obtained by scanning the τ delay while information regarding incoherent population decay is gained by scanning the T delay.

3.3 TYPES OF FWM EXPERIMENTS

FWM experiments can be categorized into three different types (Figure 12): time-integrated (TI-FWM), time-resolved (TR-FWM), and spectrally-resolved (SR-FWM). One of the most common types of FWM experiments is TI-FWM in which the signal is sent to a single-channel, slow detector and is recorded for the duration of the emission time, t . The signal is recorded as a function of the delays τ and T and can be expressed as

$$S_{TI}(\tau, T) \propto \int_0^{\infty} |P^{(3)}(\tau, T, t)|^2 dt, \quad (39)$$

where $P^{(3)}(\tau, T, t)$ is the macroscopic third-order polarization. In the limit that the excitation pulses are much shorter than the dephasing and population decay the signal can be simplified to the following expression [139]

$$S_{TI}(\tau, T) \propto \theta(\tau)\theta(T)e^{-2\gamma\tau} \cdot e^{-\Gamma T}, \quad (40)$$

where $\theta(\tau)$ and $\theta(T)$ are the Heaviside step functions, γ is the dephasing rate and Γ is the population decay rate. The factor of two in the first exponent is applicable only in the limit that inhomogeneous broadening is smaller than the homogeneous linewidth. For systems in which inhomogeneous broadening dominates, the expression is

$$S_{TI}(\tau, T) \propto \theta(\tau)\theta(T)e^{-4\gamma\tau} \cdot e^{-\Gamma T}. \quad (41)$$

For systems with moderate inhomogeneity, where the homogeneous and inhomogeneous linewidths are comparable, the factor in front of γ is ambiguous, although it is quite often the case that inhomogeneous broadening is the dominated factor.

For inhomogeneously broadened systems, it's easy to see that dephasing will occur at a faster rate than homogeneously broadened systems because the oscillators have slightly different resonance frequencies. Inhomogeneously broadened systems can exhibit

what's called a photon echo in time-resolved experiments in which pulse A comes first and acts as the conjugated pulse. Photon echoes occur when the second and third pulses act to reverse the phase evolution of the oscillators, resulting in a signal that occurs at a time τ after the arrival of the last pulse, at which time the oscillators are back in phase again. TR-FWM can be implemented with the use of a reference pulse and spectrometer or a reference pulse and a nonlinear crystal. When using a spectrometer the signal and reference are delayed from each other and can then be Fourier-transformed into the time domain. If phase stability is maintained between all pulses then the nonlinear signal can be fully characterized, both real and imaginary parts, upon Fourier transform. Fourier-transforming is unnecessary when using a nonlinear crystal as the signal is mapped out directly in the time-domain via up-conversion in the nonlinear crystal. The signal can be written as

$$S_{TR}(\tau, T, t) \propto \int_{-\infty}^{\infty} |P^{(3)}(\tau, T, t')|^2 \cdot |E_{ref}(t - t')|^2 dt', \quad (42)$$

where E_{ref} is the electric field of the reference pulse. For SR-FWM the signal is sent directly to a spectrometer without the use of a reference pulse and can be written in the following way

$$S_{SR}(\tau, T, \omega_t) \propto \int_{-\infty}^{\infty} |P^{(3)}(\tau, T, t)|^2 \cdot e^{i\omega_t t} dt, \quad (43)$$

where ω_t is the emission frequency.

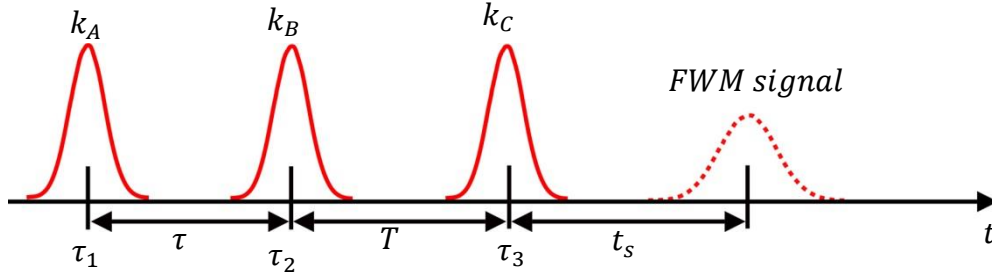


Figure 13: Pulse sequence in a FWM mixing experiment.

3.4 THE NONLINEAR RESPONSE FUNCTION

The polarization that appears in equations (39)-(43) is the only material dependent quantity that appears in the Maxwell equations for the signal and serves as the source for the radiation field. All material processes will therefore show up through their effect on the polarization alone and so calculating the polarization is the primary goal of any theory of optical spectroscopy and is key to interpreting optical measurements. The microscopic processes in the material are connected to the macroscopic polarization through the nonlinear response function. Consider a FWM experiment in which the three pulses are incident on the sample at times τ_1 , τ_2 , and τ_3 . This pulse sequence is shown in Figure 13. For a material with a purely linear response, we may write the polarization of the material as [140]

$$\tilde{P}^{(1)} = \epsilon_0 \int_0^{\infty} R^{(1)}(\tau) \tilde{E}(\mathbf{r}, t - \tau) d\tau , \quad (44)$$

where $R^{(1)}(\tau)$ is the linear response function and is assumed to be zero for $\tau < 0$, obeying the causality condition. In an analogous manner we may define the second-order and third-order response functions

$$\begin{aligned}
\tilde{P}^{(2)} &= \epsilon_0 \int_0^\infty d\tau_1 \int_0^\infty d\tau_2 R^{(2)}(\tau_1, \tau_2) E(\mathbf{r}, t - \tau_1) E(\mathbf{r}, t - \tau_2) \\
\tilde{P}^{(3)} &= \epsilon_0 \int_0^\infty d\tau_1 \int_0^\infty d\tau_2 \int_0^\infty d\tau_3 R^{(3)}(\tau_1, \tau_2, \tau_3) E(\mathbf{r}, t - \tau_1) E(\mathbf{r}, t \\
&\quad - \tau_2) E(\mathbf{r}, t - \tau_3) .
\end{aligned} \tag{45}$$

For the limit of a Dirac delta function excitation where the field envelopes are much shorter than the delay periods and material timescales, the time integrations can be eliminated. If we write the fields individually and explicitly

$$E(\mathbf{r}, t) = \mathbf{e}_i \mathcal{E}_i^+(t - \tau_i) e^{i(\mathbf{k}_i \cdot \mathbf{r} - \omega_i t)} + \mathcal{E}_i^-(t - \tau_i) e^{-i(\mathbf{k}_i \cdot \mathbf{r} - \omega_i t)} \tag{46}$$

then the third-order polarization can be written as [141]

$$\begin{aligned}
\tilde{P}^{(3)}(\mathbf{r}, t) &= R^{(3)}(\tau_1, \tau_2, \tau_3) \mathcal{E}_1^\pm \mathcal{E}_2^\pm \mathcal{E}_3^\pm e^{i(\pm \mathbf{k}_1 \pm \mathbf{k}_2 \pm \mathbf{k}_3) \cdot \mathbf{r}} e^{i(\pm \omega_1 \pm \omega_2 \pm \omega_3) t} e^{i(\pm \omega_1 \pm \omega_2 \pm \omega_3) \tau_3} \\
&\quad e^{i(\pm \omega_1 \pm \omega_2) \tau_2} e^{i(\pm \omega_1) \tau_1} ,
\end{aligned} \tag{47}$$

where $R^{(3)}$ is the third-order, nonlinear response function. The signal \mathbf{k}_s can propagate in any of the four phase-matched directions:

$$\begin{aligned}
\mathbf{k}_I &= -\mathbf{k}_1 + \mathbf{k}_2 + \mathbf{k}_3 \\
\mathbf{k}_{II} &= \mathbf{k}_1 - \mathbf{k}_2 + \mathbf{k}_3 \\
\mathbf{k}_{III} &= \mathbf{k}_1 + \mathbf{k}_2 - \mathbf{k}_3 \\
\mathbf{k}_{IV} &= \mathbf{k}_1 + \mathbf{k}_2 + \mathbf{k}_3 .
\end{aligned} \tag{48}$$

Equation (47) includes all possible permutations of the signal wavevectors, but the ones listed in equation (48) are the only ones that are not redundant. For a given pulse

ordering, each signal direction will correspond to a different physical process. For example, in a rephasing scan taken on an inhomogeneously broadened system a photon echo is expected to propagate in the \mathbf{k}_I but no signal is expected in the \mathbf{k}_{III} direction for a simple two-level system. Any signal in the \mathbf{k}_{III} can be attributed to many-body interactions and so for the materials we study a signal would therefore appear in this direction as well. It is often not possible, or prohibitively difficult to record the signal in all four directions. In practice, it is much simpler to change the time-ordering of the pulses while looking in the same direction for each time-ordering.

The full expression for the third-order polarization can be constructed using a simple diagrammatic approach that will be discussed later in this chapter. The diagrammatic approach uses double-sided Feynman diagrams and a sum-over-states to construct the response function. Before moving on to constructing the third-order response function, it is helpful to explain the optical Bloch equation formalism which will help us in understanding the nature of the perturbation theory behind the construction of the Feynman diagram approach.

3.5 THE OPTICAL BLOCH EQUATIONS

The optical Bloch formalism is a simple approach to analyzing and understanding the two-level system through the basic equations of motion. In the optical Bloch equations (OBE), we add phenomenological dephasing and depopulation and often ignore any effects of the bath. In this form, the OBEs are of very limited use in understanding systems with pronounced many-body effects, EID, or EIS, but can serve as an intuitive guide to interpreting 2DCS experiments and results. In order to account for these various effects often found in semiconductor systems, further phenomenological terms can be added [91] and often work quite well for describing semiconductor systems,

but for simplicity we will consider just a two-level system with only phenomenological dephasing and population decay.

The OBEs are derived using a density matrix approach. Suppose a system may be found in a state

$$\psi_s(\mathbf{r}, t) = \sum_n C_n^s(t) u_n(\mathbf{r}) \quad (49)$$

with a Hamiltonian given by

$$\hat{H} = \hat{H}_0 + \hat{V}(t), \quad (50)$$

where the $u_n(\mathbf{r})$ are the energy eigen-solutions to the time independent Schrodinger equation. These are assumed to be orthonormal and obey the relation

$$\int u_m^*(\mathbf{r}) u_n(\mathbf{r}) d^3r = \delta_{mn}. \quad (51)$$

The expectation value for any Hermitian operator can be expressed as

$$\langle A \rangle = \sum_{mn} C_m^{s*} C_n^s A_{mn}. \quad (52)$$

Using equation (52) we can define the elements of the density matrix as the expectation value of the Hermitian operator $p(s)$ which is the probability that the system is in a state s . This is written then as

$$\rho_{nm} = \sum_s p(s) C_m^{s*} C_n^s = \overline{C_m^{s*} C_n^s}, \quad (53)$$

where the overbar denotes an ensemble average over all possible states of the system. The density matrix can be interpreted in the following way: the diagonal elements of ρ_{nn} give the probability that the system is in an energy eigenstate n , while the off-diagonal elements give the probability that the system is in a coherent superposition of the states n and m .

The density matrix is useful in the sense that it can be used to calculate the expectation value of any observable quantity when the exact state of the system is unknown. This is in direct contrast to equation (52) which gives the expectation value for the observable A only in the case that the exact state of the system is known. The expectation value of the observable A , averaged over all possible states of the system, can then be written in various forms as

$$\langle \overline{A} \rangle = \sum_s p(s) \sum_{nm} C_m^{s*} C_n^s A_{mn} = \sum_{nm} \rho_{nm} A_{mn} = \text{tr}(\hat{\rho} \hat{A}). \quad (54)$$

In order to determine how the expectation value of any variable varies in time, it is thus necessary to determine how the density matrix evolves in time. This can be done by direct differentiation, which yields

$$\dot{\rho}_{nm} = \frac{-i}{\hbar} [\hat{H}, \hat{\rho}]_{nm}. \quad (55)$$

Equation (55) does not include any damping or population decay, but these terms can be added phenomenologically resulting in a modified equation of motion

$$\begin{aligned} \dot{\rho}_{nm} &= \frac{-i}{\hbar} [\hat{H}, \hat{\rho}]_{nm} - \gamma_{nm} \rho_{nm}, \quad n \neq m \\ \dot{\rho}_{nn} &= \frac{-i}{\hbar} [\hat{H}, \hat{\rho}]_{nn} + \sum_{E_m > E_n} \Gamma_{nm} \rho_{mm} - \sum_{E_m < E_n} \Gamma_{mn} \rho_{nn}. \end{aligned} \quad (56)$$

Here, Γ_{nm} gives the rate per atom at which population decays from level m to level n and γ_{nm} gives the damping rate of the ρ_{nm} coherence. The depopulation rates and dephasing rates are not independent of each other and are related in the following way

$$\gamma_{nm} = \frac{1}{2}(\Gamma_n + \Gamma_m) + \gamma_{nm}^{(col)} . \quad (57)$$

Here, Γ_n and Γ_m gives the total decay rates of population out of levels n and m , respectively. The last term in equation (57), $\gamma_{nm}^{(col)}$, is often called the pure dephasing rate and represents dephasing caused by elastic collisions or any process that is not associated with population transfer.

As an example, let us consider equations (56) in the context of a two-level system. For a simple two-level system with an applied field, the Hamiltonian is given by

$$H = H_0 + H_I = \begin{pmatrix} \hbar\omega_1 & V_{12} \\ V_{21} & \hbar\omega_2 \end{pmatrix} , \quad (58)$$

where H_0 is the free particle Hamiltonian with eigenenergies $\hbar\omega_1$ and $\hbar\omega_2$ for states $|1\rangle$ and $|2\rangle$, respectively. H_I is the interaction Hamiltonian that describes the dipole interaction with the applied field and can be written as $H_I = -\hat{\mu} \cdot E(t)$, where $\hat{\mu} = -e\hat{r}$ is the electric dipole operator. The off-diagonal elements of the interaction Hamiltonian have been set to zero under the assumption that states $|1\rangle$ and $|2\rangle$ have definite parity. We can insert this Hamiltonian into the equations of motion, i.e. equations (56), which gives the following

$$\begin{aligned} \dot{\rho}_{11} &= -\gamma_1 \cdot \rho_{11} + \frac{i}{\hbar} \cdot \mu_{12} E(t) \cdot (\rho_{12} - \rho_{21}) \\ \dot{\rho}_{22} &= -\gamma_2 \cdot \rho_{22} - \frac{i}{\hbar} \cdot \mu_{12} E(t) \cdot (\rho_{12} - \rho_{21}) \\ \dot{\rho}_{12} &= -\Gamma_{12} \cdot \rho_{12} + i\omega_0 \rho_{12} - \frac{i}{\hbar} \cdot \mu_{12} E(t) \cdot (\rho_{22} - \rho_{11}) , \end{aligned} \quad (59)$$

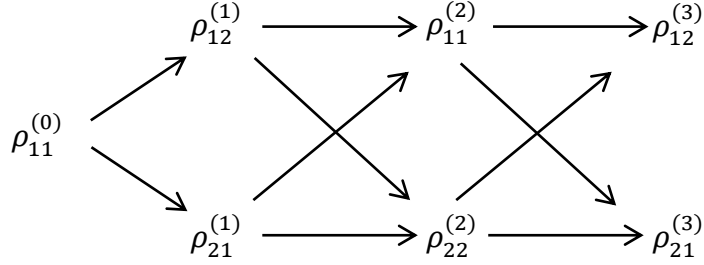


Figure 14: Schematic diagram showing the increase in perturbation order with each field interaction (represented here by arrows). Odd numbered field interactions produce polarization terms while even numbered field interactions produce population terms.

where $\omega_0 = (1/\hbar) \cdot (E_2 - E_1)$. Equations (59) do not include many-body effects, the inclusion of which would require numerical solutions of the equations. We ignore these effects here in the interest of simplicity and for the sake of developing intuitive insight into 2DCS. We can seek a simple perturbation expansion solution for equations (59) by first making the substitution in equations (59)

$$\frac{\mu_{12}E}{\hbar} \rightarrow \lambda \frac{\mu_{12}E}{\hbar}, \quad (60)$$

where λ is taken to be a small parameter ranging from zero to one that characterizes the strength of the interaction with the field. We now seek a solution in the form of a power series in λ —that is

$$\rho_{nm} = \rho_{nm}^{(0)} + \lambda \rho_{nm}^{(1)} + \lambda^2 \rho_{nm}^{(2)} + \dots \quad (61)$$

We require that equation (61) be a solution to equations (59) for any value of λ . In order for this condition to be true, the coefficients of each power of λ must satisfy equations

(59) separately. We can therefore plug equation (61) into equations (59) and gather like orders of λ giving

$$\begin{aligned}\dot{\rho}_{nm}^{(0)} &= -i\omega_{nm}\rho_{nm}^{(0)} - \gamma_{nm}(\rho_{nm}^{(0)} - \rho_{nm}^{(eq)}) \\ \dot{\rho}_{nm}^{(1)} &= -(i\omega_{nm} + \gamma_{nm})\rho_{nm}^{(1)} + i\hbar^{-1}[\mu_{12}E(t), \rho_{nm}^{(0)}]_{nm} \\ \dot{\rho}_{nm}^{(2)} &= -(i\omega_{nm} + \gamma_{nm})\rho_{nm}^{(2)} + i\hbar^{-1}[\mu_{12}E(t), \rho_{nm}^{(1)}]_{nm} ,\end{aligned}\tag{62}$$

and so on. Here $\rho_{nm}^{(eq)}$ is the equilibrium value that ρ_{nm} relaxes to at rate γ_{nm} as well as the steady-state solution, $\rho_{nm}^{(0)} = \rho_{nm}^{(eq)}$. We also assume, since γ_{nm} is a decay rate, that

$$\rho_{nm}^{(eq)} = 0, n \neq m .\tag{63}$$

Equations (62) can be integrated to find all the higher order corrections to the density matrix.

From equations (62), it is clear that interaction with the light field increases the order of the perturbation from $n - 1 \rightarrow n$. Further inspection of equations (62) also shows that for no interactions of the field the system starts in the population state $\rho_{11}^{(0)}$. For one interaction with the field the system is promoted to a first-order coherence state, $\rho_{12}^{(1)}$ or $\rho_{21}^{(1)}$. For two interactions with the field the system is promoted to a second-order population and so on. This can better be described with the diagram shown in Figure 14 where each arrow represents one interaction of the system with the field. As we'll see in the next section, the diagrammatic approach represented in Figure 14 is further expanded upon with the use of Feynman diagrams.

3.6 FEYNMAN DIAGRAMS

As we saw in the previous section, the density matrix can be found by performing a perturbation expansion which separates out the zeroth and all higher order corrections

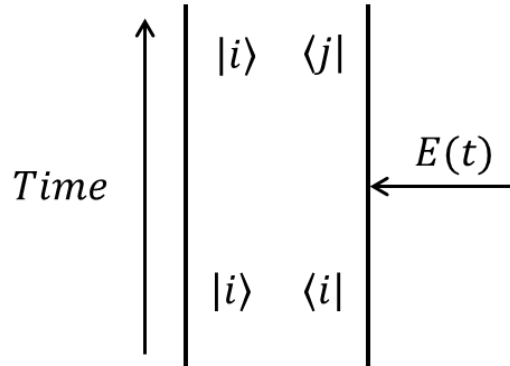


Figure 15: A Feynman diagram showing a single field interaction that promotes the state $|i\rangle$ to the state $\langle j|$.

to the density matrix. We then saw that each order of the density matrix can be built up one field interaction at a time and, in fact, different pathways can lead to the exact same density matrix term. In this section, we will see that the order in which these field interactions occur can be kept track of by using double-sided diagrams. Each diagram represents a different coherent pathway in the density matrix, often referred to as Liouville-space pathway. By adding up all the terms associated with each diagram, which amounts to summing the Liouville-space pathways, we can construct the nonlinear response function in a straightforward manner.

In order to understand Feynman diagrams--an example of which we show in Figure 15--we first write the density matrix in terms of $|\psi\rangle$ which represents the key vector for some state of the system

$$\hat{\rho} = \overline{|\psi\rangle\langle\psi|} , \quad (64)$$

where the overbar represents an ensemble average. Referring to Figure 15, one can see that Feynman diagrams are constructed by drawing vertical black lines where the vertical

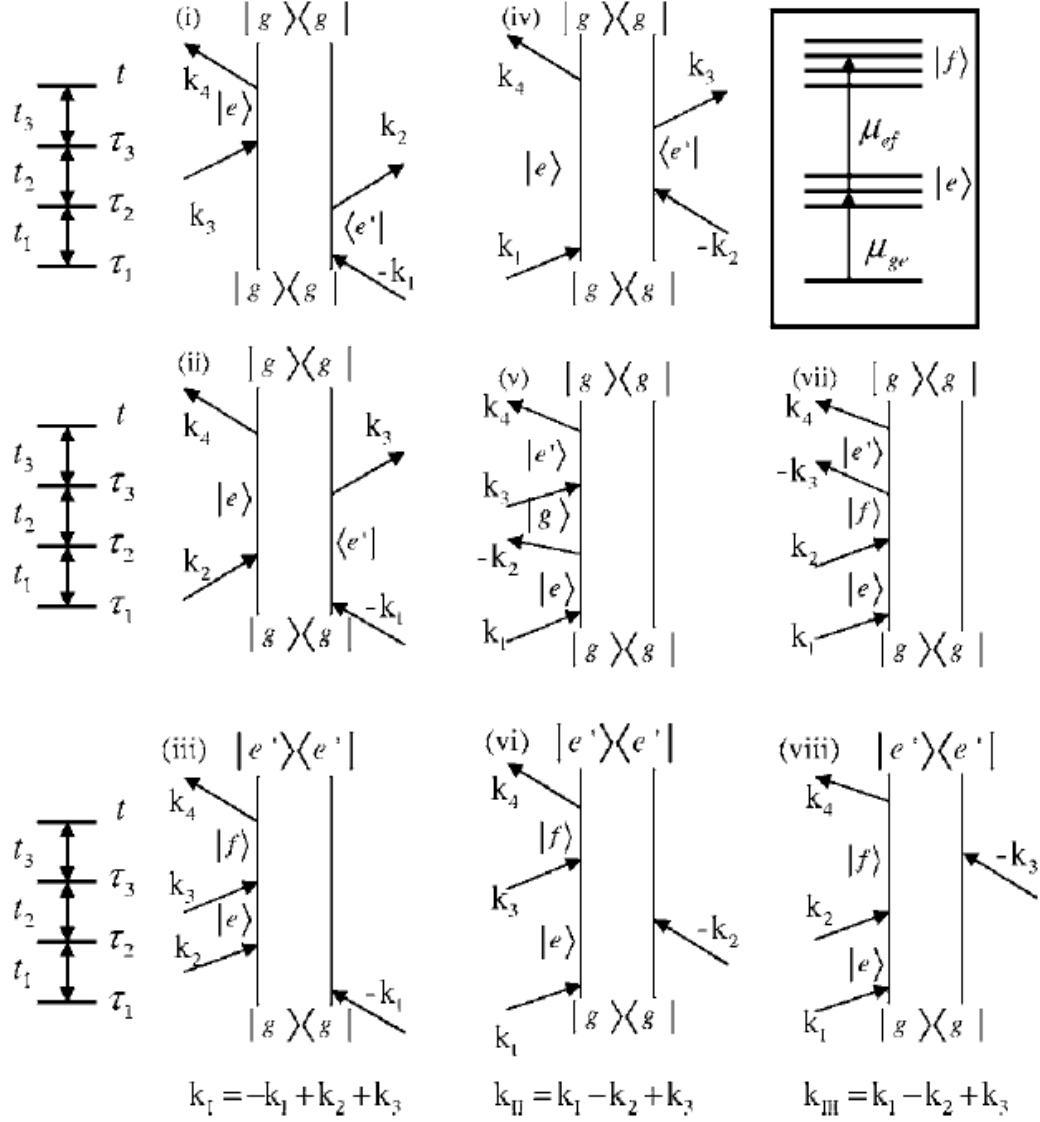


Figure 16: Feynman diagrams corresponding to different coherent pathways for the simple exciton level scheme shown in the top right. $|g\rangle$ is the ground state, $|e\rangle$ the excited state and $|f\rangle$ is the two-exciton manifold. μ_{ge} and μ_{ef} are the corresponding transition dipoles [141].

line on the left represents the “ket” in equation (64) and the vertical line on the right represents the “bra”. The state of the “bra” or “ket” may be changed by a field interaction which is represented by incoming or outgoing arrows. Arrows that occur farther down

along the vertical lines are field interactions that occur earlier in time and therefore time increases in the vertical direction as you go up on the diagram. Arrows pointing to the right indicates the interacting field has the form $\mathcal{E}_j^+ \exp(i\mathbf{k}_j \cdot \mathbf{r} - i\omega_j t)$ and arrows pointing to the left indicate the interacting field has the form $\mathcal{E}_j^- \exp(-i\mathbf{k}_j \cdot \mathbf{r} + i\omega_j t)$ where $\mathcal{E}_j^- = (\mathcal{E}_j^+)^*$. An arrow pointing towards the vertical line indicates absorption of a photon and an arrow pointing away indicates photon emission. Each arrow represents an increase of one in the order of the perturbation expansion. For example, a diagram with only one arrow represents a coherent pathway in the $\rho^{(1)}$ order of the perturbation expansion. To obtain higher order terms in the perturbation expansion of the density matrix, one can concatenate the Feynman diagrams by stacking them on top of each other. The wavevector of each diagram is simply the sum of the wavevectors associated with each vertex. The overall sign of each diagram is given by $(-1)^m$ where m is the number of vertices on the right hand side of the diagram since each interaction with the “bra” introduces a minus sign.

As an example of constructing the nonlinear response function from double-sided Feynman diagrams we refer to Figure 16 which shows the third-order Feynman diagrams for a simple two-band model (upper right). Each of the three columns represents signals that would propagate in different directions according to the wavevector of the given diagram. We may denote the signal field amplitudes generated along any particular direction \mathbf{k}_j as S_j , where $j = I, II, III$, and IV correspond to each of the wavevectors given in equation (48). From equation (47) we may write the signal field amplitude for I as [141]

$$S_I(t_3, t_2, t_1) = iR_I^{(3)}(t_3, t_2, t_1) \mathcal{E}_3^+ \mathcal{E}_2^+ \mathcal{E}_1^- e^{i(-\omega_1 + \omega_2 + \omega_3)t_3} \cdot e^{i(-\omega_1 + \omega_2)t_2} e^{-i\omega_1 t_1} , \quad (65)$$

where the fields \mathcal{E}_n^\pm and frequencies $\pm\omega_n$ are determined through inspection of the Feynman diagrams and t_1, t_2 , and t_3 are the times in which the three pulses are incident on the sample. The signs are determined quite easily, for example, ω_1 carries a negative sign throughout because the arrow is situated on the left-hand side in every diagram that appears in the first column. The signal fields for *II*, *III*, and *IV* are found similarly, but in some cases some of the nonlinear response functions may be ignored if they contain highly oscillatory terms that appear in the denominator for the signal field expression. Such is the case for the $R_{IV}^{(3)}$ term, which may be ignored in what's referred to as the rotating wave approximation (RWA).

For the simple two-band model shown in Figure 16, we can see three manifolds: the ground state (*g*), the single-exciton state (*e*), and the two-exciton state (*f*). The dipole operator only connects *g* to *e* and *e* to *f*. Let us now write down the nonlinear response function $R_I^{(3)}$ which will contain three terms in the summation each corresponding to a diagram in the first column of Figure 16.

$$\begin{aligned}
R_I^{(3)}(t_3, t_2, t_1) = & i^3 \sum_{e, e'} (\mathbf{e}_1 \cdot \boldsymbol{\mu}_{ge'}) (\mathbf{e}_2 \cdot \boldsymbol{\mu}_{e'g}) (\mathbf{e}_4 \cdot \boldsymbol{\mu}_{ge}) (\mathbf{e}_3 \\
& \cdot \boldsymbol{\mu}_{eg}) e^{-(i\omega_{eg} + \Gamma_{eg})t_3 + \Gamma_{gg}t_2 + (i\omega_{e'g} - \Gamma_{e'g})t_1} \\
& + i^3 \sum_{e, e'} (\mathbf{e}_1 \cdot \boldsymbol{\mu}_{ger}) (\mathbf{e}_3 \cdot \boldsymbol{\mu}_{e'lg}) (\mathbf{e}_4 \cdot \boldsymbol{\mu}_{ge}) (\mathbf{e}_2 \\
& \cdot \boldsymbol{\mu}_{eg}) e^{-(i\omega_{eg} + \Gamma_{eg})t_3 - (i\omega_{eer} + \Gamma_{eer})t_2 + (i\omega_{e'lg} - \Gamma_{e'lg})t_1} \\
& - i^3 \sum_{e, e'} (\mathbf{e}_1 \cdot \boldsymbol{\mu}_{ger}) (\mathbf{e}_4 \cdot \boldsymbol{\mu}_{e'lf}) (\mathbf{e}_3 \cdot \boldsymbol{\mu}_{fe}) (\mathbf{e}_2 \\
& \cdot \boldsymbol{\mu}_{eg}) e^{-(i\omega_{fer} + \Gamma_{fer})t_3 - (i\omega_{eer} + \Gamma_{eer})t_2 + (i\omega_{e'lg} - \Gamma_{e'lg})t_1} ,
\end{aligned} \tag{66}$$

where the \mathbf{e}_n are the polarization vectors for the three fields, $\omega_{vv'} = \varepsilon_v - \varepsilon_{v'}$ is the frequency of the transitions, and $\Gamma_{vv'}$ are the dephasing rates of the transitions. This result

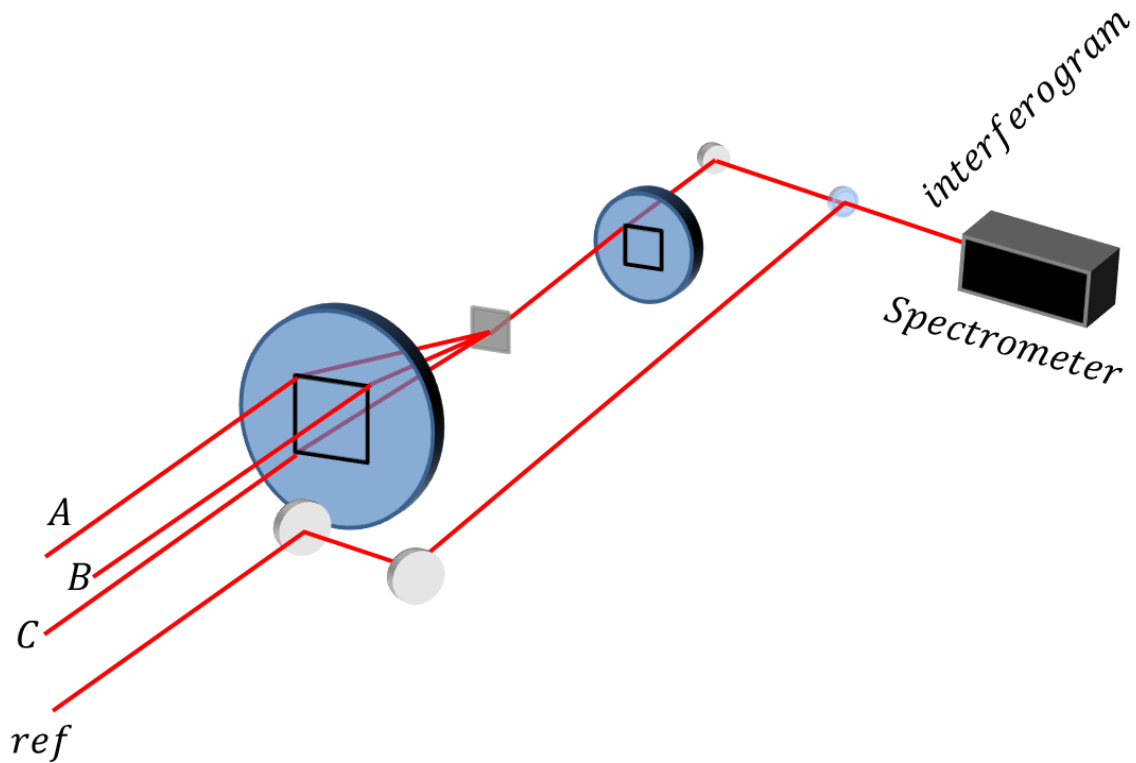


Figure 17: Schematic of box geometry setup. The reference is routed around and recombined with the signal and the interferogram is sent to a spectrometer.

can then be inserted into equation (47) to find the induced macroscopic polarization, which can then be inserted into Maxwell's equations in order to find the radiated FWM field.

3.7 2D SPECTROSCOPY

So far we have discussed FWM and with a good understanding of FWM and Feynman diagrams we may now develop some intuition for 2DCS. 2DCS is nothing more than an advanced FWM spectroscopic technique in which the time-delays are stepped with phase stable precision and the complex FWM field is measured through spectral interferometry.

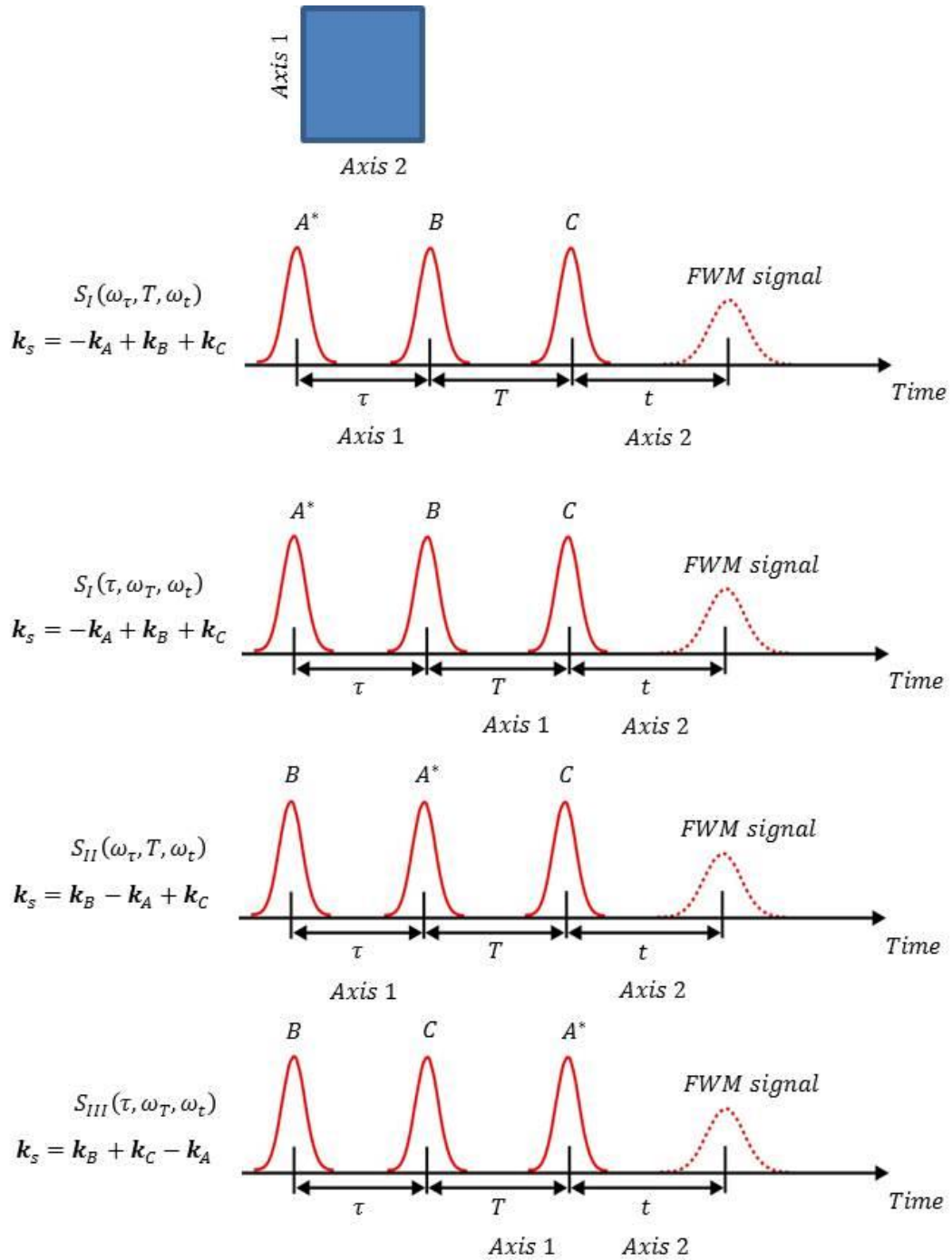


Figure 18: Possible pulse time orderings for three pulse 2D experiments.

2DCS can be implemented in many ways, some of the most common approaches use passive stabilization of the pulse delays through common path optics [142-144], pulse shaping methods [145, 146] and active phase-stabilization using a reference laser and feedback electronics [147, 148]. Each experiment can employ different geometries that range from completely collinear--which is to say that all the excitation beams copropagate--to geometries in which none of the beams are propagating along the same path. The most common of the beam geometries, and the one employed in our experiment, is the box geometry shown in Figure 17. In this configuration, three beams propagate along the corners of a box and are then focused onto the sample. These beams, with wavevectors $\mathbf{k}_a, \mathbf{k}_b,$ and $\mathbf{k}_c,$ induce a nonlinear signal that propagates in the phase-matched direction $\mathbf{k}_S = -\mathbf{k}_A + \mathbf{k}_B + \mathbf{k}_C,$ which is along the fourth corner of the box. The beams are delayed with respect to each other with the first delay labeled $\tau,$ the second $T,$ and the third t (delay t_s in Figure 13) . By interfering the FWM with a phase-stabilized reference pulse and sending both into a spectrometer, we can perform spectral interferometry and obtain one axis, the t axis, of the 2D spectrum without having to Fourier transform. In order to build up the full 2D spectrum we can step either of the other two delays, τ or $T,$ and perform a Fourier transform with respect to the stepped delay. For example, if we were to step the τ delay, the amplitude and phase of the 2D spectrum from the emitted signal field $E(\tau, T, t)$ would look like

$$S(\omega_\tau, T, \omega_t) = \int_{-\infty}^{\infty} E(\tau, T, \omega_t) e^{i\omega_\tau \tau} d\tau \quad (67)$$

for a fixed value of $T.$ In equation (67), the Fourier transform is already performed for the t axis through use of spectral interferometry.

3.8 TYPES OF 2D SPECTRA

Because we can vary the delay between each of the three excitation pulses, we have the ability to probe different microscopic processes that propagate along the phase matched direction \mathbf{k}_s . This is simply done by varying the pulse ordering of the incident fields. Examples of the different 2D spectra that's possible in such a setup is shown in Figure 18. The axes which are Fourier transformed are labeled as “Axis 1” and “Axis 2” in the figure.

By far, the most common spectrum to take, and the one we have employed to study TMDCs, is the $S_I(\omega_\tau, T, \omega_t)$ scan, also known as a rephasing one-quantum spectrum. In this spectrum the FWM signal is recorded while the delay τ is scanned and the delay T is held fixed. The FWM field $E(\tau, T, \omega_t)$ is Fourier transformed with respect to τ to generate the rephasing one-quantum spectrum that correlates the excitation frequencies, ω_τ , with the emission frequencies, ω_t . Coherently tracking the phase of the signal as the delay τ is scanned with sub-cycle precision permits the Fourier transform operation of the emitted FWM field, thus congested one-dimensional spectra can coherently be unfolded onto two frequency dimensions.

To understand why coherent tracking of the signal phase is so powerful, consider the FWM signal that is emitted from a transition with angular frequency ω_{ik} due to excitation of a transition ω_{ij} by the first pulse. If the first pulse is the conjugated field, as in the case of an $S_I(\omega_\tau, T, \omega_t)$ scan, then the signal field can be written [135]

$$S(\tau, t) = D(\tau, T, t) \mu_{ij}^2 \mu_{ik}^2 e^{i(\omega_{ij}\tau - \omega_{ik}t)}, \quad (68)$$

where μ_{ij} and μ_{ik} are the dipole moments of the respective excitation and emission transitions and the decay dynamics and the evolution of the system between the second and third pulses are lumped into $D(\tau, T, t)$. Equation (68) shows that the phase evolution

between the first two pulses results in a constant overall phase in the emitted field, i.e. as τ and t increase the phase is held constant. Therefore, by coherently tracking the phase of the emitted signal and by keeping sub-wavelength stability between the individual excitation pulses, we can simultaneously determine the frequency of the absorbing and emitting transitions. For two-level systems where $\omega_{ij} = \omega_{ik}$, the 2D spectrum will show a signal along the diagonal and for systems in which $\omega_{ij} \neq \omega_{ik}$, e.g. three-level systems, part of the signal will appear off-diagonal as well.

One of the advantages of the three-pulse technique is that we can probe very different microscopic processes by simply reordering the pulses in time. The phase evolution described by equation (68) happens when the conjugated pulse arrives first which creates a coherent superposition between the ground and excited state of the transition. The oscillators in the ensemble then dephase during the evolution period τ provided that there is some inhomogeneous broadening in the system. The second pulse converts the coherence into a population of ground states and excited states which do not accumulate phase during the period T , but simply decays at some characteristic rate. The third pulse then creates a conjugated phase evolution during the emission time t , which causes the oscillators to reverse their phases and come back into phase. This rephasing takes a time τ , the time in which the oscillators were allowed to dephase, and thus a photon echo signal is observed a time τ after the third pulse hits the sample. If we were to allow the second pulse to come first, then followed by the conjugated pulse as depicted in the third schematic of Figure 18, we could perform a “non-rephasing” scan. In the case of a non-rephasing $S_{II}(\omega_\tau, T, \omega_t)$ scan, the complex signal field would have the form

$$S(\tau, t) = D(\tau, T, t) \mu_{ij}^2 \mu_{ik}^2 e^{-i(\omega_{ij}\tau + \omega_{ik}t)} . \quad (69)$$

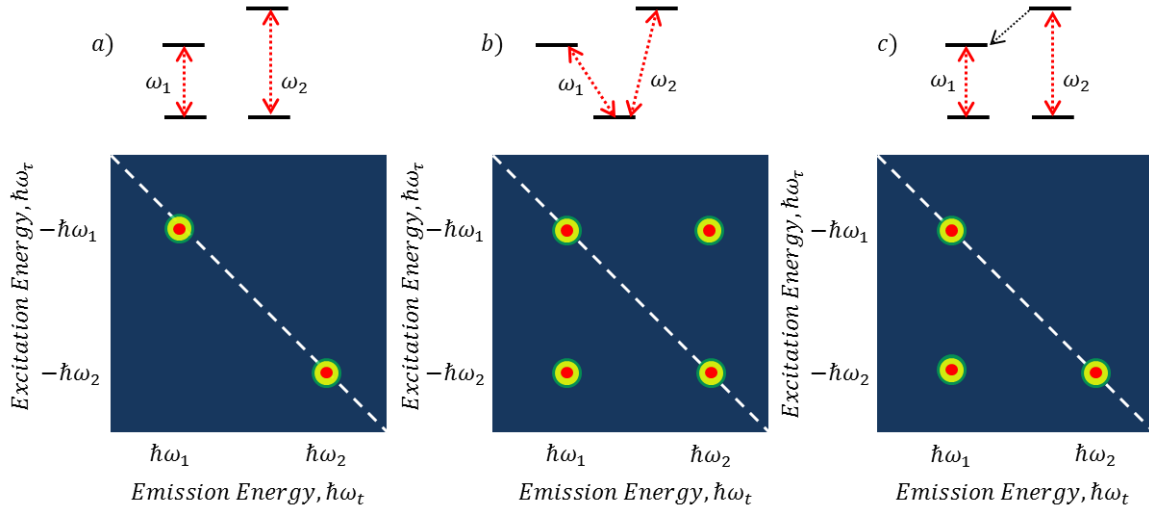


Figure 19: Schematic rephasing spectra for a) two independent two-level transitions b) a three-level system with a common ground state and c) two independent two-level systems that are coupled through incoherent relaxation from the higher energy transition to the lower energy transition.

Delay τ is defined as the difference between pulse B and A , therefore τ is positive for the rephasing scan and negative for the non-rephasing scan. From equation (69), it is clear to see that instead of a photon echo appearing at time τ after the third pulse, there is a polarization decay in the phase evolution of the system. By comparing both the non-rephasing and rephasing scans, important insight into the inhomogeneous broadening of the system can be gained.

In addition to the rephasing and non-rephasing one quantum scans in which the τ delay is scanned, we are also free to scan the delay T in order to perform $S_I(\tau, \omega_T, \omega_t)$ and $S_{III}(\tau, \omega_T, \omega_t)$ scans, referred to as rephasing zero-quantum and two-quantum scans, respectively. A rephasing zero-quantum scan still has the same pulse ordering as a rephasing one-quantum scan, except now the delay T is scanned while τ is held fixed. A photon echo is still emitted at a time τ after the arrival of the third pulse, however the

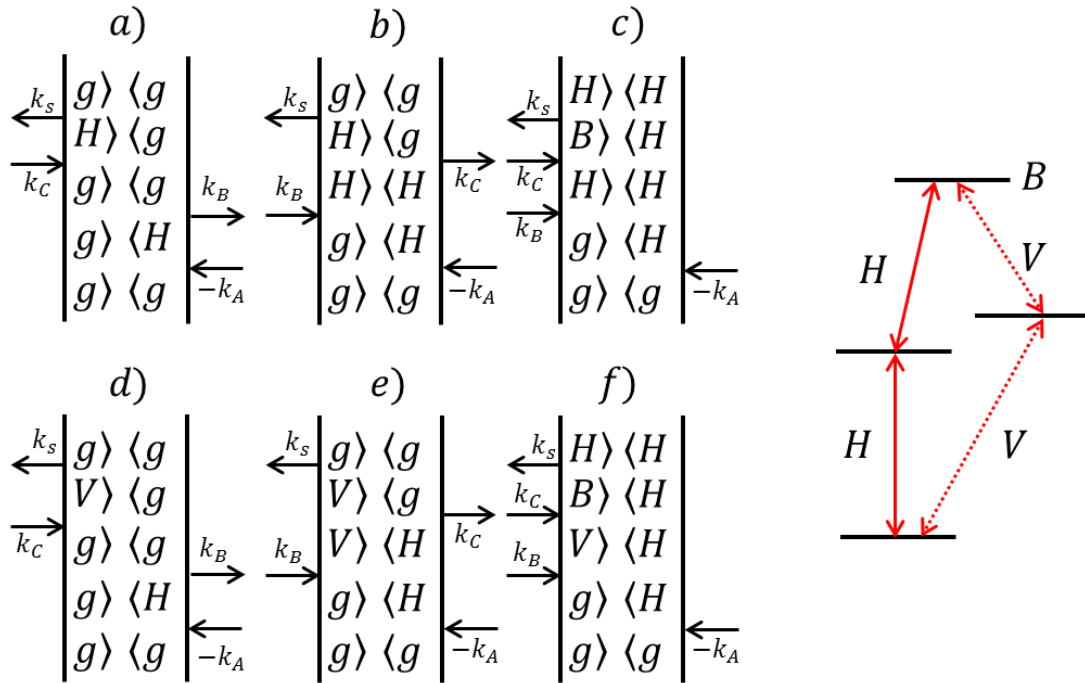


Figure 20: Feynman diagrams for a diamond level scheme.

population dynamics may now be probed. For a two-quantum scan, the conjugated pulse arrives last at the sample while the time delay T is scanned. This pulse ordering (for $\tau = 0$) is the same as a negative delay scan in a two pulse experiment for which no signal is expected for a simple two-level system. A signal for a negative delay scan would indicate the presence of many-body effects and therefore the two-quantum scan can provide a sensitive measurement of the many-body effects in a material.

3.9 INTERPRETING 2D SPECTRA

In order to gain an intuitive understanding of 2D spectra, let us consider three simple systems shown in Figure 19. In each of the three systems considered, individual resonances appear produce peaks along the diagonal and coupled resonances produce

peaks off of the diagonal. Let us first consider the system shown in Figure 19a where we have two independent transitions with energies $\hbar\omega_1$ and $\hbar\omega_2$ and the corresponding 2D rephasing spectra below. The spectrum shows two peaks along the diagonal, one ($\hbar\omega_t = \hbar\omega_1, \hbar\omega_\tau = -\hbar\omega_1$) and ($\hbar\omega_2, -\hbar\omega_2$). The $\hbar\omega_\tau$ axis is negative because in a rephasing scan the first pulse is conjugated and therefore picks up a negative sign. As expected for two independent transitions, no peaks are present off-diagonal. These peaks can be attributed to the Feynman diagrams (a) and (b) in Figure 20. If two transitions share a common ground state, such as the “V” system shown in Figure 19b, then the transitions can no longer be considered independent and are said to be coupled. When the two transitions are coupled, off-diagonal peaks can occur indicating that the material is being excited at one wavelength and emitting at another. These off-diagonal peaks can be attributed to diagrams (d) and (e) in Figure 20. Because these systems share a common ground state, excitation of one transition depletes the ground state population, which in turn affects the nonlinear optical response of the other transition.

The two independent two-level transitions and the “V” system shown in Figure 19 is a good illustration of the advantages of 2DCS. In linear absorption, PL or spectrally-resolved FWM, the off-diagonal peaks would be overlapped and hidden by the diagonal peaks. 2DCS is able to resolve whether or not these resonances are quantum mechanically coupled. By considering another system, shown in Figure 19c, we can understand some further advantages of 2DCS. In this system we have two independent two-level systems that are coupled through incoherent, non-radiative population transfer from the higher energy state to the lower energy state. This type of coupling would produce a single off-diagonal peak as shown in the Figure 19c. This peak originates from excitation at the higher energy $\hbar\omega_2$ and emission at the lower energy $\hbar\omega_1$. Because this

process involves population transfer it is an incoherent process, the dynamics of which can be mapped out by scanning the delay T .

3.10 LINESHAPE ANALYSIS

For the most part, we have only really looked at systems that have negligible inhomogeneous broadening. Most real-world systems, however, have some non-negligible inhomogeneous broadening that must be separated from the homogeneous linewidth in order to get an accurate measurement of either. A multitude of incoherent nonlinear optical measurements have been used to study the linewidth broadening mechanisms in semiconductors [149], but their effectiveness at measuring both the homogeneous and inhomogeneous linewidths are limited. For example, in TR-FWM the width of the photon echo can be correlated to the amount of inhomogeneity in the sample and the decay of the photon echo as the τ delay is scanned can provide one with a measure of the homogeneous linewidth, but the photon echo may not be well-resolved if many-body interactions are prevalent. Quantum beating between two slightly non-degenerate resonances may also distort the TR-FWM signal, which may mask the decay time of the photon echo [88, 150].

It should be no surprise at this point that 2DCS can overcome all of the difficulties in unambiguously separating the homogeneous and inhomogeneous linewidths. In fact, a quick glance at a 2D plot can give one a good sense of how much inhomogeneous and homogeneous broadening is present in a system since the width of a signal peak along the diagonal is correlated with inhomogeneous broadening and the width along the cross-diagonal is correlated with the homogeneous broadening. However getting detailed and accurate information is not so simple since the cross-diagonal and diagonal linewidths have been shown to be coupled [93, 95].

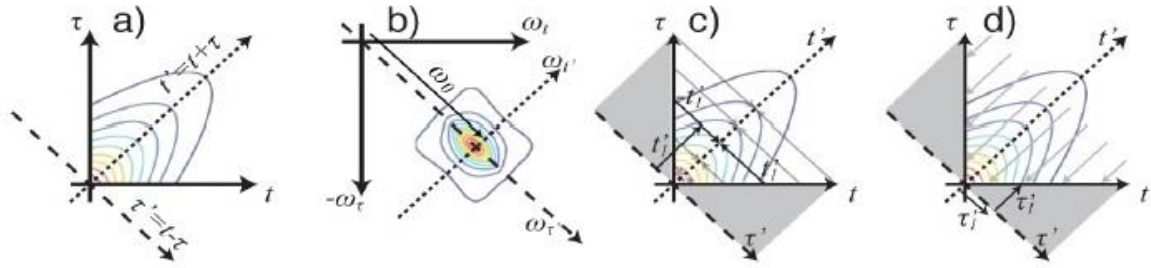


Figure 21: The 2D signal of a photon echo in the a) time domain and b) frequency domain. c) 2D time projection onto the diagonal corresponds to a slice along $\omega_{t'}$ in the frequency domain. d) 2D time projection onto the cross-diagonal corresponds to slices along $\omega_{\tau'}$ in the frequency domain [95].

Despite the coupling of the cross-diagonal and diagonal linewidths a quantitative connection can be made between the plotted linewidths and the homogeneous and inhomogeneous linewidths. Using analytical solutions to the optical Bloch equations (OBEs) one can decouple the two linewidths in a 2D rephasing scan [95]. These analytical solutions can then be Fourier-transformed into the time domain to get the signal in both time and frequency domains. Using the projection-slice theorem of Fourier transforms [151] one can then directly correlate slices line cuts in the time-domain signal with line cuts in the frequency domain signal. By projecting the signal in the time domain onto the axes t' and τ' , (see Figure 21) then Fourier transforming these projections into the frequency domain, one can then obtain a function for the lineshape of a slice in the frequency domain 2D plot. This procedure yields, for the rephasing amplitude spectrum, the following function for the cross-diagonal lineshape

$$S_I^{proj}(\omega_{t'}) = \frac{e^{\frac{(\gamma - \omega_{t'}^2)^2}{2\sigma^2}} \text{Erfc}\left(\frac{\gamma - i\omega_{t'}}{\sqrt{2}\sigma}\right)}{\sigma(\gamma - i\omega_{t'})}, \quad (70)$$

where Erfc is the complementary error function, γ is the homogeneous linewidth, and σ is the inhomogeneous linewidth. Similarly, the diagonal lineshape can be described by the following function

$$S_I^{proj}(\omega_{t'}) = \left(\sqrt{\frac{2}{\pi\sigma^2}} e^{-\frac{\omega_{t'}^2}{2\sigma^2}} \right) * \left(\frac{1}{\gamma^2 + \omega_{t'}^2} \right) = \frac{\sqrt{2\pi}}{\gamma} \text{Voigt}(\gamma, \sigma, \omega_{t'}), \quad (71)$$

where the Voigt function is a convolution of a Gaussian profile and a Lorentzian profile. Equations (70) and (71) are very general and apply for all values of γ and σ , but can take on more familiar forms when we assume certain limiting cases. For the case where there is no inhomogeneous broadening both the diagonal and cross-diagonal slices of the amplitude rephasing spectrum are Lorentzian functions

$$L(\omega, \gamma) = \sqrt{\frac{2}{\pi}} (\gamma^2 + \omega^2)^{-1}, \quad (72)$$

with a FWHM of 2γ . This limit leads to a spectral plot where the signal appears as a star shape with Lorentzians along both the diagonal and cross-diagonal directions.

In the opposite limit, the case where inhomogeneity dominates and we have $\sigma \gg \gamma$, the cross diagonal shape becomes $\sqrt{L(\omega_{t'}, \gamma)}$ with a FWHM of 2γ , and the diagonal lineshape becomes a Gaussian of the form

$$G(\omega_{t'}, \sigma) = \frac{1}{\sigma} e^{-\omega_{t'}^2/2\sigma^2}, \quad (73)$$

with a linewidth of σ .

Chapter 4: Experimental Apparatus

The work presented in this dissertation was taken solely with an apparatus called the JILA Multidimensional Optical Nonlinear SpecTRometer (MONSTR), designed at JILA in Boulder, Colorado by Bristow *et al* [94]. The MONSTR is an ultrastable platform of nested and folded Michelson interferometers that's designed to take a single pulsed laser input and produce four identical, phase stabilized pulses in a box geometry configuration. The delay between each pulse is varied with the use of translation stages with three of the pulses being used for excitation and the fourth pulse employed as a phase stable reference pulse copropagating with the signal itself. The interference between the reference pulse and the signal is what is read out on the spectrometer and processed in order to generate a 2D spectrum. Because 2D coherent spectroscopy requires phase sensitivity, great care is taken in maintaining phase stability between the pulses with the use of active stabilization via feedback assisted, interferometric monitoring and locking between steps and during data acquisition [148]. The interferometric techniques employed in the MONSTR gives us phase stability between pulses of $\lambda/150$ and up to $\lambda/400$ for laser pulses centered at 800 nm, which is critical in obtaining a high quality 2D signal. Mechanical vibrations, drift in the optical components or incorrect measurements of the pulse delays can degrade the quality of the signal or introduce artifacts making interpretation of the 2D data difficult or impossible. Because of the requirement of phase stability, the implementation of 2DCS in the near-IR and optical regimes is a challenging endeavor.

4.1 THE JILA-MONSTR

Previous implementations of 2DFTS have used various passive stabilization techniques in order to maintain phase stability between the pulses. These techniques

range from the simple use of sturdy mirror mounts [111, 152] to more complicated implementations that use diffractive optics [153, 154] and pulse shapers [155, 156]. For experiments in which the operating wavelengths are very long compared to the near-IR or the visible spectrum, it is often quite sufficient to stabilize the various pulses with sturdy mirror mounts alone. For wavelengths in which the inherent mechanical vibrations in the setup are on the order, or greater than, the wavelength of the excitation pulses, then passive stabilization must be improved. In these cases, diffractive optics can be used in order to pick out the first-order diffraction of the excitation pulses. The first-order diffraction is then directly sent to the sample and thus the time-delayed beams have a common optic as their source and are inherently phase stable.

Pulse shaping techniques also make use of a common optic to generate inherent phase stable pulses. This technique can be employed with the use of an acousto-optic modulator (AOM). An AOM can be used to generate a train of collinear pulses in which one can control the pulse delays, phase and waveform shape. In the collinear geometry, phase-cycling techniques can be used to isolate the desired nonlinear signal of interest.

The drawback of such passive stabilization techniques is often the limitation on pulse delays, which is the case for both diffractive optics and pulse shaper based stabilization. This limitation is especially problematic when dealing with the slow population relaxation times often found in semiconductors. Problematic still, with both techniques, is the potential effects of the local oscillator, or reference beam, as it passes through the sample. In systems which have strong excitation dependent phenomenon, the modifying effects of the reference beam as it passes through the sample cannot be ignored.

The design of the MONSTR is aimed at overcoming the limitations of short pulse delays and local oscillator effects with the use of active phase stabilization, through

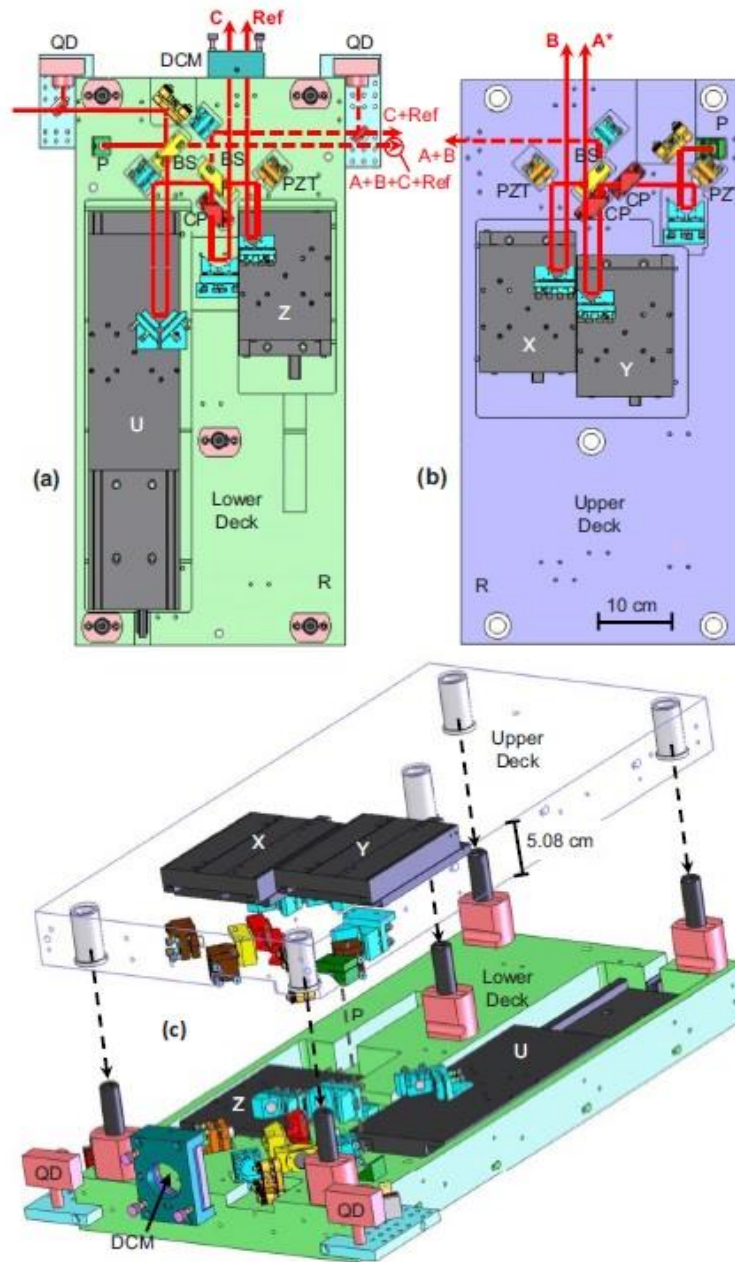


Figure 22: a) Drawing of the lower and b) upper decks of the MONSTR. c) Schematic of how both decks fit together. (DCM=Dichroic Mirror, QD=Quad-diode, BS=Beamsplitter, PZT=Piezo mounted mirror, CP=Compensation Plate, P=Periscope mirror). The Ti:sapph and HeNe enter the lower deck on the left. The Ti:sapph exits through the DCM and the HeNe exits through the sides of the deck.

feedback electronics, and translation stages in order to achieve pulse delays of hundreds of picoseconds. The MONSTR consists of a top deck and bottom deck each housing two delay stages that make up a Michelson interferometer (Figure 22). The top deck houses the translation stages and optics responsible for producing beams A and B as well as their time delays with stage X and Y controlling the time delays of beams B and A , respectively. The bottom deck houses the translation stages and optics for beam C and the *Tracer/Reference*, with stage Z used to adjust the delay of the *Tracer* and stage U used to adjust the relative delay between the top and bottom deck. The top deck and bottom deck are assembled and aligned separately and the two decks are then put together to be aligned with respect to each other. The Ti:Sapph and HeNe (Melles Griot 25-LHP-073) are aligned to overlap with each other before entering the MONSTR and a dichroic mirror is placed just before the beams exit in order to reflect the HeNe back through the MONSTR. The back-reflected HeNe beams exit the MONSTR through the side and represent interference from the $C+Ref$, $A+B$, and $A+B+C+Ref$ arms of the interferometers. These three interference patterns are sent to detectors and are monitored with the feedback electronics. Any change in relative delay between any of the beams A , B , C or *Tracer*, due to drift of the optics inside the MONSTR, shows up as a shift in the interference pattern being monitored at the HeNe diagnostic detectors which can then be compensated for using the homemade feedback electronics and piezo actuated mirrors (PZT) which were purchased from *Piezomechanik GMBH* (model HPCH150/6-2/2).

Stages X , Y , and Z are all identical and were purchased from Aerotech. Each have a travel of 5 cm (ALS130H-0050) while stage U has a travel range of 20 cm (ALS135-200) and was also purchased from Aerotech. The beamsplitters (BS) used were purchased from CVI (FABS-790-45S-PW-1004-UV) and designed around 790 nm for broadband femtosecond pulses at 50/50 transmission and reflection. The compensator plates (CP)

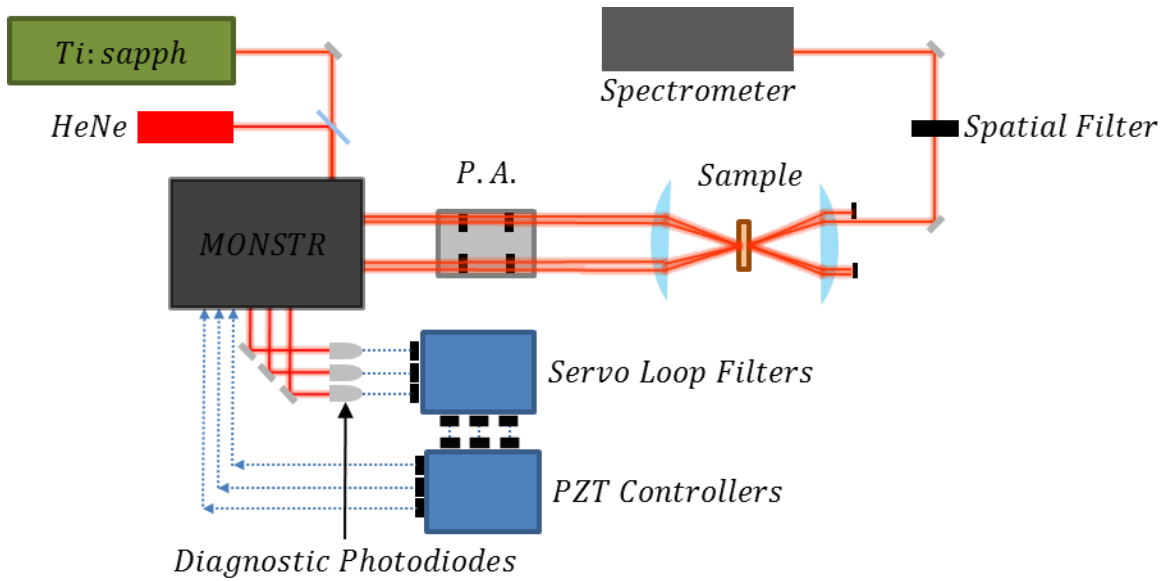


Figure 23: Schematic of the experiment outside of the MONSTR. The *reference/tracer* and signal copropagate with each other after the sample and no external reference is needed. (P.A.=Polarization Assembly)

were also purchased from CVI (W2-PW-1004-UV-500-850-45S) and were designed for femtosecond pulses and maximal transmission. The compensator plates are there specifically to ensure that all beams pass through similar amounts of glass and therefore are identical when they exit the MONSTR. The quad-diode photodetectors (QD) are there to ensure reliable alignment day-to-day through the MONSTR, but in principal, pinholes before the MONSTR, for both the HeNe and Ti:Sapph, were found to be sufficient. The laser source used is a *Spectra-Physics Tsunami* (Model 3960-X1BB), diode-pumped (Millennia Pro-10sJ), Ti:Sapphire operating at 80 MHz repetition rate. The wavelength can be tuned between 700 nm – 1000 nm with pulse durations as short as 100 fs in duration. Before entering the MONSTR, the Ti:Sapph is precompensated for dispersion with the use of a prism pair (CVI IB-13.0-60.6-SF10) and chirped mirrors (Layertec 102267), giving us a pulse duration of 130 fs at the sample.

Once outside the MONSTR, the four beams exit in a square pattern that's 1"x1" and through a polarization optics assembly (see Figure 23) that was custom made to house two liquid crystal phase modulators, four half-wave plates (Special Optics 8-9014-1/2-700-1550 nm), four polarizers (Newport PolarCor 74-860 nm 05P109AR.16) and four quarter-wave plates (Special Optics 8-9012-1/4-600-900 nm). The polarization assembly gives us the freedom to work with any combination of linear or circular polarization necessary for the sample in question. The liquid crystal phase modulators (Meadowlark Optics Liquid Crystal Variable Retarders) are required for phase-cycling (see Chapter 3) and allow us to toggle the phase of both beams A and B , between 0 and π . After the polarization assembly, the beams pass through a 2-inch diameter achromatic lens and then an AR-coated window purchased from CVI (W1-PW1-2025-UV-800-0). The AR-coated window serves the purpose of partially reflecting the four beams backwards onto a camera purchased from the *Imaging Source* (DMK 21BF04). This camera is then used to monitor a replica of the focus which is then used to determine the zero delay for all pulses. The autocorrelation is done in a pairwise fashion, first the top deck beams, then the bottom deck beams and then one beam from each deck. The intensity of an interference fringe is monitored as a function of the delay of one beam relative to another. As the beams pass through their zero delay, the interference fringe decays and what is seen are interference fringes modulated by a double Gaussian as a function of stage position. This plot is then fitted in order to determine the zero position for delay.

After the polarization assembly, one has the option of using a *Reference* beam that has been routed around and recombined with the signal after the sample. In addition, since the *Reference* is only partially reflected and routed around, one has the option of using as the *Reference* the beam that passes through the sample itself. In many

experiments it is possible to send all four beams to the sample, the three excitation beams *A*, *B*, and *C*, as well as the *Tracer*. This has the advantage that the *Tracer* is already phase stabilized with respect to the three excitation beams, but has the disadvantage of creating potential unwanted modifications to the sample dynamics, especially for samples that are particularly sensitive to excitation induced effects. The simplest and most direct way around this is to route the *Tracer* around the sample and recombine it with the *Signal* downstream of the sample. Because this involves introducing optics not common to both the *Signal* and *Tracer*, another PZT and diagnostic detector must be used to monitor and compensate for changes in the path length between the *Reference* and the *Signal*. This is simply done by inserting a beamsplitter and combining the *Reference* with any one of the excitation beams. A translation stage is used for the routed *Reference* beam path in order to ensure that both the beams at the diagnostic detector overlap in time. Our experimental design could accommodate the routing of the *Reference* around the sample, but for the data shown in this dissertation, the excitation induced effects of our sample were unaffected by the presence of the *Reference* and so we chose not to use the external diagnostic detector and PZT. This simplified our day-to-day alignment considerably. After the *Reference* is recombined with the *Signal*, it is sent through a 10 μm spatial filter (Newport 910PH-10) and then to the spectrometer (Acton SpectraPro 2750) where spectral interferometry is used to extract the phase and amplitude of the generated four-wave mixing (FWM) signal for each time delay τ or T . The spatial filter was of utmost importance when working with monolayer thick samples on transparent sapphire substrates. Without the spatial filter, the scattering of the excitation beams into the signal direction, even with modest excitation powers, would easily saturate our CCD.

The sample itself is housed in a cold-finger cryostat purchased from CryoIndustries (CFM-1738-102-XE). Once the daily alignment procedures are done, i.e.

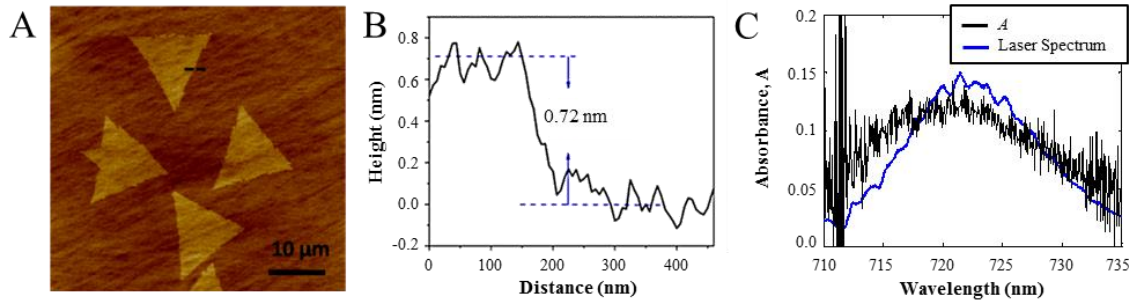


Figure 24: a) Atomic force microscopy image of monolayer WSe₂ flakes on a sapphire substrate. b) Height profile along the dashed line in a). Absorbance determined from differential reflectance measurements at 17 K using the laser spectrum, yielding a maximum $A = 0.12$ at the peak of laser. The laser spectrum is shown in blue as a reference.

making sure that we have a perfect square pattern for our beams, making sure the beams overlap at the replica focus and on the sample, and aligning the *Tracer/Reference* through the spatial filter, then we have the freedom to optimize any signal by moving the entire cryostat through, or parallel, to the focus of the three excitation beams.

4.2 SAMPLE PREPARATION, PHOTOLUMINESCENCE AND SAMPLE IMAGING

The samples used in this dissertation were prepared using chemical vapor deposition (CVD) onto transparent sapphire (0001) substrates from *Tera Xtal Technology Corporation* [39]. The substrate was cleaned with an H₂SO₄/H₂O₂ (70:30) solution at 100 °C for one hour in preparation for deposition. The sample was then placed in a quartz holder in the center of a 1-inch tubular furnace in which a mixture of Ar/H₂ gas (Ar = 80 sccm and H₂ = 20 sccm at a pressure of 1 Torr) flows through in order to bring the WO₃ and Se vapors to the substrates. Upstream of the blank substrates, WO₃ powder (0.3 grams, 99.5% *Sigma-Aldrich*) and Se powder (99.5% *Sigma-Aldrich*) were placed in ceramic holders with WO₃ being placed in the heating zone center and the Se powder placed farther upstream still. The Se powder was maintained at 270 °C and the WO₃

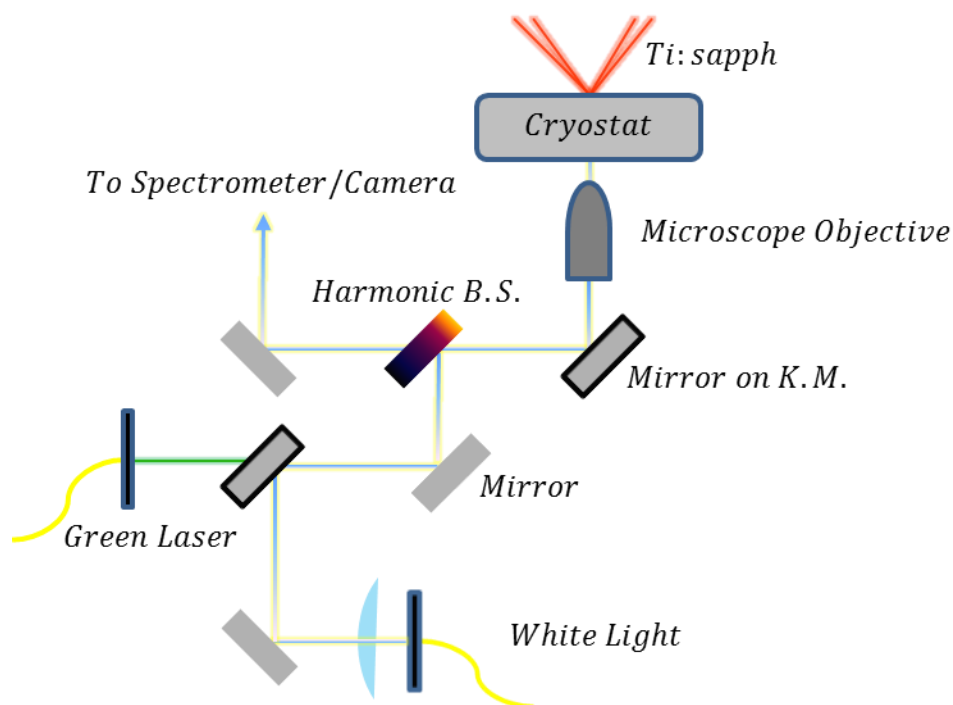


Figure 25: Schematic of the imaging and PL optics. The mirrors on the kinematic mounts (K.M.) may be removed in order to switch between PL and imaging. The microscope objective was also mounted on a kinematic mount in order to let the Ti:sapph through for 2D measurements. Both the white light and green laser sources were brought in via fiber optic cables and placed on fiber mounts. The harmonic beamsplitter (B.S.) is able to reflect most of the green light and pass most of the white light.

powder was heated to 925 °C at a rate of 25 °C/min. For a temperature of 925 °C at the heating zone center, the sapphire substrate itself reached temperatures of 750 to 850 °C. After reaching 925 °C, the heating zone was maintained at that temperature for 15 minutes and then allowed to cool naturally back to room temperature.

Figure 24 shows an optical microscope image of the WSe₂ sample produced with this method. The figure shows monolayer WSe₂ domains of triangular shape and ~10 μm

lateral size. The figure also shows the height profile of the flakes measured with atomic force microscopy, confirming the expected thickness of ~ 7 Å for monolayer WSe₂.

In practice, for samples that have a very strong nonlinear signal, using the setup described in Figure 23 to find a decent 2D signal was more than sufficient, i.e., no further modifications to the setup were necessary. Using the daily alignment procedures for the MONSTR would often get us close enough where we could see a 2D signal that we could then optimize by adjusting the sample position. This was the case for the first sample we worked, 10 period GaAs quantum well, which was primarily used to diagnose any problems in the MONSTR and optimize the daily alignment procedures. After working out the bugs using the quantum well sample, we then moved onto the TMDC sample and found that we could no longer find a signal and so we needed to modify the original MONSTR experimental apparatus in order to perform more diagnostics before searching for a 2D signal.

Unlike the GaAs quantum well, the first TMDC samples we worked with were not uniform and so we found it necessary to add modifications to the MONSTR setup in order to image and perform photoluminescence with the sample still in the cryostat. Because TMDC samples are very sensitive to thermal cycling and humidity, it was not possible to take the sample out of the cryostat and perform the PL in another setup. In addition, we needed the ability to find areas of the sample that yielded the strongest PL and then quickly switch optics in order to perform 2D on the same spot on the sample. Figure 25 shows a schematic of PL and imaging optics that could easily be switched out, or put in, in order to quickly go between PL, sample imaging and 2D measurements. The imaging and PL are done with the white light source and 532 nm laser incident from the opposite direction as the Ti:Sapph. We use a 10× objective (Newport M-10×) for both imaging and PL and the harmonic beam splitter (Thorlabs HBSY12) serves to reflect 532

nm light but transmits 700-800 nm light. Many of the mounts are kinematic and can be inserted or removed with ease. After aligning the MONSTR, we then image the sample looking for flakes of TMDC large enough to accommodate as much of our 30 μm beam as possible. After finding a suitable flake we would then perform PL on it and then move on to 2D scans if the flake showed a strong PL signal. The setup in Figure 25 allowed for us to image the PL laser and the Ti:Sapph laser on the sample, as well as whether or not we were on a monolayer flake.

4.3 FOURIER TRANSFORM SPECTRAL INTERFEROMETRY

Because of the weak four-wave mixing signal and strong scattering from the TMDC samples, processing the data carefully was crucial in detecting a signal. Two methods for extracting the FWM were indispensable: phase cycling and filtering through Fourier transform of the signal into the time domain.

The FWM signal, in practice, is first phase-cycled and then saved to be Fourier transformed later using Matlab. For the sake of clarity, it is easier to start with an explanation of filtering with Fourier transformation into the time-domain. This technique is done with the use of spectral interferometry [157, 158] and a phase-stabilized reference pulse. In our experiment we send both the co-propagating reference and signal into the spectrometer with the reference arriving first. We typically set the delay between reference and signal between 1 and 3 picoseconds. The longer the delay the more interference fringes that appear on the CCD and with too long of a delay you run into problems of resolving the fringes. The CCD we use is an *Andor iDus* (DU416A-LDC-DD) with a 2000×256 pixel array, which can be thermo-electrically cooled to $-80\text{ }^\circ\text{C}$.

The interferogram can be written as [158]

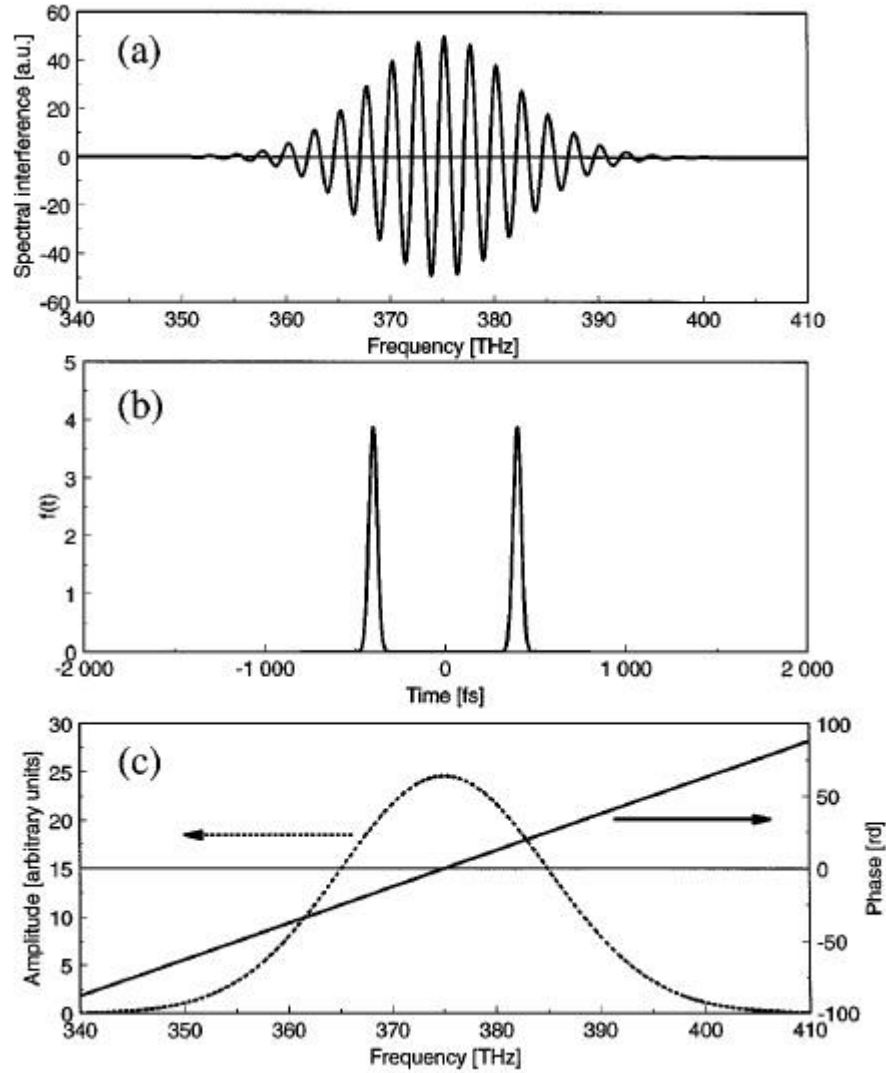


Figure 26: a) Pure interference term after subtracting reference and signal power spectra from equation (74). b) Inverse Fourier transform of the interference term and after applying causality condition we Fourier transform in order to get c) which is the spectral phase and amplitude [158].

$$|E_R(\omega_t) + E_S(\omega_t)|^2 = |E_R(\omega_t)|^2 + |E_S(\omega_t)|^2 + 2\text{Re}\{E_S(\omega_t)E_R^*(\omega_t)\}, \quad (74)$$

where $E_R(\omega_t)$ and $E_S(\omega_t)$ are the electric fields for the reference and signal, respectively.

The first two terms in equation (74) are actually taken before data acquisition is started

and then subtracted from the reference/signal interferogram. After subtraction, we take the inverse Fourier transform of the pure interference term, the third term on the right in equation (74), with the result shown in Figure 26]. The inverse Fourier transform contains two terms separated by a time $2\Delta_t$

$$S(t) = \mathcal{F}^{-1}\{S(\omega_t)\} = f(-t - \Delta_t) + f(t - \Delta_t), \quad (75)$$

which show up as two peaks on either side of $t = 0$. The only term that satisfies the causality conditions is $f(t - \Delta_t)$ and everything else is taken to be noise and set to zero using a Heaviside theta function $\Theta(t - \Delta_t)$. Equation (75) is then Fourier transformed back into the frequency domain, multiplied by a phase factor $\exp(-i\omega_t\Delta_t)$ to remove the linear phase associated with the reference/signal delay and divided by the reference amplitude. What is left is the complex FWM signal electric field

$$E_S(\omega_t) = \frac{\mathcal{F}\{\Theta(t - \Delta_t)\mathcal{F}^{-1}\{S(\omega_t)\}\}e^{-i\omega_t\Delta_t}}{E_R^*(\omega_t)}. \quad (76)$$

The extracted FWM signal amplitude and phase are shown in Figure 26. The signal phase increases by π radians across the resonance, as expected, and is measured with respect to the reference phase. In our experiments we only use the amplitude data and so the phase is of little concern for this dissertation.

4.4 PHASE CYCLING

For the TMDC samples we worked with, we found that filtering in the time-domain was not enough to extract a decent signal. Scattering and background noise that occurred at the same time delay, Δ_t , was more than enough to hide any sort of signal. Also, because laser scatter occurs along the diagonal in the 2D spectrum, any small signal that happens to be along the diagonal will be indistinguishable from laser scatter. The

noise from laser scatter can be drastically reduced by using phase cycling techniques that were first developed in NMR spectroscopy [93]. This technique has been previously used in 2D spectroscopy in experiments, where the pulses are collinear, in order to isolate the nonlinear terms of interest. Many of these experiments used acousto-optic based pulse shapers in order to induce phase shifts [114, 156], but we take a different approach and use liquid crystal phase modulators to toggle the phase of beams A and B between 0 and π . The liquid crystals were purchased from Meadowlark Optics and were designed to be operated between 450 nm and 1800 nm. The liquid crystals are operated by applying a voltage to them, this voltage is slowly ramped up from 0 V to 5 V while a camera at the replica focus monitors the interference fringes between pulses A and B . The liquid crystals are then calibrated to operate at 0 V and whatever voltage was found to give a π phase shift. In practice, the voltage for π phase shift changes slightly every day and the liquid crystal calibration must be done before each day of data acquisition. For a rephasing one-quantum experiment (see Chapter 3) in which pulse A comes first, then pulse B and finally pulse C , at each delay step as we scan pulse A to earlier and earlier times we toggle the phase of both beams A and B . To see how this eliminates laser scatter let us consider an interferogram that includes the reference, FWM as well as, for simplicity, scatter from pulse A alone. The interferogram is then given by

$$\begin{aligned}
s_1 &\equiv |E_R(\omega_t) + E_S(\omega_t) + E_A(\omega_t)|^2 & (77) \\
&= |E_R(\omega_t)|^2 + |E_S(\omega_t)|^2 + |E_A(\omega_t)|^2 \\
&\quad + 2\text{Re}\{E_S(\omega_t)E_R^*(\omega_t) + E_S(\omega_t)E_A^*(\omega_t) \\
&\quad + E_A(\omega_t)E_R^*(\omega_t)\} ,
\end{aligned}$$

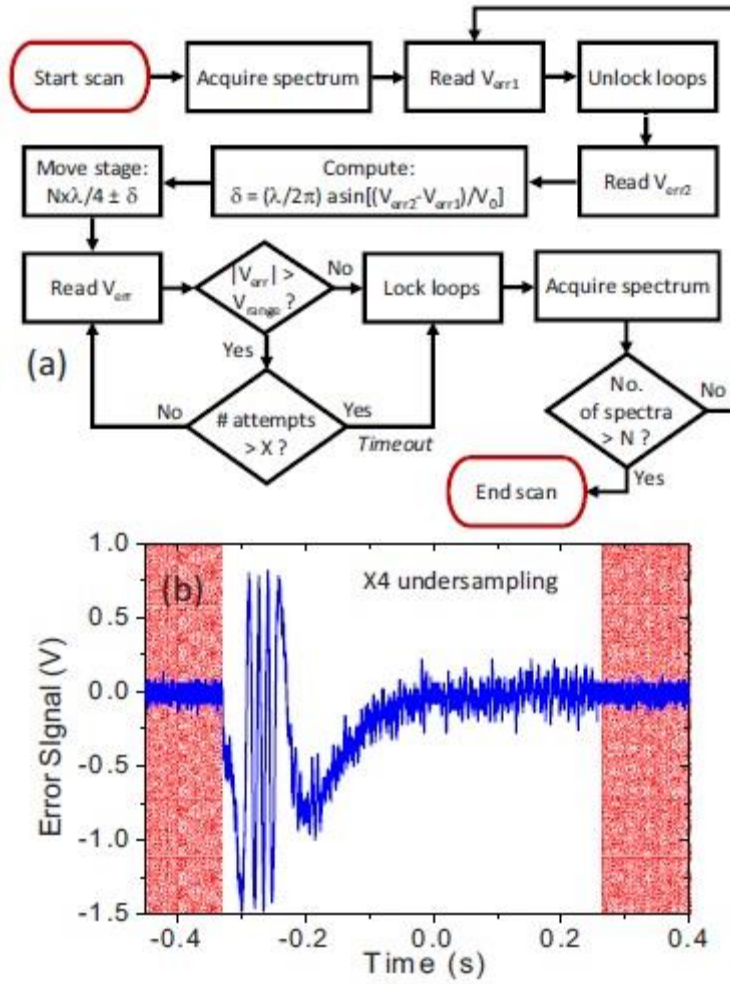


Figure 27: a) A flowchart of the stepping procedure and b) the HeNe error signal for when the delay is stepped by a distance $\lambda=532$ nm. The red shaded regions indicate when the stages are locked and the feedback loop has been engaged.

where the phase offsets between A , reference and signal are defined to be zero. The phase of the signal itself is dependent on the phase associated with the nonlinear response, $\varphi_{S,0}(\omega_t)$, as well as the phase of the excitation pulses themselves. We can write this as

$$\varphi_S(\omega_t) = \varphi_A(\omega_t) + \varphi_B(\omega_t) + \varphi_C(\omega_t) + \varphi_{S,0}(\omega_t). \quad (78)$$

By toggling the phase of just pulse A, it introduces a factor of $e^{\pm i\pi} = -1$ to all the complex terms with $E_S(\omega_t)$ or $E_A(\omega_t)$ in them. For each delay, we can then toggle the phase of both beams A and B and arrive at four different spectra: zero phase shift for both beams (s_1), π phase shift for beam A (s_2), π phase shift for beam B (s_3), and π phase shift for both beams A and B (s_4). In terms of how the complex portion of equation (77) changes with each type of phase shift, we have

$$\begin{aligned}
s_2 &= 2Re\{-E_S(\omega_t)E_R^*(\omega_t) + E_S(\omega_t)E_A^*(\omega_t) - E_A(\omega_t)E_R^*(\omega_t)\} \\
s_3 &= 2Re\{-E_S(\omega_t)E_R^*(\omega_t) - E_S(\omega_t)E_A^*(\omega_t) + E_A(\omega_t)E_R^*(\omega_t)\} \\
s_4 &= 2Re\{E_S(\omega_t)E_R^*(\omega_t) - E_S(\omega_t)E_A^*(\omega_t) - E_A(\omega_t)E_R^*(\omega_t)\} .
\end{aligned} \tag{79}$$

By combining the four interferograms

$$s_{net} = \frac{1}{4}(s_1 + s_2 - s_3 - s_4) = 2Re\{E_S(\omega_t)E_R^*(\omega_t)\} , \tag{80}$$

we can retrieve the FWM/interference term and eliminate any scatter from beam A , but also from the other two pump beams as well. Because the liquid crystal response time is so fast (20 ms), the phase cycling does not add any significant amount of time to the data collection. The limiting factor in the data collection time is the result of the motion of the mechanical stages. By using phase cycling, we also eliminate the need to take the FWM power spectrum at each delay, which was a necessary step in order to properly implement Fourier transform spectral interferometry (see section 4.3). This allows us to effectively cut the acquisition time down by a factor of two.

4.5 ACQUIRING 2D DATA

In order to generate a 2D array we perform phase cycling on the interferogram at each delay and carefully monitor the stepping in between each phase cycle in order to

ensure correct tracking of the signal phase. A flowchart for the stepping procedure is shown in Figure 27. Consider a one-quantum rephasing scan in which we scan the time delay τ , i.e. we scan the stage for beam A in the upper deck. At the beginning of the scan we acquire a phase-cycled interferogram, after which we prepare to unlock the feedback loop by measuring the HeNe diagnostic error signal associated with the upper deck interferometer (V_{err1}). Next, the interdeck feedback loop is disengaged followed by the upper deck servo loop. The upper deck error signal is remeasured (V_{err2}) in order to measure the change in the path length when a voltage is applied to the piezo and when the loop is disengaged and no voltage is being applied. The change in the path length difference is calculated using $\delta = (\lambda/2\pi)\arcsin(V_{err1} - V_{err2}/V_0)$, where λ is the HeNe wavelength and V_0 is the interferometer signal's peak-to-peak amplitude, which is always set to 2 V for all interferometers. The stage is then stepped in integer increments of the HeNe wavelength divided by four in order to allow the feedback loops to relock to zero volts on the upper deck error signal. Each step is then corrected for the path length change, due to unlocking of the piezo, with a factor of $\pm\delta$. The stage is then moved and the HeNe error signal (V_{err}) is re-measured in order to ensure that the stage did indeed move in integer steps of the HeNe wavelength $\lambda/4$. After this, the upper deck feedback loop is re-engaged followed by the interdeck feedback loop then a phase-cycled spectrum is taken and the whole process is repeated.

In most one-quantum rephasing scans we set our step size to 8 HeNe fringes and sometimes more. Since each fringe is equal to a distance $\lambda/4$ of the stage motion, 8 HeNe fringes corresponds to a delay of $2.5 \mu m$, or $8.6 fs$. The Nyquist frequency associated with this delay is $f_{Nyq} = 1/2\Delta\tau = 59.2 THz$, which is the maximum frequency that can be reconstructed without aliasing effects. This is just another way of saying that in a Michelson interferometer, the step size of your stage is the limiting factor in how high a

frequency range you can scan. In the TMDC samples we studied, the signal for the A exciton occurs at around 730 nm, or 410 THz. This means, for a step size of 8 HeNe fringes, our data is very much undersampled. One way around this is to set the step size to just one HeNe fringe which corresponds to a Nyquist frequency of 473.61 THz, but this means our acquisition time for each scan would effectively be a factor of 8 longer, which is generally prohibitively long. In practice, the undersampled and aliased signal is taken with step sizes of 8-32 HeNe fringes and anti-aliasing filtering is done to shift the measured frequency into the expected frequency range.

The total number of steps taken for a scan is determined by the undersampling ratio (i.e. how many HeNe fringes) and the signal decay rate. Scans are taken as to allow the signal to completely decay below the detection threshold and a windowing function is applied in the time domain in order to make the signal decay gradually to zero. If not for the windowing function, the signal would be abruptly truncated leading to unwanted oscillations in the frequency domain.

Chapter 5: 2DCS on Monolayer TMDCs

There are many two-dimensional materials that exist in nature that can be mechanically exfoliated from their bulk forms into monolayer sheets, graphene being the most notable example. Transition metal dichalcogenides (TMDCs), like graphene, consist of stacks of atomically thin sheets with weak, out-of-plane Van der Waals forces holding the layers together and strong in-plane bonding. The surge in graphene research catapulted forward our knowledge in sample preparation, optical detection, transfer and manipulation and advanced the physical understanding of 2D materials. Since then, there has been much renewed interest in applying this new knowledge to the study of TMDCs. TMDCs represent an exciting new class of direct gap materials with coupled spin and valley pseudospin degrees of freedom [16, 20]. Many novel phenomenon have already been discovered in these materials including a non-hydrogenic exciton Rydberg series [159, 160], electronic and valley coherent coupling [63, 161], and carrier spin and valley pseudospin Hall effects [108, 162].

Monolayer TMDCs differ from graphene in that they have a bandgap, with most materials in this class having transitions between 1-2 eV [163] (e.g. monolayer WSe₂ has an exciton transition at 1.7 eV) showing promising applications in new FET and optoelectronic devices. TMDCs also exhibit layer-dependent properties. Many of the semiconducting TMDCs exhibit transitions from an indirect gap, in their bulk forms, to a direct gap in their monolayer limits [20, 164]. This transition leads to dramatically increased photoluminescence in the monolayer limit which opens even further possibilities for optoelectronic applications. The electronic structure of many monolayer TMDCs also allows for valley polarization which has promising applications in new and novel technologies including valleytronic devices [63, 76, 84]. In addition, large

excitonic effects are expected in many TMDCs, a property which may be exploited for optical and electrical control of excitons in any potential application of atomically thin optoelectronics and valleytronic devices [7].

5.1 MOTIVATIONS

Because TMDCs represent such a new class of materials with many unique properties, it is of utmost importance to characterize the fundamental properties of the materials. The two key parameters that characterize the quantum dynamics of excitons is the population relaxation (decay) time, T_1 , and the dephasing time T_2 (see Chapter 4). The population relaxation is the inverse of the decay rate Γ and the dephasing time is inversely proportional to the homogeneous linewidth $\gamma = \hbar/T_2$. In terms of a simple two-level system, Γ represents the population decay, both radiative and non-radiative, from the excited state to the ground state, while γ represents the dephasing rate of a coherent superposition between the ground state and the excited state. The decay rate and dephasing rate are not independent of each other and can be shown to obey the relation

$$\gamma = \frac{\Gamma}{2} + \gamma^* , \quad (81)$$

where γ^* represents elastic, pure dephasing processes, e.g. exciton-impurity scattering. Pure dephasing processes do not include any processes related to population transfer. From equation (81) we can see that the linewidth of the exciton resonance will be broadened by population relaxation and pure dephasing process and it is with a measurement of the homogeneous linewidth that we may begin to understand some of the fundamental processes going on inside a material. In real materials though, the homogeneous linewidth can be hidden by inhomogeneous broadening which can arise from differences in local potentials due to impurities, disorder or--as is the case in GaAs

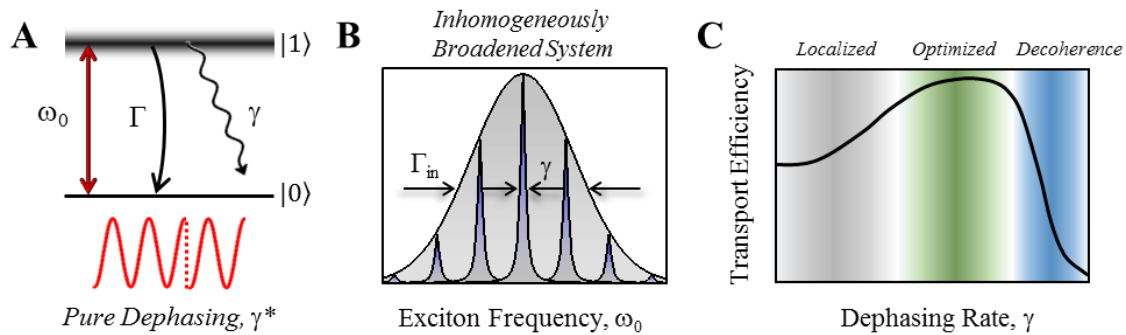


Figure 28: a) The quantum dynamics of a resonance at frequency ω_0 is characterized by two parameters: the population relaxation rate, Γ , and the dephasing rate, γ . b) Inhomogeneous broadening hides the intrinsic homogeneous linewidth. c) Balancing the dephasing rate in many systems can lead to optimized energy transfer between resonances.

quantum wells--fluctuations in well widths. This broadening is an important characteristic to measure in itself as it is indicative of the quality of the sample.

The key parameter we have set out to measure is the intrinsic exciton homogeneous linewidth, knowledge of which can shed light on the dissipative effects that interactions with the bath have on the system of excitons. The dephasing time is of utmost importance for any potential application where coherent control of the exciton dynamics is required since it sets the upper limit on the time scales where coherent control can be maintained. The ability to measure both the inhomogeneous and homogeneous linewidths is also crucial as the dynamic interplay between both types of broadening can play an important role in energy transfer behavior. The interplay between homogeneous and inhomogeneous broadening has already been shown to factor significantly into the gain dynamics of semiconductor lasers [165] and the energy transfer processes in photosynthesis [166]. As one can imagine intuitively, systems with very

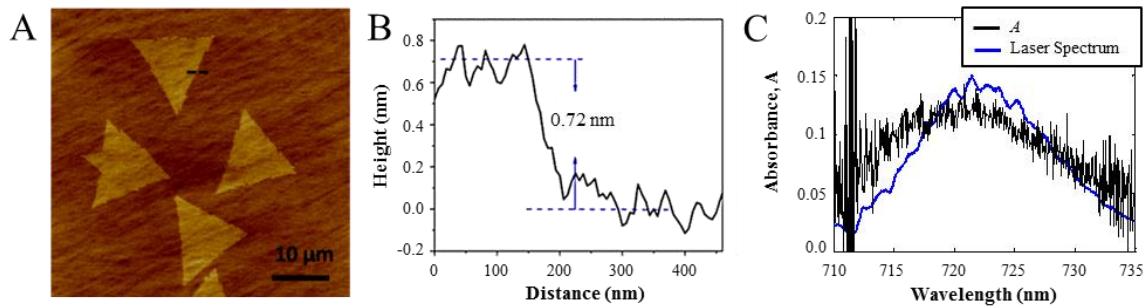


Figure 29: a) Atomic force microscopy image of monolayer WSe₂ flakes on a sapphire substrate. b) Height profile along the dashed line in a). Absorbance determined from differential reflectance measurements at 17 K using the laser spectrum, yielding a maximum $A = 0.12$ at the peak of laser. The laser spectrum is shown in blue as a reference.

narrow homogeneous linewidths exhibit little overlap between resonances that are separated due to inhomogeneity (see Figure 28). On the other hand, strong dephasing will naturally lead to decoherence before any significant energy transfer can take place. It is therefore critical in designing systems with the most efficient energy transfer to be able to measure the homogeneous and inhomogeneous linewidths [167].

In order to measure the homogeneous linewidth of the system we performed 2D rephasing scans on monolayer WSe₂ triangular flakes with a base width of approximately 10 μm. The WSe₂ flakes were deposited on double-sided polished sapphire using chemical vapor deposition (CVD). This sample was then mounted inside a cold-finger cryostat at the focus of three pulsed excitation beams from a Ti:Sapphire laser. These three beams were phase-stabilized with respect to each other and separated by time delays τ_1 and τ_2 , with the photon echo arriving at time τ_3 after the last pulse.

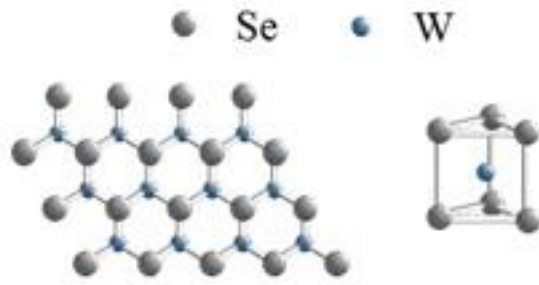


Figure 30: 2D hexagonal crystal lattice consisting of two planes of Se atoms separated by a plane of W atoms.

5.2 PHOTOLUMINESCENCE STUDIES

The thickness of the flakes and their lateral widths were both confirmed with atomic force microscopy (AFM), the results of which can be seen in Figure 29. Monolayer WSe₂ is composed of two layers of selenium atoms separated by a layer of tungsten atoms that form a 6-7 Å thick hexagonal lattice (see Figure 30). In monolayer transition metal dichalcogenides, the minimum in the momentum-energy dispersion does not occur at the Γ point as in GaAs, but at the $\pm K$ points of the first Brillouin zone (see Figure 31). The bandgaps at the $\pm K$ points are degenerate, direct bandgaps and well-separated in momentum space. The optical selection rules for the $\pm K$ excitons in monolayer TMDs can be exploited to give one optical control of carrier spin and valley pseudospin degrees of freedom [63, 84]. The work presented in this dissertation focuses on the lowest energy transitions at the $\pm K$ points, the so-called A exciton of one particular helicity.

Figure 32 shows the photoluminescence (PL) of an ensemble of WSe₂ flake taken at 10 K with an excitation laser with wavelength 532 nm. The peak at 730 nm is what we identify as the A exciton, labeled X in the figure. The other peak (D^0X) arises from

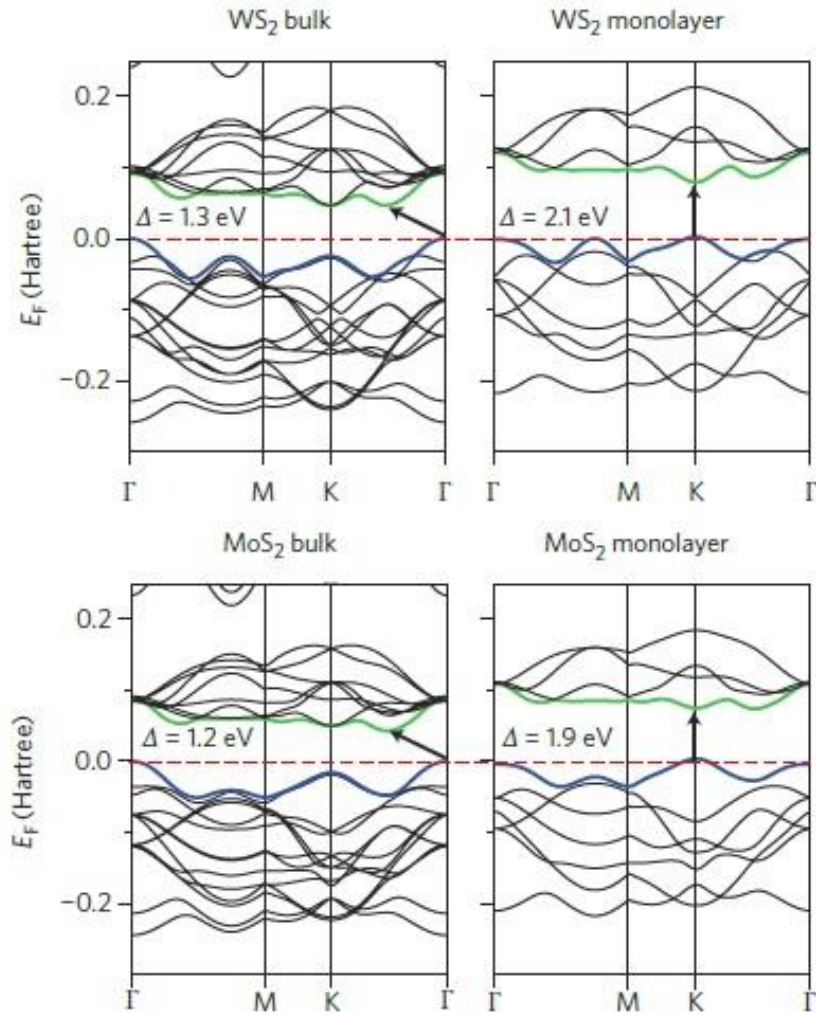


Figure 31: Band structures calculated from first-principles density functional theory (DFT) for WS₂ and MoS₂ [96].

localized, defect-bound excitons and occurs at about 760 nm. The A exciton was observed to shift from 750 nm at room temperature to 730 nm at low temperature, whereas the D^0X peak exhibited no such shift. The full-width half max (FWHM) of the X peak is determined to be dominated by inhomogeneous broadening, as confirmed with the 2DCS shown later, and has a value of $\Gamma_{in} \approx 50 \text{ meV}$. The presence of such large

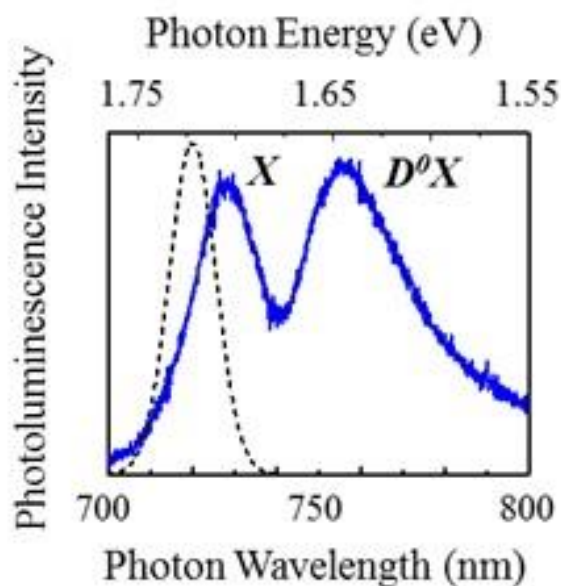


Figure 32: Low temperature PL taken at 10K (blue curve) showing two peaks, the A exciton (X) and defect-bound excitons (D^0X) at 730 nm and 760 nm, respectively.

inhomogeneities can likely be ascribed to differences in local potentials due to chalcogenide vacancies or other impurities like water vapor adsorption.

The peaks in the PL were further identified with the aid of polarization analysis. The lower energy peak at 730 nm was shown to exhibit some degree of linear polarization following excitation by the linear polarized 532 nm laser light, but the peak at around 760 nm did not exhibit any linear polarization. The appearance of linear polarization can only be seen if a coherent superposition of exciton valley states is being generated which is consistent with previous work showing the linear polarization of excitons in WSe₂ [63]. The assignment of the lower energy peak to localized, defect-bound exciton states and not trion states is in part due to the separation of the two peaks. The two peaks are separated by about 50 meV which is nearly a factor of two larger than

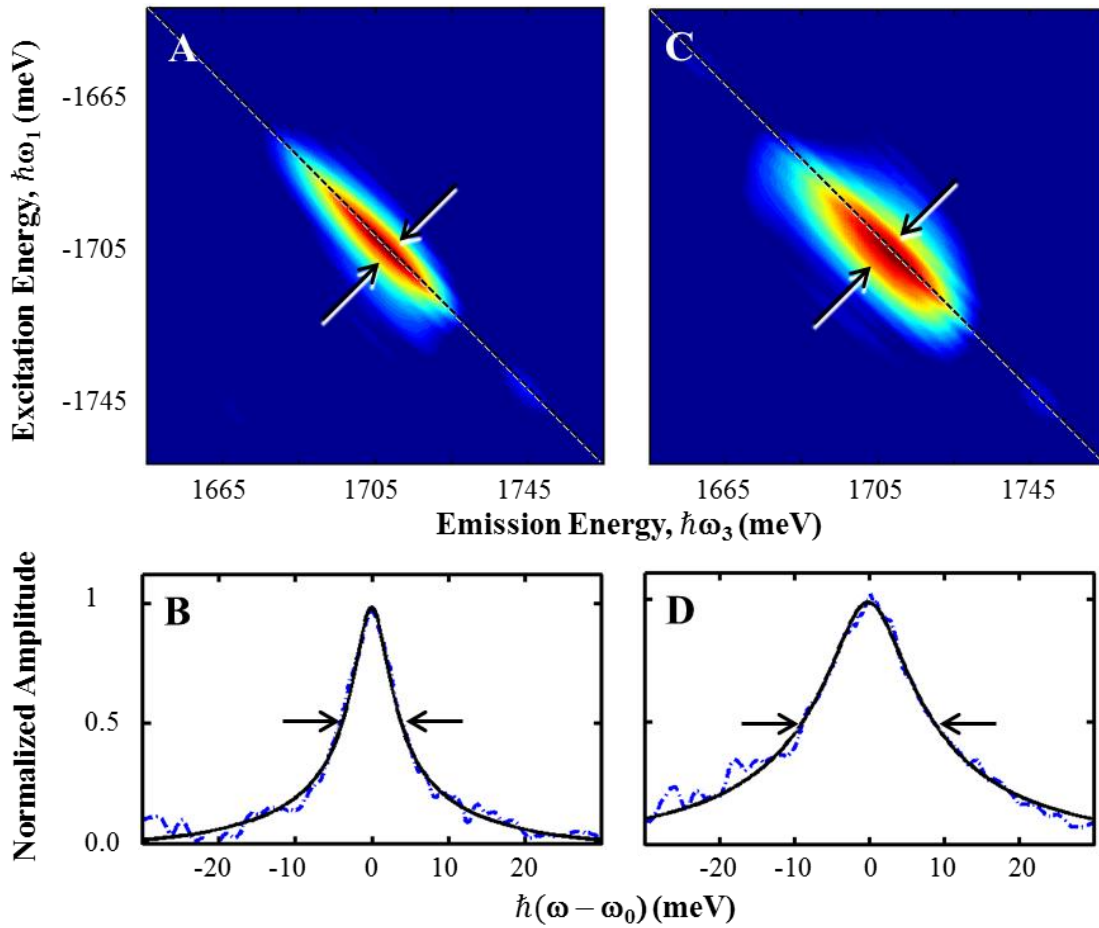


Figure 33: The photon echo appears as a single peak along the diagonal in the 2D spectra. The peak is inhomogeneously broadened along the diagonal and homogeneously broadened along the cross-diagonal. All of the data shown were taken with co-circularly polarized pulses. The data in a) was taken at an excitation density of $\sim 1.3 \times 10^{11}$ excitons/cm². b) Shows a slice along the cross-diagonal indicated by the arrows in a) fitted to the square root of a Lorentzian. The fitting yields a half-width half max (i.e. homogeneous linewidth) of $\gamma = 2.7 \pm 0.2$ meV ($T_2 = 240 \pm 20$ fs). c) Shows a 2D spectrum for an excitation density of $\sim 1.3 \times 10^{12}$ excitons/cm² and d) is the corresponding fit yielding a value of $\gamma = 6.1 \pm 0.3$ meV ($T_2 = 110 \pm 5$ fs).

the 30 meV binding energy difference between trions and excitons [63, 168]. This assignment of the neutral, defect-bound exciton peak is also consistent with the PL peak assignments in previous work as well [168].

5.3 2DCS STUDIES OF EID

After verifying the position of the exciton resonance with PL, we were then able to move on to 2DCS measurements. The 2D rephasing amplitude spectra were obtained by coherently exciting the samples with three excitation pulses focused to a 35 μm spot which generates a nonlinear signal field $E_S(\tau_1, \tau_2, \tau_3)$. The nonlinear signal E_S is resolved through spectral interferometry using a fourth, phase-stabilized reference pulse. These interferograms are taken at various delays of τ_1 and a Fourier transform is then performed with respect to this time-delay in order to generate a 2D spectrum. In the 2D plots, the photon echo signal appears as a single peak along the diagonal (see Figure 33) which indicates that the signal evolves at the same frequency during both the τ_1 and τ_3 time periods. We use a value of $\tau_2 = 0 \text{ fs}$ in order to maximize the signal-to-noise. Larger values of τ_2 were used, up to 200 fs , but the signal did not change except in decreased signal-to-noise. In the figure we can also see that the $\hbar\omega_1$ axis is plotted as a negative energy because the system evolves with the opposite phase accumulation as compared to the detection time, the $\hbar\omega_3$ axis. This negative sign is the result of the first pulse being a conjugated pulse which is the typical pulse ordering in a photon echo experiment.

Shown in Figure 33 are two 2D plots at different excitation densities and their respective line cuts along the cross-diagonal direction. Figure 33a) and Figure 33b) represents the signal from co-circularly polarized pulses with an excitation density of

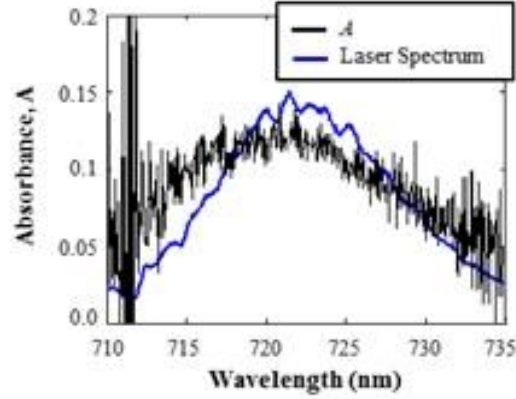


Figure 34: Absorbance found through differential reflection measurement done at 17 K using the laser spectrum (blue curve), yielding a maximum of $A = 0.12$ at the peak of the laser.

$\sim 1.3 \times 10^{11}$ excitons/cm² taken at 10 K. Figure 33c and Figure 33d represents the signal from an excitation density an order of magnitude greater, with clear broadening occurring along the cross-diagonal, the result of excitation induced dephasing (EID) [90]. The excitation densities were calculated using the expression

$$N_X = \frac{P_{ave} T_p (1 - R)(1 - e^{-\alpha L})}{\pi r^2 E_{ph}} \quad (82)$$

where P_{ave} is the average power per beam, $T_p = 12.5$ ns is the laser pulse time separation, $R = 0.15$ takes into account reflection losses, $A = 1 - e^{-\alpha L}$ is the linear absorbance of the WSe₂ monolayer, $r = 17.5$ μ m is the focused beam radius, and $E_{ph} = 1710$ meV is the photon energy. The absorbance was determined by measuring the fractional change in the laser reflectance from the WSe₂ monolayer flake relative to the substrate reflectance. The differential reflectance (δ_R) is related to the linear absorbance of a material on a transparent substrate by [16]

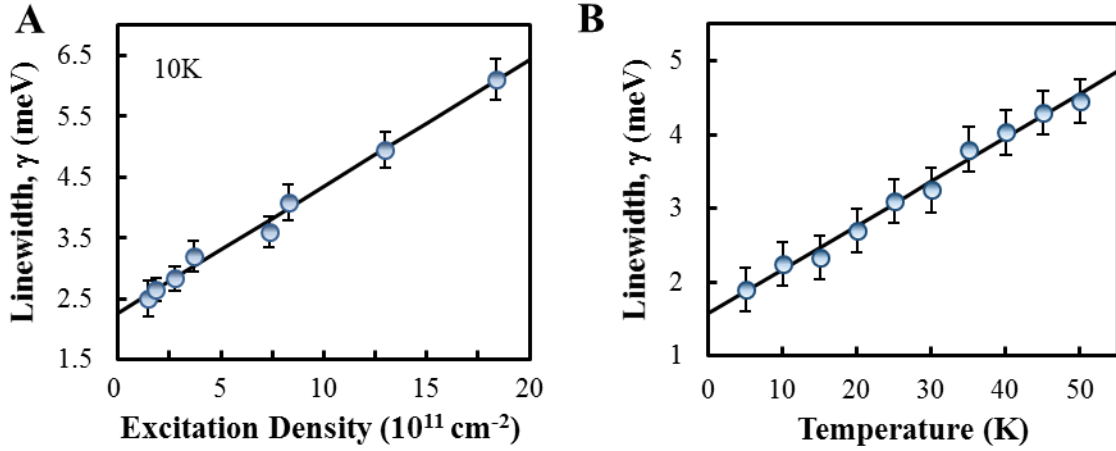


Figure 35: a) The measured homogeneous linewidth as a function of excitation density taken at 10 K. The solid line is a fit of equation (84) with $\gamma_0 = 2.3 \pm 0.3 \text{ meV}$ and a slope of $\gamma^* = 0.21 \pm 0.05 \times 10^{-11} \text{ meV cm}^2 \text{ exciton}^{-1}$. b) The measured homogeneous linewidth as a function of temperature. The solid line is a fit of equation (85) giving a exciton-phonon coupling strength of $\gamma_{ph} = 60 \pm 6 \mu\text{eV/K}$ and a zero temperature offset of $\gamma_0(0) = 1.6 \pm 0.3 \text{ meV}$.

$$\delta_R(\lambda) = \frac{4}{n_s^2 - 1} A \quad (83)$$

where $n_s = 1.76$ is the refractive index of the sapphire substrate. The absorbance is shown in Figure 34. This measurement was carried out in a comparable setup to the one in which 2DCS was performed because the spot sizes achievable were much smaller than possible in the 2DCS setup. The laser was tuned to a similar wavelength as that used in the 2DCS measurements with a sample temperature of 17 K. The absorbance measured was $A \approx 0.12$.

The FWHM is found by fitting the cross-diagonal line cuts to the square root of a Lorentzian with the FWHM equal to 2γ [95]. The cross-diagonal slice in a 2D rephasing

measurement represents the homogeneous broadening inherent in the system. For the data in Figure 34, fitting to a square root Lorentzian, we find a value of $\gamma = 2.7 \pm 0.2 \text{ meV}$, which corresponds to an exciton coherence time of $T_2 = \hbar/\gamma = 240 \pm 20 \text{ fs}$. For the data in Figure 33c, for which we have excited the sample with much higher power, we find a coherence time of $110 \pm 5 \text{ fs}$. The FWHM of the peak along the diagonal was not analyzed and does not reflect the actual inhomogeneous broadening present in the system. The peak width along the diagonal, in this experiment, is limited by the laser bandwidth which was much smaller than the width of the exciton resonance. To get a better idea of the inhomogeneous broadening present in the system, it is more instructive to look at PL spectrum. Previous work has shown through transient absorption measurements that the exciton lifetime, T_1 , does not change appreciably as a function of the excitation densities studied here [169]. This result implies that the EID effects seen here can be attributed to elastic exciton-exciton scattering in which phase disruptions occur in the absence of any significant population relaxation.

Further measurements were taken in order to better determine the dependence of homogeneous linewidth on the excitation density, these results are shown in Figure 35a. All the data shown were taken at 10 K and were analyzed following similar procedures used previously on quantum wells [170, 171]. We also took care to confirm that all measurements were indeed performed in the $\chi^{(3)}$ regime by checking to see if the signal field amplitude varied proportionally with the product of the three excitation fields. Excitation induced dephasing can be modeled by the following expression:

$$\gamma(N_X) = \gamma_0 + \gamma^* N_X, \quad (84)$$

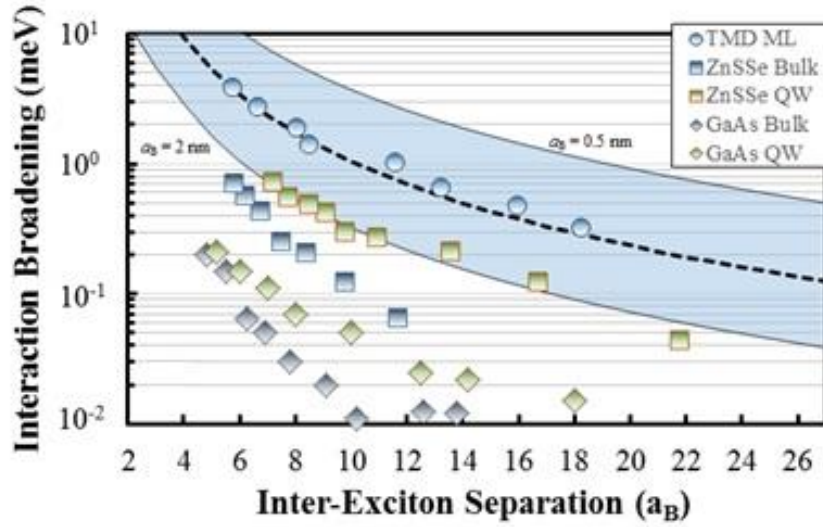


Figure 36: Comparison of interaction broadening as a function of inter-exciton separation for different materials. The horizontal axis is normalized to the exciton Bohr radius for each system. The shaded region is the expected exciton separation distance for monolayer WSe₂ for Bohr radii in the range of $0.5 \text{ nm} < \mathbf{a}_B < 2 \text{ nm}$ and the dashed line is for $\mathbf{a}_B = 1 \text{ nm}$.

where γ_0 is the zero-density linewidth and γ^* is an exciton-exciton interaction parameter. Equation (84) is used to fit the data shown in Figure 35a, which yields $\gamma^* = 0.21 \pm 0.05 \times 10^{-11} \text{ meV cm}^2 \text{ exciton}^{-1}$ and an extrapolated zero-density homogeneous linewidth of $\gamma_0 = 2.3 \pm 0.3 \text{ meV}$. The interaction parameter found here for monolayer WSe₂ is of the same order of magnitude as in quasi-2D semiconductor quantum wells, which would imply stronger interaction broadening between the tightly bound excitons in the monolayer TMDCs (Bohr radius $\sim 1 \text{ nm}$) compared to weakly bound excitons in quantum wells (Bohr radius 5-10 nm) [90, 172-174]. Stronger exciton-exciton interaction is indeed consistent with reduced dielectric screening of the Coulomb interactions in atomically-thin materials [175, 176]. This effect is more clearly illustrated in Figure 36 in which we've plotted exciton-exciton EID, defined as $\Delta\gamma = \gamma(N_X) - \gamma(0)$, as a function

of the inter-exciton separation distance r_x normalized to the exciton Bohr radius, a_B . For comparison, we also show on the same plot the interaction strength of various other materials, both 2D and bulk. The exciton spacing for the materials shown can be calculated from the excitation density using the formulas $r_x = (\pi a_B^2 N_x)^{-1/2}$ and $r_x = (4\pi a_B^3 N_x / 3)^{-1/3}$ for 2D and 3D systems, respectively. The measured EID for monolayer WSe₂ appear as solid circles in the plot and the dashed line is a fit to the data. Since the Bohr radius for our sample is not precisely known, the data in the figure (dashed line) was produced with an estimated value of $a_B = 1$ nm and the shaded region is the calculated $\Delta\gamma$ for a range of TMD exciton Bohr radii $0.5 \text{ nm} \leq a_B \leq 2 \text{ nm}$. Larger Bohr radii means, of course, smaller normalized exciton separation. From the figure it is obvious that monolayer WSe₂ exhibits significantly more exciton-exciton interaction than more conventional semiconductor systems [173, 174] due mostly to the reduced dielectric screening of the Coulomb force inherent in ultra-thin semiconductors [177].

5.4 2DCS STUDIES OF PHONON INTERACTIONS

In addition to studying the role of excitation density on homogeneous broadening, we also did careful studies of the role of phonon-exciton interactions on the homogeneous linewidth. In order to do this, we repeated the linewidth density dependent measurements, but this time as a function of temperature, the results of which can be seen in Figure 35b. The extrapolated zero-linewidth is shown for temperatures all the way up to 50 K and is seen to increase linearly from 19 ± 0.3 meV at 5 K to 4.5 ± 0.3 meV at 50 K. At these temperatures, the linear dependence of the homogeneous linewidths is analogous to exciton dephasing in semiconductor quantum wells as the result of the absorption of acoustic phonons with energies smaller than $k_B T$, where T is the sample temperature [178]. The phonon absorption may be modeled by

$$\gamma(T) = \gamma_0(0) + \gamma_{ph}T , \quad (85)$$

where γ_{ph} denotes the exciton-phonon coupling strength and $\gamma_0(0)$ is the residual exciton homogeneous linewidth in the absence of exciton-exciton and exciton-phonon interaction. Equation (85) is used to fit the data shown in Figure 35b which gives a value of $60 \pm 6 \mu\text{eV}/\text{K}$ for γ_{ph} , a factor of 5-10 larger than that of quasi-2D semiconductor quantum wells [172, 178] and twice as large as other bulk TMDC materials [179]. From the fitting, we also find a value of $1.6 \pm 0.3 \text{ meV}$ for $\gamma_0(0)$.

The residual homogeneous linewidth of $\sim 1.6 \text{ meV}$ is free of the effects of exciton-exciton and exciton-phonon interaction effects and therefore must be due to the exciton population relaxation (T_1 processes) and pure dephasing associated with impurities or defects (T_2^* processes). This is further supported by the recent fast population decay features found in transient absorption measurements and time-resolved photoluminescence [168]. There are also a large number of impurities and defects present in the sample, this can be seen in the PL which shows a large impurity peak and also large exciton inhomogeneous broadening on the order of $\sim 50 \text{ meV}$. Pure dephasing may also play a role in the residual homogeneous linewidth. This pure dephasing may arise from charge capture events that have been shown to shift the exciton energies in quantum dots on picosecond timescales [180].

5.5 CALCULATING HOMOGENEOUS LINEWIDTH

One might expect that in higher quality samples the residual homogeneous linewidth would be much smaller than what is measured here, but recent calculations have shown this might not be the case [181]. This recent work has shown that in samples with the less defects, *i.e.* higher quality samples, the localization length of the excitons

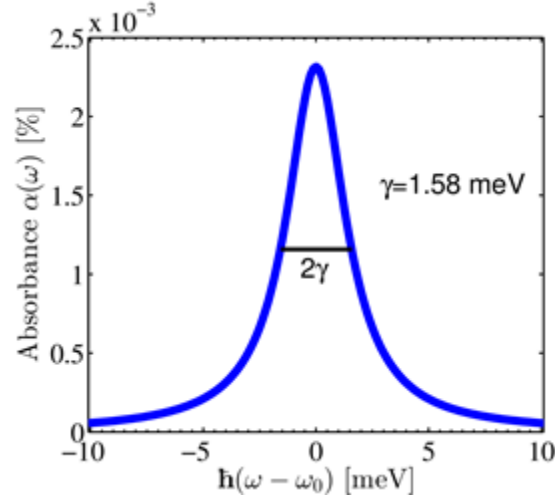


Figure 37: Calculated frequency dependent homogeneous absorbance $\alpha(\omega)$ of delocalized excitons in WSe₂. The calculations show a lower limit for the homogeneous linewidth of $\gamma = 1.58$ meV (or 2.4 ps⁻¹) due to radiative coupling.

increases leading to a decrease in the radiative lifetimes. Since excitons in TMDCs have small radii, and therefore large oscillator strengths, one would expect their radiative lifetimes to be particularly short and so is consistent with the homogeneous linewidths measured here. Through microscopic calculations of our own, we also show that the radiative decay becomes the dominant dephasing process in the limit that the excitons are completely delocalized in an ideal monolayer TMD crystal. The microscopic calculations we perform start from Maxwell's equations and uses the boundary conditions for a two-dimensional crystal between two media with indices of refraction n_1 and n_2 . From this starting point, we calculate the frequency-dependent excitonic absorbance defined as $\alpha(\omega) \equiv 1 - T(\omega) - R(\omega)$. This calculation leads to the following analytic expression for the frequency-dependent absorbance

$$\alpha(\omega) = \frac{\frac{\omega}{c_0 n_1} \text{Im}[\chi_{2D}(\omega)]}{\left| \frac{1}{2} \left(1 + \frac{n_1}{n_2} \right) - i \frac{\omega}{2c_0 n_1} \chi_{2D}(\omega) \right|^2} \quad (86)$$

where c_0 is the speed of light in vacuum and $\chi_{2D}(\omega)$ describes the linear response of the TMD monolayer to an optical pulse. The linear response of the TMD monolayer is a material parameter which is calculated using the semiconductor Bloch equations. Through this approach, we find the following expression for the linear response of the TMD monolayer

$$\chi_{2D}(\omega) = \frac{1}{\epsilon_0 \omega^2} \sum_{\nu \xi s} \frac{\Theta_{\nu \xi}^s}{E_{\nu \xi}^s - \hbar \omega - i \gamma_0} \quad (87)$$

where $\Theta_{\nu \xi}^s$ are the exciton eigenfunctions, $E_{\nu \xi}^s$ are the eigenvalues of the Wannier equation and γ_0 is a small parameter necessary for the numerical calculations, but does not affect the calculation of the radiative lifetimes in any way. The indices ν, ξ and s are indices describing the exciton state, the valley index and the spin, respectively. Figure 37 shows the absorbance profile of the A exciton based on the calculations described above. From the calculations we find a homogeneous linewidth of 1.58 meV which corresponds to a radiative lifetime of about 0.2 ps. This fast radiative decay of 0.2 ps represents a lower bound and can be explained by the large oscillator strength inherent to monolayer TMDC. The calculation outlined here is consistent with the extrapolated homogeneous linewidth found through our 2DCS measurements.

Chapter 6: Conclusion and Outlook

6.1 CONCLUSION

In any material that displays potential for new and exciting optoelectronic applications, gaining insight into the fundamental exciton properties is key to guiding further research. While bulk TMDCs have been studied for decades, the recent explosion in research on monolayer TMDCs has made the need to understand these fundamental properties even more urgent. Some of the seminal and recent experiments in this field have uncovered intriguing properties including: coupled spin and valley pseudospin degrees of freedom [16, 20], exceptionally large binding energies [159, 182] with non-hydrogenic exciton Rydberg series [159, 160], excitons with robust electronic and valley coherence [63, 161] as well as coupled spin and valley pseudospin degrees of freedom [16, 20]. Despite the multitude of exciting new properties uncovered by these experiments, much is still left to be learned in order to uncover the unique exciton physics in monolayer TMDCs.

Two of the fundamental parameters that characterizes the exciton quantum dynamics is the excited state population relaxation rate (Γ) and the dephasing rate (γ), the two of which are inextricably related to each other through the relationship $\gamma = \Gamma/2 + \gamma^*$. Understanding these basic properties of the exciton dynamics will be key to developing TMDC-based optoelectronics, valleytronics, and quantum information devices [96]. Since the dephasing rate sets the timescales over which excitons can be coherently manipulated, knowledge of the homogeneous linewidth will be crucial to the development of many optoelectronic devices utilizing TMDCs, including coherent valleytronic devices. Examples of the delicate balance between dephasing and energy transfer include semiconductor lasers [165] and photosynthetic proteins [166]. These systems are examples in which the homogeneous linewidth is delicately balanced so as to

achieve adequate overlap to facilitate energy transfer between inhomogeneously broadened resonances, but not too broad such as would cause decoherence before any energy transfer.

This dissertation has focused mainly on our results in measuring, for the first time, the homogeneous linewidths in monolayer WSe₂. We have shown that at low temperature both exciton-exciton and exciton-phonon interactions play a significant role in exciton dephasing. These dephasing processes have been shown to compete on sub-picosecond time scales, which is in sharp contrast to conventional semiconductors. For example, 10 nm thick GaAs wells typically exhibit picosecond long coherence times dominated by pure dephasing from exciton-phonon coupling, and tens of picoseconds long radiative lifetimes [183, 184]. Knowledge of such a basic property of the exciton dynamics will help shape future directions in monolayer TMDC research as well as facilitate the design of optoelectronic devices and photovoltaic devices based on these materials.

This dissertation has also gone into much detail on the benefits and implementation of 2DCS. Much time was spent in discussing the types of 2D spectra possible, the interpretation of 2D spectra, and lineshape analysis. We have also spent a great deal of effort on describing the experimental implementation of 2DCS, including details on noise filtering through Fourier transform as well as noise filtering through phase cycling.

6.1 OUTLOOK

There are still many avenues to explore with little to no changes necessary in the experimental aspect. Since co-circularly polarized rephasing one-quantum scans have been the main topic of this dissertation, the next logical step would be to do cross-

circularly polarized rephasing one-quantum scans. One could take rephasing quantum scans at various delays of T for different combinations of left and right circular polarizations of beams A , B and C . For example, using left circularly polarized light for beams A and B and right circularly polarized light for beams C and *reference* would allow us to probe valley relaxation dynamics. By looking at the dipole selection rules for optical transitions in these materials (see Chapter 2), many more dynamics may be probed using other combinations of left and right hand circular polarization. Also, by taking these spectra at various delays of T we can also get some idea of the population decay. In addition, we can gain a lot more insight into the population decay by scanning the T delay directly, *i.e.* zero-quantum rephasing scans. These scans can be done for co-circular polarization and for various values of power and temperature in order to see how the population dynamics change as a function of excitation density and temperature.

All of the data 2DCS reported in this dissertation has been done on the lower energy peak in the PL (see Chapter 5), but many of the same experiments may be repeated on the higher energy peak, *i.e.* the localized, defect-bound excitons. The first set of experiments to do on the defect-bound excitons would be to repeat the one-quantum rephasing scans in order to determine the homogeneous linewidth of these localized excitons.

Appendix: Pump-Probe on Hybrid Structures

In this appendix I present some minor work done on hybrid metallic-semiconductor materials comprising of a GaAs quantum well coupled to surface plasmon polaritons (SPPs) in a gold grating. Because the hybrid materials discussed here were taken on a very different setup and are outside the range of discussion of the bulk of my dissertation work, it is left as an appendix.

I begin by briefly introducing the applications and motivations for studying these materials and then move on to describing the sample and experimental design. The chapter concludes with a discussion of the results and fitting.

A.1 APPLICATIONS AND MOTIVATIONS

Hybrid metallic-semiconductor nanostructures have a wide array of potential applications including all-optical switches [185-187], single photon transistors [188], and nanolasers [189-191]. These materials can come in a wide variety of geometries, but usually rely on the proximity of excitons in a semiconductor structure to SPPs in a nearby metallic structure. Hybrid devices combine both the field-concentrating properties of plasmonic materials and the large optical nonlinearities present in semiconductors. The ability of plasmonic structures to confine light to sub-wavelength dimensions has been previously exploited in a variety of hybrid systems including organic semiconductors [192], J-aggregated molecules [193], quantum wells [194], to quantum dots [195]. Spectroscopic [194, 196-198] and theoretical studies [199] of hybrid devices have demonstrated enhancements in luminescence yield, strong SPP-exciton coupling and decreased exciton radiative lifetimes for QWs coupled to plasmon resonances. Other contradictory reports, however, have shown suppression of luminescence for QWs in the vicinity of metal nanostructures [200, 201].

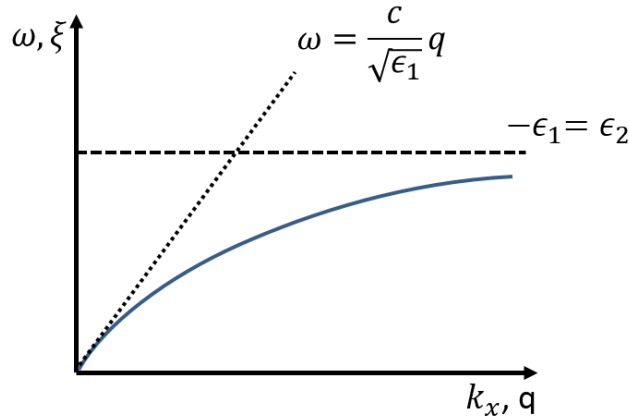


Figure 38: The solid line shows the dispersion curve for surface plasmons which reaches an asymptotic value when $-\epsilon_1 = \epsilon_2$, where ϵ_1 and ϵ_2 are the frequency dependent dielectric functions for the surrounding vacuum and metal, respectively. This occurs at $k_x \rightarrow \infty$, i.e. where k_x is the plasmon wavevector in the direction of propagation and ξ is the frequency. The dotted line is the dispersion curve for a photon.

Because metallic-semiconductor materials have the ability to couple plasmons to quantum emitters like excitons, these materials also show promising applications in the growing field of quantum plasmonics. As an emerging off-shoot of the field of plasmonics, quantum plasmonics has the potential to go beyond just interfacing photonics with nanoelectronics, but shows promise in addressing challenges in quantum information processing, qubit scalability, and qubit communication [202].

Very little is known about how quantum coherence is affected when coupled to plasmonic excitations. Linear studies have been performed on GaAs QWs coupled to gold gratings, demonstrating significant red-shifting and broadening of the exciton resonances as a result of the strong coupling [194], but to date no nonlinear studies have

been performed and therefore information regarding the coherent interaction in these coupled systems is limited.

Pump-probe, in limited cases, can provide information about the coherent dynamics in a system. In this work, we are particularly interested in how quantum coherence is modified in hybrid structures. Very fast dephasing times have been reported in metallic nanostructures, on the order of tens of femtoseconds, while the dephasing times in semiconductor heterostructures can be very long. In quantum wells, the exciton dephasing time lasts a few picoseconds to tens of picoseconds at low temperatures and this dephasing time can be extended close to a nanosecond in quantum dots. In this work we aim to answer the question whether the fast dephasing time in the metallic nanostructure becomes the limiting factor in a hybrid structure.

A.2 SAMPLE DESIGN

The sample we investigate consists of a gold grating deposited on top of an AlGaAs/GaAs quantum well. The AlGaAs/GaAs quantum well consists of a 10 nm GaAs well embedded between $\text{Al}_{0.3}\text{Ga}_{0.7}\text{As}$ barriers grown on top of a GaAs substrate by molecular beam epitaxy (MBE). The gold grating and GaAs quantum well are separated by a 20 nm buffer in order to ensure close proximity of the excitons in the GaAs well and plasmons in the gold grating. Plasmons are a collective oscillation of the electron gas that can be coupled to light through the use of various techniques. The plasmon dispersion curve is shown schematically in Figure 38. From the figure we can see that the dispersion curves for light and plasmons do not cross, but by using a prism or grating structure on the surface of the metal, one can effectively increase the wavevector of the incoming light enough such that the dispersion curves intersect. For our sample we use a gold grating which is created by first depositing a gold

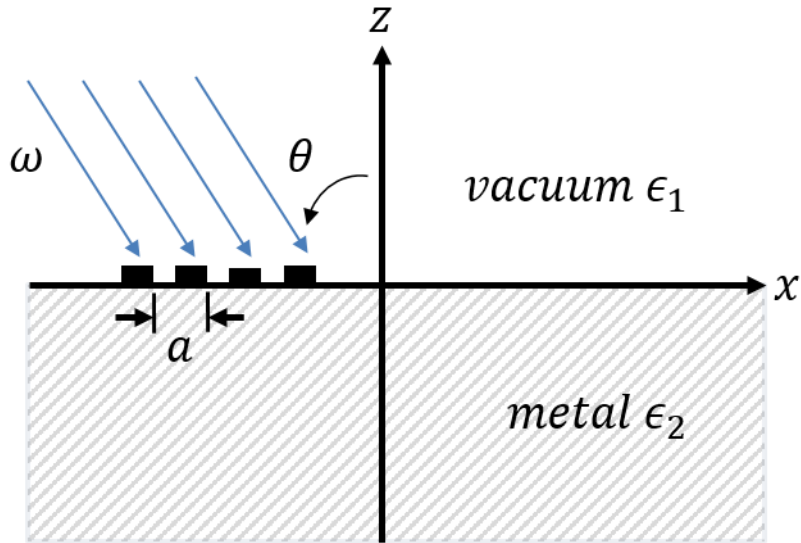


Figure 39: Coupling light to a surface plasmon. The light must be polarized in the x-direction.

film of 140 nm. Slits are then etched into the gold film with electron beam lithography forming a gold grating structure with grating period, $a=500$ nm, and grating width, $w=370$ nm. The gold grating structures are approximately $100 \mu m$ on each side and surrounded by bare quantum well, which allows us to move between the hybrid structure and bare quantum well with ease. The dimensions of the gold grating structure are chosen such that plasmons at the semiconductor-metal interface will be created for 800 nm (1.55 eV) light at an incident angle of 34° to the normal. This condition can be written as follows

$$\frac{\omega}{c} \sqrt{\epsilon_1} \sin(\theta) + \frac{2\pi m}{a} = k_x, \quad (88)$$

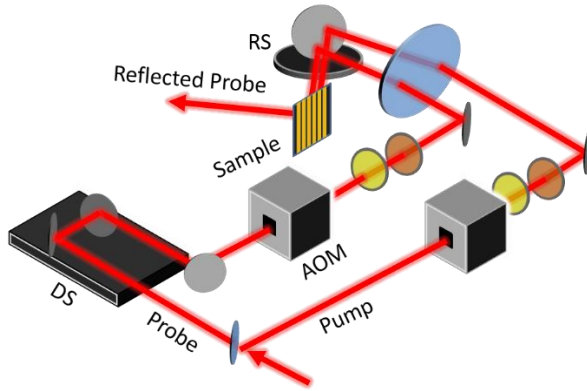


Figure 40: Schematic of experimental setup.

where ω is the frequency of the incident light, a is the period of the grating and m is an integer (see Figure 39). This well-known result can be found in any introductory textbook on surface plasmons [97].

For 800 nm light, excitons will also be excited in the quantum well leading to a coupled, hybrid oscillator which manifests as red-shifting of the exciton resonances. By observing the time-resolved, pump-probe signal of the LH peak, we can see quantum beats in the signal indicating non-radiative, coherent coupling between the LH and HH exciton transitions.

A.3 EXPERIMENTAL APPARATUS

The experimental design is a simple homodyne-detected differential reflection setup shown in Figure 40. The excitation source is a *Spectra-Physics Tsunami* (Model 3960-X1BB) Ti:sapph laser that produces pulses of 150 fs in duration with 15 nm of bandwidth. The Ti:sapph beam is split into a pump and probe beam with *CVI* beamsplitters (FABS-790-45S-PW-1004-UV) which are then intensity modulated by acousto optic modulators (AOMs) at 0.5 MHz and 0.515 MHz, respectively. The AOMs

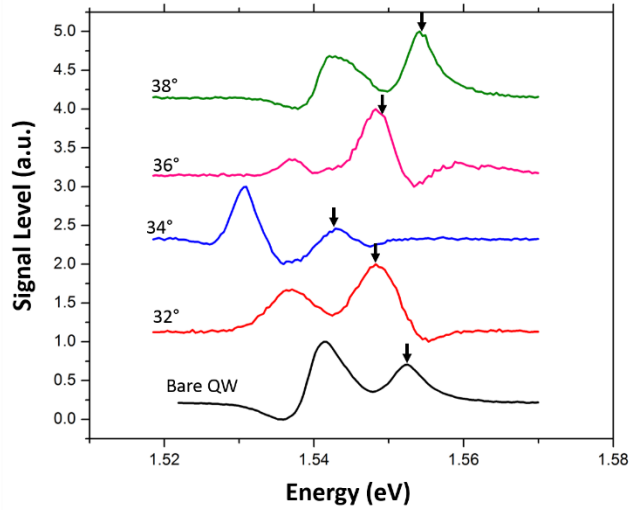


Figure 41: Spectrally resolved pump-probe taken at 4 K on the bare quantum well and on the hybrid structure at 4 different angles. The black arrows indicates the position of the light hole (LH) transitions. A clear red-shift can be seen as the angle of incidence approaches the coupling angle of 34° . At this angle, the incident light excites an SPP as well as an exciton transition. Because of the close proximity of the QW to the grating, the SPP and exciton become coupled and a redshift in the spectrum is observed.

we employ are made by *Gooch and Housego* (Model 46080-2-LTD) and consist of a Tellerium Dioxide (TeO_2) crystal. The mechanism of action through which AOMs modulate the beam is by distortion of the local index of refraction of the TeO_2 crystal. This distortion is produced by a sound wave propagating through the crystal and presents a grating to incident light. The TeO_2 based AOM is designed to operate at 80 MHz. When the Ti:sapph is incident on this grating, a Bragg diffracted first order beam in the operating wavelength range of 700-900 nm can be produced. The 80 MHz driving signal is then modulated at 0.5 and 0.515 MHz for the pump and probe beams, respectively, producing the intensity modulated excitation beams. The 80 MHz driving signal and two

modulation signals are produced by *Novatech* signal generators (Model 409B). The signals from the *Novatech* are sent into mixers (ZAD-1-1+) and splitters (ZSC-2-1+) from *MiniCircuits* in order to produce the modulated 80 MHz driving signal that is then sent to voltage amplifiers before being sent to the AOMs.

An *Aerotech* (Model ALS130H-0050) delay stage (DS) in the probe path is used to control the relative delay. After the AOMs, the pump and probe pass through $1/2 \lambda$ plates (*Special Optics* Model 8-9014-1/2-700-1550 nm) and polarizers (*Newport* Polarcor 740-860 nm 05P109AR.16), which allows us to control the intensity and polarization of the beams hitting the sample. The two beams are then focused onto the sample at angles which can be varied through use of a *Newport* rotation stage (RS) mounted mirror and the reflected probe is then sent through a spectrometer (*Acton* SpectraPro 2750) and onto a single-channel detector (*Thorlabs* DET36A) that is connected to a lock-in amplifier (*Stanford Research* SR830). The signal is homodyne detected at the difference frequency of 15 kHz.

A.3 RESULTS

The plasmonic resonances excited vary as the angle of incidence. We first perform angular- and spectrally-resolved measurements at 4 K in order to identify the angle at which the strongest exciton-plasmon occurs. For these measurements we set the incident pump/probe polarizations perpendicular to the grating structure. This data is shown in Figure 41 where we have measured pump-probe spectra at four different angles on the

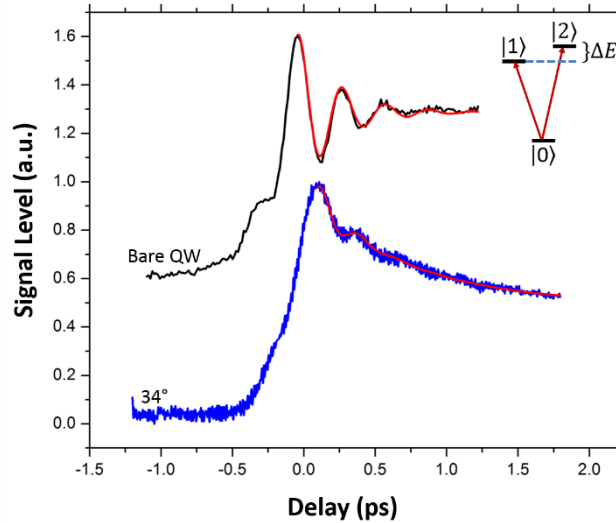


Figure 42: Time-resolved pump-probe of the LH transitions on the bare QW (black trace) and hybrid structure (blue trace) at 34° . All fits are shown in red. In the upper-right we show the schematic of the V-level diagram that describes our system. $|1\rangle$ is the HH transition and $|2\rangle$ is the LH transition.

hybrid structure as well as on the bare quantum well. The angle-dependent spectra shows a red-shift of ~ 10 meV at 34° incidence with decreasing red-shift at angles greater than, or less than, 34° indicating that the strongest exciton-plasmon coupling occurs at $\sim 34^\circ$. Previous experiments have seen similar red-shifts on these types of materials [194].

To investigate the change in quantum coherence in hybrid structures, we compare the quantum beats in the pump-probe signal in the surrounding bare quantum well to that of the hybrid structure at the resonant coupling angle of 34° . The differential reflection signal is presented in Figure 42 which represents the temporal behavior of the respective LH transitions shown in Figure 41. For the bare quantum well, we measure a much more pronounced beating behavior and no measurable population decay on the timescale of the

delay. The differential reflection signal measured is fit to an exponential decay plus an exponentially decaying sinusoid

$$DR(\tau) = Ae^{-\Gamma\tau} + Be^{-\gamma_{12}\tau} \cos(\delta\tau), \quad (89)$$

where Γ is the population relaxation rate, γ_{12} is the dephasing rate for the Raman coherence between the HH (state |1) in Figure 42) and the LH (state |2)), and $\Theta(\tau)$ is a step function ensuring the signal is zero for negative time delays. The Raman period (T_R) is related to the LH-HH energy splitting ($\Delta E = \hbar\delta$) by $T_R\delta = 2\pi$. The motivation for this model is discussed later in terms of a density matrix approach.

From the fit to equation (89) we find values of $\gamma_{12}^{-1} = 0.27 \pm 0.01$ ps and $T_R = 0.152 \pm 0.001$ ps for the Raman coherence time and Raman period, respectively. The Raman period, from the fitting, corresponds to a LH-HH splitting of ~ 27 meV, well within the measured spectral spread of the LH-HH transitions (~ 30 meV) when inhomogeneous broadening is taken into account. For the hybrid structure, at the resonant coupling angle, pronounced population decay is measured as well as a significant reduction in the Raman coherence time. The fitting yields values of $\Gamma^{-1} = 0.70 \pm 0.03$ ps, $\gamma_{12}^{-1} = 0.16 \pm 0.03$, and $T_R = 0.134 \pm 0.005$ ps (~ 30 meV), where Γ^{-1} is the population relaxation time. On the hybrid structure, at the resonant coupling angle, the Raman coherence time is reduced by almost a factor of two, but still much longer than the coherence times for plasmons. The measured increase in population relaxation and decrease in Raman period close to the resonant coupling angle is well understood and has been reported previously in similar hybrid materials [194, 203].

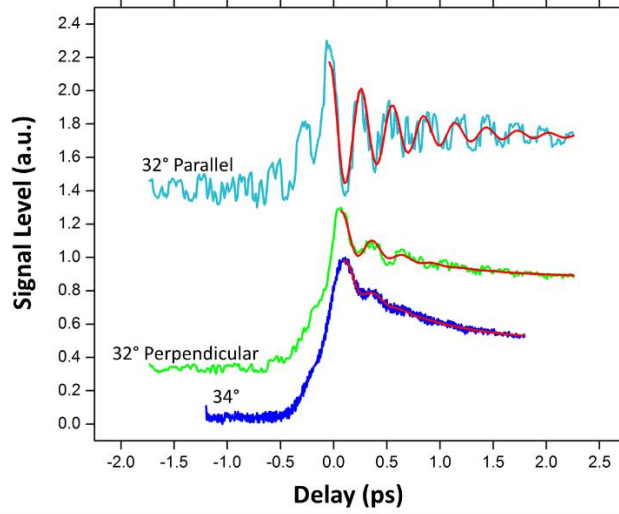


Figure 43: Time-resolved pump-probe of the LH transition at 32° on the hybrid structure. With the incident polarization parallel to the gold grating (light blue trace), no SPP is excited. With the incident polarization perpendicular to the gold grating a hybrid SPP-exciton mode is excited and the Raman coherence is markedly shorter. The data for 34° is reproduced (blue trace) for comparison.

We further examine the quantum beating behavior in these hybrid materials by performing polarization measurements near the resonant coupling angle. Figure 43 shows time-resolved pump-probe scans taken at 4 K and at an incident angle of 32° . The top trace (light blue) was measured for an incident polarization, of both pump and probe, parallel to the grating structure for which no plasmon excitation is expected. The middle trace (green) was taken for incident polarization perpendicular to the grating structure for which weaker exciton-plasmon coupling is expected compared to the bottom trace in blue (reproduced from Figure 42). The fitting gives timescales of $\gamma_{12}^{-1} = 0.62 \pm 0.2$ ps and $T_R = 0.147 \pm 0.001$ ps for parallel polarization. For perpendicular polarization the fitting yields timescales of $\Gamma^{-1} = 0.76 \pm 0.06$ ps, $\gamma_{12}^{-1} = 0.26 \pm 0.03$ ps, and $T_R = 0.144 \pm 0.003$ ps.

No significant population decay was measured for the case of parallel polarization. As one can see from the fitting, at 32° the population lifetimes and Raman coherence are slightly longer as compared to the timescales at the resonant coupling angle. The effect of exciton-plasmon coupling is even more pronounced when comparing the perpendicular and parallel polarizations where we see the Raman coherence time change by more than a factor of two. The much longer Raman coherence times seen for the case of parallel polarization, as compared to bulk, can be explained by the large pump intensities required on the hybrid structures. As these conditions were kept constant across all scans, more pronounced excitation induced dephasing is expected on the bare quantum well.

While the kind of pump-probe experiments employed in this work are typically used to investigate incoherent population relaxation, information on quantum coherence can be extracted in certain cases[204]. In particular, we have investigated non-radiative coherence in a three-level “V” (see upper right panel Figure 42) system using homodyne detected differential reflection experiments. The form of equation (89) can be derived by analyzing the quantum dynamics of the V-level system, which can be described by the density matrix formalism. The dynamics of the density matrix are governed by the master equation,

$$i\hbar \frac{d\rho}{dt} = [H, \rho] + i\hbar \left. \frac{d\rho}{dt} \right|_{relaxation}, \quad (90)$$

where $H = H_0 + V = H_0 - \hat{\mu} \cdot \mathbf{E}$. The first term in the Hamiltonian is the diagonalized matrix for the eigenstates of the excitation level diagram and the second term describes the coherent coupling of the system to the laser field. The nonzero elements of the dipole

operator correspond to the transitions shown in the upper right panel of Figure 42 and the last term in equation (90) accounts for population decay (diagonal terms in density matrix) and dephasing (off-diagonal terms in density matrix). The solutions to the master equation given in equation (90) are well known for the V-level system [205], working through them yields two different types of perturbation pathways that contribute to the nonlinear signal. The first type describes population saturation effects, which can be expressed diagrammatically,

$$\rho_{00}^{(0)} \xrightarrow{E_1^*} \begin{pmatrix} \rho_{10}^{(1)} \\ \rho_{20}^{(1)} \end{pmatrix} \xrightarrow{E_1} \begin{pmatrix} \rho_{11}^{(2)} \\ \rho_{22}^{(2)} \end{pmatrix} \xrightarrow{E_2^*} \begin{pmatrix} \rho_{10}^{(3)} \\ \rho_{20}^{(3)} \end{pmatrix}, \quad (91)$$

where the second-order terms are population terms and no quantum beating between the $|1\rangle$ and $|2\rangle$ states exist. The applied fields are labeled above the arrows, where E_1 is the pump (it acts twice) and E_2 is the probe.

Another class of terms in the perturbation pathways are the coherent terms that describe quantum beating effects. These are given by the diagrams,

$$\rho_{00}^{(0)} \xrightarrow{E_1^*} \begin{pmatrix} \rho_{10}^{(1)} \\ \rho_{20}^{(1)} \end{pmatrix} \xrightarrow{E_1} \rho_{12}^{(2)} \xrightarrow{E_2^*} \begin{pmatrix} \rho_{10}^{(3)} \\ \rho_{20}^{(3)} \end{pmatrix}, \quad (92)$$

where the non-radiative coherence can be seen in the second-order. The nonlinear signal found by solving equation (90) can be used in the optical Bloch equations to find the homodyne detected DR signal given by equation (89).

In conclusion, we have investigated the effects of exciton-plasmon coupling on the nonradiative, coherent behavior in a hybrid metal-semiconductor structure. We have measured exciton-plasmon coupling evidenced by a large red-shift of the pump-probe

signal on the order of ~ 10 meV. In the presence of exciton-plasmon coupling, the measured coherence lifetimes decreased by a factor of ~ 3.9 . Despite this decrease, we have found that the coherence lifetimes are still more than ten times longer than that of plasmons alone, indicating plasmon coherence lifetimes are not the limiting factor in these coupled systems. Because of the large nonlinearities inherent in semiconductor nanostructures and the field concentrating effects of plasmonics, hybrid materials like those studied here, show promise in bridging the gap between nanophotonics and quantum plasmonics. Knowledge of the coherent dynamics in these hybrid oscillator systems will prove critical to developing plasmonic-based qubit communication and quantum information processing devices.

Citations

1. Novoselov, K.S., et al., *Two-dimensional gas of massless Dirac fermions in graphene*. Nature, 2005. **438**(7065): p. 197-200.
2. Novoselov, K.S., et al., *Two-Dimensional Atomic Crystals*. Proceedings of the National Academy of Sciences of the United States of America, 2005. **102**(30): p. 10451-10453.
3. Qiu, D.Y., H. Felipe, and S.G. Louie, *Optical spectrum of MoS₂: Many-body effects and diversity of exciton states*. Physical review letters, 2013. **111**(21): p. 216805.
4. Feng, J., et al., *Strain-engineered artificial atom as a broad-spectrum solar energy funnel*. Nature Photonics, 2012. **6**(12): p. 866-872.
5. Shi, H., et al., *Quasiparticle band structures and optical properties of strained monolayer MoS₂ and WS₂*. Physical Review B, 2013. **87**(15): p. 155304.
6. Cheiwchanchamnangij, T. and W.R. Lambrecht, *Quasiparticle band structure calculation of monolayer, bilayer, and bulk MoS₂*. Physical Review B, 2012. **85**(20): p. 205302.
7. Ramasubramaniam, A., *Large excitonic effects in monolayers of molybdenum and tungsten dichalcogenides*. Physical Review B, 2012. **86**(11): p. 115409.
8. Korn, T., et al., *Low-temperature photocarrier dynamics in monolayer MoS₂*. Applied Physics Letters, 2011. **99**(10): p. 102109.
9. Lagarde, D., et al., *Carrier and polarization dynamics in monolayer MoS₂*. Physical review letters, 2014. **112**(4): p. 047401.
10. Shi, H., et al., *Exciton dynamics in suspended monolayer and few-layer MoS₂ 2D crystals*. ACS nano, 2013. **7**(2): p. 1072-1080.
11. Sim, S., et al., *Exciton dynamics in atomically thin MoS₂: interexcitonic interaction and broadening kinetics*. Physical Review B, 2013. **88**(7): p. 075434.
12. Kumar, N., et al., *Exciton-exciton annihilation in MoSe₂ monolayers*. Physical Review B, 2014. **89**(12): p. 125427.
13. Mai, C., et al., *Many-Body Effects in Valleytronics: Direct Measurement of Valley Lifetimes in Single-Layer MoS₂*. Nano letters, 2013. **14**(1): p. 202-206.
14. Alem, N., et al., *Atomically thin hexagonal boron nitride probed by ultrahigh-resolution transmission electron microscopy*. Physical Review B, 2009. **80**(15): p. 155425.
15. Lee, C., et al., *Anomalous Lattice Vibrations of Single- and Few-Layer MoS₂*. ACS Nano, 2010. **4**(5): p. 2695-2700.
16. Mak, K.F., et al., *Atomically thin MoS₂: a new direct-gap semiconductor*. Physical Review Letters, 2010. **105**(13): p. 136805.
17. Bertolazzi, S., J. Brivio, and A. Kis, *Stretching and Breaking of Ultrathin MoS₂*. ACS Nano, 2011. **5**(12): p. 9703-9709.
18. Radisavljevic, B., et al., *Single-layer MoS₂ transistors*. Nat Nano, 2011. **6**(3): p. 147-150.

19. Radisavljevic, B., M.B. Whitwick, and A. Kis, *Integrated Circuits and Logic Operations Based on Single-Layer MoS₂*. ACS Nano, 2011. **5**(12): p. 9934-9938.
20. Splendiani, A., et al., *Emerging photoluminescence in monolayer MoS₂*. Nano letters, 2010. **10**(4): p. 1271-1275.
21. Ayari, A., et al., *Realization and electrical characterization of ultrathin crystals of layered transition-metal dichalcogenides*. Journal of Applied Physics, 2007. **101**(1): p. -.
22. Yin, Z., et al., *Single-Layer MoS₂ Phototransistors*. ACS Nano, 2011. **6**(1): p. 74-80.
23. Feng, J., et al., *Giant Moisture Responsiveness of VS₂ Ultrathin Nanosheets for Novel Touchless Positioning Interface*. Advanced Materials, 2012. **24**(15): p. 1969-1974.
24. Zhang, Y., et al., *Ambipolar MoS₂ Thin Flake Transistors*. Nano Letters, 2012. **12**(3): p. 1136-1140.
25. Coleman, J.N., et al., *Two-Dimensional Nanosheets Produced by Liquid Exfoliation of Layered Materials*. Science, 2011. **331**(6017): p. 568-571.
26. Smith, R.J., et al., *Large-Scale Exfoliation of Inorganic Layered Compounds in Aqueous Surfactant Solutions*. Advanced Materials, 2011. **23**(34): p. 3944-3948.
27. Zhou, K.-G., et al., *A Mixed-Solvent Strategy for Efficient Exfoliation of Inorganic Graphene Analogues*. Angewandte Chemie International Edition, 2011. **50**(46): p. 10839-10842.
28. May, P., et al., *Role of Solubility Parameters in Understanding the Steric Stabilization of Exfoliated Two-Dimensional Nanosheets by Adsorbed Polymers*. The Journal of Physical Chemistry C, 2012. **116**(20): p. 11393-11400.
29. Bissessur, R., J. Heising, and W. Hirpo, *Toward Pillared Layered Metal Sulfides. Intercalation of the Chalcogenide Clusters Co₆Q₈(PR₃)₆ (Q = S, Se, and Te and R = Alkyl) into MoS₂*. Chemistry of Materials, 1996. **8**(2): p. 318-320.
30. Joensen, P., R.F. Frindt, and S.R. Morrison, *Single-layer MoS₂*. Materials Research Bulletin, 1986. **21**(4): p. 457-461.
31. Osada, M. and T. Sasaki, *Exfoliated oxide nanosheets: new solution to nanoelectronics*. Journal of Materials Chemistry, 2009. **19**(17): p. 2503-2511.
32. Eda, G., et al., *Photoluminescence from Chemically Exfoliated MoS₂*. Nano Letters, 2011. **11**(12): p. 5111-5116.
33. Zeng, Z., et al., *Single-Layer Semiconducting Nanosheets: High-Yield Preparation and Device Fabrication*. Angewandte Chemie International Edition, 2011. **50**(47): p. 11093-11097.
34. Dines, M.B., *Lithium intercalation via n-Butyllithium of the layered transition metal dichalcogenides*. Materials Research Bulletin, 1975. **10**(4): p. 287-291.
35. Gutiérrez, H.R., et al., *Extraordinary Room-Temperature Photoluminescence in Triangular WS₂ Monolayers*. Nano Letters, 2012. **13**(8): p. 3447-3454.
36. Perea-López, N., et al., *Photosensor Device Based on Few-Layered WS₂ Films*. Advanced Functional Materials, 2013. **23**(44): p. 5511-5517.

37. Elías, A.L., et al., *Controlled Synthesis and Transfer of Large-Area WS₂ Sheets: From Single Layer to Few Layers*. ACS Nano, 2013. **7**(6): p. 5235-5242.
38. Berkdemir, A., et al., *Identification of individual and few layers of WS₂ using Raman Spectroscopy*. Scientific Reports, 2013. **3**: p. 1755.
39. Huang, J.-K., et al., *Large-area synthesis of highly crystalline WSe₂ monolayers and device applications*. ACS nano, 2013. **8**(1): p. 923-930.
40. Wu, S., et al., *Vapor–Solid Growth of High Optical Quality MoS₂ Monolayers with Near-Unity Valley Polarization*. ACS Nano, 2013. **7**(3): p. 2768-2772.
41. Lin, Y.-C., et al., *Atomically Thin Heterostructures based on Single-Layer Tungsten Diselenide and Graphene*. Nano letters, 2014.
42. Saidi, W.A., *Van der Waals epitaxial growth of transition metal dichalcogenides on pristine and N-doped graphene*. Crystal Growth & Design, 2014. **14**(10): p. 4920-4928.
43. Kuc, A., N. Zibouche, and T. Heine, *Influence of quantum confinement on the electronic structure of the transition metal sulfide TM_2S_3* . Physical Review B, 2011. **83**(24): p. 245213.
44. Kobayashi, K. and J. Yamauchi, *Electronic structure and scanning-tunneling-microscopy image of molybdenum dichalcogenide surfaces*. Physical Review B, 1995. **51**(23): p. 17085-17095.
45. Li, T. and G. Galli, *Electronic Properties of MoS₂ Nanoparticles*. The Journal of Physical Chemistry C, 2007. **111**(44): p. 16192-16196.
46. Leitao, L., et al., *Performance Limits of Monolayer Transition Metal Dichalcogenide Transistors*. Electron Devices, IEEE Transactions on, 2011. **58**(9): p. 3042-3047.
47. Ding, Y., et al., *First principles study of structural, vibrational and electronic properties of graphene-like MX₂ (M=Mo, Nb, W, Ta; X=S, Se, Te) monolayers*. Physica B: Condensed Matter, 2011. **406**(11): p. 2254-2260.
48. Ataca, C., H. Şahin, and S. Ciraci, *Stable, Single-Layer MX₂ Transition-Metal Oxides and Dichalcogenides in a Honeycomb-Like Structure*. The Journal of Physical Chemistry C, 2012. **116**(16): p. 8983-8999.
49. Lebègue, S. and O. Eriksson, *Electronic structure of two-dimensional crystals from *ab initio* theory*. Physical Review B, 2009. **79**(11): p. 115409.
50. Frindt, R.F., *The optical properties of single crystals of WSe₂ and MoTe₂*. Journal of Physics and Chemistry of Solids, 1963. **24**(9): p. 1107-1108.
51. Frindt, R.F. and A.D. Yoffe, *Physical Properties of Layer Structures: Optical Properties and Photoconductivity of Thin Crystals of Molybdenum Disulphide*. Proceedings of the Royal Society of London A: Mathematical, Physical and Engineering Sciences, 1963. **273**(1352): p. 69-83.
52. Kam, K.K. and B.A. Parkinson, *Detailed photocurrent spectroscopy of the semiconducting group VIB transition metal dichalcogenides*. The Journal of Physical Chemistry, 1982. **86**(4): p. 463-467.
53. Bollinger, M.V., et al., *One-Dimensional Metallic Edge States in MoS_2* . Physical Review Letters, 2001. **87**(19): p. 196803.

54. Castro Neto, A.H., *Charge Density Wave, Superconductivity, and Anomalous Metallic Behavior in 2D Transition Metal Dichalcogenides*. Physical Review Letters, 2001. **86**(19): p. 4382-4385.
55. Liu, K.-K., et al., *Growth of Large-Area and Highly Crystalline MoS₂ Thin Layers on Insulating Substrates*. Nano Letters, 2012. **12**(3): p. 1538-1544.
56. Balendhran, S., et al., *Atomically thin layers of MoS₂ via a two step thermal evaporation-exfoliation method*. Nanoscale, 2012. **4**(2): p. 461-466.
57. Shi, Y., et al., *van der Waals Epitaxy of MoS₂ Layers Using Graphene As Growth Templates*. Nano Letters, 2012. **12**(6): p. 2784-2791.
58. Peng, Y., et al., *Hydrothermal Synthesis of MoS₂ and Its Pressure-Related Crystallization*. Journal of Solid State Chemistry, 2001. **159**(1): p. 170-173.
59. Peng, Y., et al., *Hydrothermal Synthesis and Characterization of Single-Molecular-Layer MoS₂ and MoSe₂*. Chemistry Letters, 2001. **30**(8): p. 772-773.
60. Kumar, A. and P.K. Ahluwalia, *Electronic structure of transition metal dichalcogenides monolayers 1H-MX₂ (M = Mo, W; X = S, Se, Te) from ab-initio theory: new direct band gap semiconductors*. The European Physical Journal B, 2012. **85**(6): p. 1-7.
61. Böker, T., et al., *Band structure of MoS₂, MoSe₂, and alpha-MoTe₂: Angle-resolved photoelectron spectroscopy and *ab initio* calculations*. Physical Review B, 2001. **64**(23): p. 235305.
62. Zhao, W., et al., *Evolution of Electronic Structure in Atomically Thin Sheets of WS₂ and WSe₂*. ACS Nano, 2012. **7**(1): p. 791-797.
63. Jones, A.M., et al., *Optical generation of excitonic valley coherence in monolayer WSe₂*. Nature nanotechnology, 2013. **8**(9): p. 634-638.
64. Coehoorn, R., C. Haas, and R.A. de Groot, *Electronic structure of MoSe₂, MoS₂, and WSe₂ II. The nature of the optical band gaps*. Physical Review B, 1987. **35**(12): p. 6203-6206.
65. Berkelbach, T.C., M.S. Hybertsen, and D.R. Reichman, *Theory of neutral and charged excitons in monolayer transition metal dichalcogenides*. Physical Review B, 2013. **88**(4): p. 045318.
66. Ross, J.S., et al., *Electrical control of neutral and charged excitons in a monolayer semiconductor*. Nat Commun, 2013. **4**: p. 1474.
67. Zhu, Z.Y., Y.C. Cheng, and U. Schwingenschlögl, *Giant spin-orbit-induced spin splitting in two-dimensional transition-metal dichalcogenide semiconductors*. Physical Review B, 2011. **84**(15): p. 153402.
68. Zeng, H., et al., *Optical signature of symmetry variations and spin-valley coupling in atomically thin tungsten dichalcogenides*. Scientific reports, 2013. **3**.
69. Jin, W., et al., *Direct measurement of the thickness-dependent electronic band structure of MoS₂ using angle-resolved photoemission spectroscopy*. Physical Review Letters, 2013. **111**(10): p. 106801.
70. Zhang, Y., et al., *Direct observation of the transition from indirect to direct bandgap in atomically thin epitaxial MoSe₂*. Nature nanotechnology, 2013.

71. Kadantsev, E.S. and P. Hawrylak, *Electronic structure of a single MoS₂ monolayer*. Solid State Communications, 2012. **152**(10): p. 909-913.
72. Kośmider, K. and J. Fernández-Rossier, *Electronic properties of the MoS₂-WS₂ heterojunction*. Physical Review B, 2013. **87**(7): p. 075451.
73. Song, Y. and H. Dery, *Transport Theory of Monolayer Transition-Metal Dichalcogenides through Symmetry*. Physical Review Letters, 2013. **111**(2): p. 026601.
74. Kormányos, A., et al., *Monolayer MoS₂: Trigonal warping, the gamma valley, and spin-orbit coupling effects*. Physical Review B, 2013. **88**(4): p. 045416.
75. Liu, G.-B., et al., *Three-band tight-binding model for monolayers of group-VIB transition metal dichalcogenides*. Physical Review B, 2013. **88**(8): p. 085433.
76. Xiao, D., et al., *Coupled spin and valley physics in monolayers of MoS₂ and other group-VI dichalcogenides*. Physical Review Letters, 2012. **108**(19): p. 196802.
77. Rycerz, A., J. Tworzydło, and C.W.J. Beenakker, *Valley filter and valley valve in graphene*. Nat Phys, 2007. **3**(3): p. 172-175.
78. Xiao, D., W. Yao, and Q. Niu, *Valley-Contrasting Physics in Graphene: Magnetic Moment and Topological Transport*. Physical Review Letters, 2007. **99**(23): p. 236809.
79. Yao, W., D. Xiao, and Q. Niu, *Valley-dependent optoelectronics from inversion symmetry breaking*. Physical Review B, 2008. **77**(23): p. 235406.
80. Bishop, N.C., et al., *Valley Polarization and Susceptibility of Composite Fermions around a Filling Factor $\nu=3/2$* . Physical Review Letters, 2007. **98**(26): p. 266404.
81. Shkolnikov, Y.P., et al., *Valley Splitting of AlAs Two-Dimensional Electrons in a Perpendicular Magnetic Field*. Physical Review Letters, 2002. **89**(22): p. 226805.
82. Zeng, H., et al., *Valley polarization in MoS₂ monolayers by optical pumping*. Nat Nano, 2012. **7**(8): p. 490-493.
83. Cao, T., et al., *Valley-selective circular dichroism of monolayer molybdenum disulfide*. Nature communications, 2012. **3**: p. 887.
84. Mak, K.F., et al., *Control of valley polarization in monolayer MoS₂ by optical helicity*. Nature nanotechnology, 2012. **7**(8): p. 494-498.
85. Wang, Q., et al., *Valley Carrier Dynamics in Monolayer Molybdenum Disulfide from Helicity-Resolved Ultrafast Pump-Probe Spectroscopy*. ACS Nano, 2013. **7**(12): p. 11087-11093.
86. Wang, R., et al., *Ultrafast and spatially resolved studies of charge carriers in atomically thin molybdenum disulfide*. Physical Review B, 2012. **86**(4): p. 045406.
87. Cundiff, S.T., et al., *Optical 2-D Fourier transform spectroscopy of excitons in semiconductor nanostructures*. Selected Topics in Quantum Electronics, IEEE Journal of, 2012. **18**(1): p. 318-328.
88. Koch, M., et al., *Quantum beats versus polarization interference: An experimental distinction*. Physical review letters, 1992. **69**(25): p. 3631.

89. Wegener, M., et al., *Line shape of time-resolved four-wave mixing*. Physical Review A, 1990. **42**(9): p. 5675-5683.
90. Wang, H., et al., *Transient nonlinear optical response from excitation induced dephasing in GaAs*. Physical review letters, 1993. **71**(8): p. 1261.
91. Shacklette, J. and S.T. Cundiff, *Nonperturbative transient four-wave-mixing line shapes due to excitation-induced shift and excitation-induced dephasing*. JOSA B, 2003. **20**(4): p. 764-769.
92. Bott, K., et al., *Influence of exciton-exciton interactions on the coherent optical response in GaAs quantum wells*. Physical Review B, 1993. **48**(23): p. 17418.
93. Ernst, R.R., G. Bodenhausen, and A. Wokaun, *Principles of nuclear magnetic resonance in one and two dimensions*. 1991.
94. Bristow, A., et al., *A versatile ultrastable platform for optical multidimensional Fourier-transform spectroscopy*. Review of Scientific Instruments, 2009. **80**(7): p. 073108.
95. Siemens, M.E., et al., *Resonance lineshapes in two-dimensional Fourier transform spectroscopy*. Optics express, 2010. **18**(17): p. 17699-17708.
96. Wang, Q.H., et al., *Electronics and optoelectronics of two-dimensional transition metal dichalcogenides*. Nature nanotechnology, 2012. **7**(11): p. 699-712.
97. Peyghambarian, N., S.W. Koch, and A. Mysyrowicz, *Introduction to semiconductor optics*. 1994: Prentice-Hall, Inc.
98. Rohlfing, M., P. Krüger, and J. Pollmann, *Quasiparticle band-structure calculations for C, Si, Ge, GaAs, and SiC using Gaussian-orbital basis sets*. Physical Review B, 1993. **48**(24): p. 17791.
99. Yoon, Y., K. Ganapathi, and S. Salahuddin, *How good can monolayer MoS2 transistors be?* Nano letters, 2011. **11**(9): p. 3768-3773.
100. Mark, F., *Optical properties of solids*. 2001, Oxford University Press, New York.
101. Yoffe, A.D., *Electronic properties of two dimensional solids: The layer type transition metal dichalcogenides*, in *Festkörperprobleme 13*. 1973, Springer. p. 1-29.
102. Beal, A., J. Knights, and W. Liang, *Transmission spectra of some transition metal dichalcogenides. II. Group VIA: trigonal prismatic coordination*. Journal of Physics C: Solid State Physics, 1972. **5**(24): p. 3540.
103. Fehrenbach, G., et al., *Transient optical spectra of a dense exciton gas in a direct-gap semiconductor*. Physical Review Letters, 1982. **49**(17): p. 1281.
104. Frey, G.L., et al., *Optical-absorption spectra of inorganic fullerenelike MS₂ (M= Mo, W)*. Physical Review B, 1998. **57**(11): p. 6666-6671.
105. Haug, H. and S.W. Koch, *Quantum theory of the optical and electronic properties of semiconductors*. Vol. 3. 2004: World Scientific.
106. van Schilfgaarde, M. and M. Katsnelson, *First-principles theory of nonlocal screening in graphene*. Physical Review B, 2011. **83**(8): p. 081409.
107. Fox, M., *Quantum Optics: An Introduction: An Introduction*. Vol. 6. 2006: Oxford University Press.

108. Xu, X., et al., *Spin and pseudospins in layered transition metal dichalcogenides*. Nature Physics, 2014. **10**(5): p. 343-350.
109. Tanimura, Y. and S. Mukamel, *Two-dimensional femtosecond vibrational spectroscopy of liquids*. The Journal of chemical physics, 1993. **99**(12): p. 9496-9511.
110. Cowan, M., et al., *Ultrafast memory loss and energy redistribution in the hydrogen bond network of liquid H₂O*. Nature, 2005. **434**(7030): p. 199-202.
111. Hybl, J.D., et al., *Two-dimensional electronic spectroscopy*. Chemical physics letters, 1998. **297**(3): p. 307-313.
112. Brixner, T., et al., *Two-dimensional spectroscopy of electronic couplings in photosynthesis*. Nature, 2005. **434**(7033): p. 625-628.
113. Wong, C.Y., et al., *Electronic coherence lineshapes reveal hidden excitonic correlations in photosynthetic light harvesting*. Nature chemistry, 2012. **4**(5): p. 396-404.
114. Tekavec, P.F., G.A. Lott, and A.H. Marcus, *Fluorescence-detected two-dimensional electronic coherence spectroscopy by acousto-optic phase modulation*. The Journal of chemical physics, 2007. **127**(21): p. 214307.
115. Dai, X., et al., *Two-dimensional double-quantum spectra reveal collective resonances in an atomic vapor*. Physical review letters, 2012. **108**(19): p. 193201.
116. Li, H., et al., *Unraveling quantum pathways using optical 3D Fourier-transform spectroscopy*. Nature communications, 2013. **4**: p. 1390.
117. Dai, X., et al., *Two-dimensional Fourier-transform spectroscopy of potassium vapor*. Physical Review A, 2010. **82**(5): p. 052503.
118. Li, X., et al., *Many-body interactions in semiconductors probed by optical two-dimensional Fourier transform spectroscopy*. Physical review letters, 2006. **96**(5): p. 057406.
119. Turner, D.B., et al., *Persistent exciton-type many-body interactions in GaAs quantum wells measured using two-dimensional optical spectroscopy*. Physical Review B, 2012. **85**(20): p. 201303.
120. Harel, E., et al., *Measurement of electronic splitting in PbS quantum dots by two-dimensional nonlinear spectroscopy*. Physical Review B, 2012. **86**(7): p. 075412.
121. Moody, G., et al., *Exciton relaxation and coupling dynamics in a GaAs/Al_xGa_{1-x}As quantum well and quantum dot ensemble*. Physical Review B, 2011. **83**(24): p. 245316.
122. Moody, G., et al., *Exciton-exciton and exciton-phonon interactions in an interfacial GaAs quantum dot ensemble*. Physical Review B, 2011. **83**(11): p. 115324.
123. Moody, G., et al., *Influence of confinement on biexciton binding in semiconductor quantum dot ensembles measured with two-dimensional spectroscopy*. Physical Review B, 2013. **87**(4): p. 041304.
124. Moody, G., et al., *Fifth-order nonlinear optical response of excitonic states in an InAs quantum dot ensemble measured with two-dimensional spectroscopy*. Physical Review B, 2013. **87**(4): p. 045313.

125. Moody, G., et al., *Correlation and dephasing effects on the non-radiative coherence between bright excitons in an InAs QD ensemble measured with 2D spectroscopy*. Solid State Communications, 2013. **163**: p. 65-69.
126. Kasprzak, J., et al., *Coherent coupling between distant excitons revealed by two-dimensional nonlinear hyperspectral imaging*. Nature Photonics, 2011. **5**(1): p. 57-63.
127. Aue, W., E. Bartholdi, and R.R. Ernst, *Two-dimensional spectroscopy. Application to nuclear magnetic resonance*. The Journal of Chemical Physics, 1976. **64**(5): p. 2229-2246.
128. Vogelsanger, B. and A. Bauder, *Two-dimensional microwave Fourier transform spectroscopy*. The Journal of chemical physics, 1990. **92**(7): p. 4101-4114.
129. Suter, D., H. Klepel, and J. Mlynek, *Time-resolved two-dimensional spectroscopy of optically driven atomic sublevel coherences*. Physical review letters, 1991. **67**(15): p. 2001.
130. Noda, I., *Two-dimensional infrared spectroscopy*. Journal of the American Chemical Society, 1989. **111**(21): p. 8116-8118.
131. Asplund, M., M.T. Zanni, and R.M. Hochstrasser, *Two-dimensional infrared spectroscopy of peptides by phase-controlled femtosecond vibrational photon echoes*. Proceedings of the National Academy of Sciences, 2000. **97**(15): p. 8219-8224.
132. Golonzka, O., et al., *Vibrational anharmonicities revealed by coherent two-dimensional infrared spectroscopy*. Physical review letters, 2001. **86**(10): p. 2154.
133. Zhu, X., M.S. Hybertsen, and P. Littlewood, *Quantum beats in photon echo from four-waving mixing*. Physical review letters, 1994. **73**(1): p. 209.
134. Lyssenko, V., et al., *Nature of nonlinear four-wave-mixing beats in semiconductors*. Physical Review B, 1993. **48**(8): p. 5720.
135. Borca, C.N., et al., *Optical two-dimensional Fourier transform spectroscopy of semiconductors*. Chemical physics letters, 2005. **416**(4): p. 311-315.
136. Zhang, T., et al., *Polarization-dependent optical 2D Fourier transform spectroscopy of semiconductors*. Proceedings of the National Academy of Sciences, 2007. **104**(36): p. 14227-14232.
137. Malard, L.M., et al., *Observation of intense second harmonic generation from MoS₂ atomic crystals*. Physical Review B, 2013. **87**(20): p. 201401.
138. Li, Y., et al., *Probing symmetry properties of few-layer MoS₂ and h-BN by optical second-harmonic generation*. Nano letters, 2013. **13**(7): p. 3329-3333.
139. Yajima, T. and Y. Taira, *Spatial optical parametric coupling of picosecond light pulses and transverse relaxation effect in resonant media*. Journal of the Physical Society of Japan, 1979. **47**(5): p. 1620-1626.
140. Boyd, R.W., *Nonlinear optics*. 2003: Academic press.
141. Yang, L., et al., *Two-dimensional optical spectroscopy of excitons in semiconductor quantum wells: Liouville-space pathway analysis*. Physical Review B, 2007. **75**(12): p. 125302.

142. Brixner, T., *Tunable two-dimensional femtosecond spectroscopy*. Optics letters, 2004. **29**(8): p. 884-886.
143. Cowan, M., J. Ogilvie, and R. Miller, *Two-dimensional spectroscopy using diffractive optics based phased-locked photon echoes*. Chemical physics letters, 2004. **386**(1): p. 184-189.
144. Kim, J., S. Mukamel, and G.D. Scholes, *Two-dimensional electronic double-quantum coherence spectroscopy*. Accounts of chemical research, 2009. **42**(9): p. 1375-1384.
145. Gundogdu, K., et al., *Multidimensional coherent spectroscopy made easy*. Chemical Physics, 2007. **341**(1): p. 89-94.
146. Myers, J.A., et al., *Two-color two-dimensional Fourier transform electronic spectroscopy with a pulse-shaper*. Optics express, 2008. **16**(22): p. 17420-17428.
147. Volkov, V., R. Schanz, and P. Hamm, *Active phase stabilization in Fourier-transform two-dimensional infrared spectroscopy*. Optics letters, 2005. **30**(15): p. 2010-2012.
148. Zhang, T., et al., *Optical two-dimensional Fourier transform spectroscopy with active interferometric stabilization*. Optics express, 2005. **13**(19): p. 7432-7441.
149. Cundiff, S.T., *Coherent spectroscopy of semiconductors*. Optics express, 2008. **16**(7): p. 4639-4664.
150. Kuznetsova, I., et al., *Determination of homogeneous and inhomogeneous broadening in semiconductor nanostructures by two-dimensional Fourier-transform optical spectroscopy*. Physical Review B, 2007. **76**(15): p. 153301.
151. Nagayama, K., et al., *The use of cross-sections and of projections in two-dimensional NMR spectroscopy*. Journal of Magnetic Resonance (1969), 1978. **31**(1): p. 133-148.
152. Hybl, J.D., A.A. Ferro, and D.M. Jonas, *Two-dimensional Fourier transform electronic spectroscopy*. The Journal of Chemical Physics, 2001. **115**(14): p. 6606-6622.
153. Maznev, A., K. Nelson, and J. Rogers, *Optical heterodyne detection of laser-induced gratings*. Optics letters, 1998. **23**(16): p. 1319-1321.
154. Goodno, G.D., V. Astinov, and R.D. Miller, *Diffractive optics-based heterodyne-detected grating spectroscopy: application to ultrafast protein dynamics*. The Journal of Physical Chemistry B, 1999. **103**(4): p. 603-607.
155. Keusters, D., H.-S. Tan, and W.S. Warren, *Role of pulse phase and direction in two-dimensional optical spectroscopy*. The Journal of Physical Chemistry A, 1999. **103**(49): p. 10369-10380.
156. Tian, P., et al., *Femtosecond phase-coherent two-dimensional spectroscopy*. Science, 2003. **300**(5625): p. 1553-1555.
157. Dorrer, C., et al., *Spectral resolution and sampling issues in Fourier-transform spectral interferometry*. JOSA B, 2000. **17**(10): p. 1795-1802.
158. Lepetit, L., G. Cheriaux, and M. Joffre, *Linear techniques of phase measurement by femtosecond spectral interferometry for applications in spectroscopy*. JOSA B, 1995. **12**(12): p. 2467-2474.

159. Chernikov, A., et al., *Exciton Binding Energy and Nonhydrogenic Rydberg Series in Monolayer WS₂*. Physical review letters, 2014. **113**(7): p. 076802.
160. He, K., et al., *Tightly Bound Excitons in Monolayer WSe₂*. Physical review letters, 2014. **113**(2): p. 026803.
161. Singh, A., et al., *Coherent Electronic Coupling in Atomically Thin MoSe₂*. Physical Review Letters, 2014. **112**(21): p. 216804.
162. Mak, K.F., et al., *The Valley Hall Effect in MoS₂ Transistors*. arXiv preprint arXiv:1403.5039, 2014.
163. Wilson, J. and A. Yoffe, *The transition metal dichalcogenides discussion and interpretation of the observed optical, electrical and structural properties*. Advances in Physics, 1969. **18**(73): p. 193-335.
164. Tonndorf, P., et al., *Photoluminescence emission and Raman response of monolayer MoS₂, MoSe₂, and WSe₂*. Optics express, 2013. **21**(4): p. 4908-4916.
165. Chow, W.W. and S.W. Koch, *Semiconductor-Laser Fundamentals: Physics of the Gain Materials*. 1999: Springer.
166. Collini, E., et al., *Coherently wired light-harvesting in photosynthetic marine algae at ambient temperature*. Nature, 2010. **463**(7281): p. 644-647.
167. Reberstrost, P., et al., *Environment-assisted quantum transport*. New Journal of Physics, 2009. **11**(3): p. 033003.
168. Wang, G., et al., *Valley dynamics probed through charged and neutral exciton emission in monolayer WSe₂*. arXiv preprint arXiv:1402.6009, 2014.
169. Cui, Q., et al., *Transient Absorption Microscopy of Monolayer and Bulk WSe₂*. ACS nano, 2014. **8**(3): p. 2970-2976.
170. Boldt, F., K. Henneberger, and V. May, *Many-Body Theory for the Dense Exciton Gas of Direct Semiconductors II. Calculation of Exciton Level Shift and Damping in Dependence on Exciton Density*. physica status solidi (b), 1985. **130**(2): p. 675-687.
171. Manzke, G., K. Henneberger, and V. May, *Many-Exciton Theory for Multiple Quantum-Well Structures*. physica status solidi (b), 1987. **139**(1): p. 233-239.
172. Hellmann, R., et al., *Homogeneous linewidth of excitons in semimagnetic CdTe/Cd_{1-x}Mn_xTe multiple quantum wells*. Physical Review B, 1993. **48**(4): p. 2847.
173. Honold, A., et al., *Collision broadening of two-dimensional excitons in a GaAs single quantum well*. Physical Review B, 1989. **40**(9): p. 6442.
174. Wagner, H.P., et al., *Coherent optical nonlinearities and phase relaxation of quasi-three-dimensional and quasi-two-dimensional excitons in ZnS_xSe_{1-x}/ZnSe structures*. Physical Review B, 1997. **56**(19): p. 12581.
175. Keldysh, L., *Pis'ma Zh. Eksp. Teor. Fiz., 29 (1979)*. JETP Lett, 1979. **29**: p. 658.
176. Hanamura, E., et al., *Quantum wells with enhanced exciton effects and optical non-linearity*. Materials Science and Engineering: B, 1988. **1**(3): p. 255-258.
177. Keldysh, L., *Coulomb interaction in thin semiconductor and semimetal films*. Soviet Journal of Experimental and Theoretical Physics Letters, 1979. **29**: p. 658.

178. Schultheis, L., et al., *Optical dephasing of homogeneously broadened two-dimensional exciton transitions in GaAs quantum wells*. Physical Review B, 1986. **34**(12): p. 9027.
179. Dey, P., et al., *Mechanism of excitonic dephasing in layered InSe crystals*. Physical Review B, 2014. **89**(12): p. 125128.
180. Berthelot, A., et al., *Unconventional motional narrowing in the optical spectrum of a semiconductor quantum dot*. Nature Physics, 2006. **2**(11): p. 759-764.
181. Wang, H., et al., *Radiative Lifetimes of Excitons and Trions in Monolayers of Metal Dichalcogenide MoS₂*. arXiv preprint arXiv:1409.3996, 2014.
182. Wang, G., et al., *Non-linear Optical Spectroscopy of Excited Exciton States for Efficient Valley Coherence Generation in WSe₂ Monolayers*. arXiv preprint arXiv:1404.0056, 2014.
183. Deveaud, B., et al., *Enhanced radiative recombination of free excitons in GaAs quantum wells*. Physical review letters, 1991. **67**(17): p. 2355.
184. Miller, D., et al., *Electric field dependence of optical absorption near the band gap of quantum-well structures*. Physical Review B, 1985. **32**(2): p. 1043.
185. Dintinger, J., et al., *Terahertz All-Optical Molecule-Plasmon Modulation*. Advanced Materials, 2006. **18**(13): p. 1645-1648.
186. MacDonald, K.F., et al., *Ultrafast active plasmonics*. Nat Photon, 2009. **3**(1): p. 55-58.
187. Vasa, P., et al., *Ultrafast Manipulation of Strong Coupling in Metal–Molecular Aggregate Hybrid Nanostructures*. Acs Nano, 2010. **4**(12): p. 7559-7565.
188. Chang, D.E., et al., *A single-photon transistor using nanoscale surface plasmons*. Nat Phys, 2007. **3**(11): p. 807-812.
189. Bergman, D.J. and M.I. Stockman, *Surface Plasmon Amplification by Stimulated Emission of Radiation: Quantum Generation of Coherent Surface Plasmons in Nanosystems*. Physical Review Letters, 2003. **90**(2): p. 027402.
190. Noginov, M.A., et al., *Demonstration of a spaser-based nanolaser*. Nature, 2009. **460**(7259): p. 1110-1112.
191. Oulton, R.F., et al., *Plasmon lasers at deep subwavelength scale*. Nature, 2009. **461**(7264): p. 629-632.
192. Bellessa, J., et al., *Strong Coupling between Surface Plasmons and Excitons in an Organic Semiconductor*. Physical Review Letters, 2004. **93**(3): p. 036404.
193. Vasa, P., et al., *Real-time observation of ultrafast Rabi oscillations between excitons and plasmons in metal nanostructures with J-aggregates*. Nature Photonics, 2013. **7**(2): p. 128-132.
194. Vasa, P., et al., *Coherent exciton–surface-plasmon-polariton interaction in hybrid metal-semiconductor nanostructures*. Physical review letters, 2008. **101**(11): p. 116801.
195. Gómez, D.E., et al., *Surface Plasmon Mediated Strong Exciton–Photon Coupling in Semiconductor Nanocrystals*. Nano Letters, 2010. **10**(1): p. 274-278.
196. Fedutik, Y., et al., *Exciton-Plasmon-Photon Conversion in Plasmonic Nanostructures*. Physical Review Letters, 2007. **99**(13): p. 136802.

197. Hecker, N.E., R.A. Höpfel, and N. Sawaki, *Enhanced light emission from a single quantum well located near a metal coated surface*. Physica E: Low-dimensional Systems and Nanostructures, 1998. **2**(1–4): p. 98-101.
198. Okamoto, K., et al., *Surface-plasmon-enhanced light emitters based on InGaN quantum wells*. Nat Mater, 2004. **3**(9): p. 601-605.
199. Zhang, W., A.O. Govorov, and G.W. Bryant, *Semiconductor-Metal Nanoparticle Molecules: Hybrid Excitons and the Nonlinear Fano Effect*. Physical Review Letters, 2006. **97**(14): p. 146804.
200. Gontijo, I., et al., *Coupling of InGaN quantum-well photoluminescence to silver surface plasmons*. Physical Review B, 1999. **60**(16): p. 11564-11567.
201. Neogi, A., et al., *Enhancement of spontaneous recombination rate in a quantum well by resonant surface plasmon coupling*. Physical Review B, 2002. **66**(15): p. 153305.
202. Jacob, Z. and V.M. Shalaev, *Plasmonics Goes Quantum*. Science, 2011. **334**(6055): p. 463-464.
203. Wang, W., et al., *Interplay between strong coupling and radiative damping of excitons and surface plasmon polaritons in hybrid nanostructures*. ACS nano, 2014. **8**(1): p. 1056-1064.
204. Li, X., et al., *Raman coherence beats from the entangled state involving polarized excitons in single quantum dots*. Physical Review B, 2004. **70**(19): p. 195330.
205. Meystre, P. and M. Sargent, *Elements of quantum optics*. 2007: Springer Science & Business Media.